



# Explosive Nucleosynthesis in Sub-Chandrasekhar-mass White Dwarf Models for Type Ia Supernovae: Dependence on Model Parameters

Shing-Chi Leung<sup>1,2</sup> and Ken'ichi Nomoto<sup>1</sup>

<sup>1</sup> Kavli Institute for the Physics and Mathematics of the Universe (WPI), The University of Tokyo Institutes for Advanced Study, The University of Tokyo, Kashiwa, Chiba 277-8583, Japan; [shingchi.leung@ipmu.jp](mailto:shingchi.leung@ipmu.jp), [nomoto@astron.s.u-tokyo.ac.jp](mailto:nomoto@astron.s.u-tokyo.ac.jp)

<sup>2</sup> TAPIR, Walter Burke Institute for Theoretical Physics, Mailcode 350-17, Caltech, Pasadena, CA 91125, USA  
Received 2019 January 15; revised 2019 November 24; accepted 2019 November 25; published 2020 January 10

## Abstract

Recent observations of Type Ia supernovae (SNe Ia) have shown diversified properties of the explosion strength, light curves, and chemical composition. To investigate possible origins of such diversities in SNe Ia, we have presented multidimensional hydrodynamical studies of explosions and associated nucleosynthesis in near-Chandrasekhar-mass carbon–oxygen (CO) white dwarfs (WDs) for a wide range of parameters. In the present paper, we extend our wide parameter survey of models to the explosions of sub-Chandrasekhar-mass CO WDs. We take the double-detonation model for the explosion mechanism. The model parameters of the survey include a metallicity of  $Z = 0\text{--}5\,Z_{\odot}$ , a CO WD mass of  $M = 0.90\text{--}1.20\,M_{\odot}$ , and a He envelope mass of  $M_{\text{He}} = 0.05\text{--}0.20\,M_{\odot}$ . We also study how the initial He detonation configuration, such as spherical, bubble, and ring shapes, triggers the C detonation. For these parameters, we derive the minimum He envelope mass necessary to trigger the C detonation. We then examine how the explosion dynamics and associated nucleosynthesis depend on these parameters, and we compare our results with the previous representative models. We compare our nucleosynthesis yields with the unusual abundance patterns of Fe-peak elements and isotopes observed in SNe Ia SN 2011fe, SN 2012cg, and SN 2014J, as well as SN Ia remnant 3C 397, to provide constraints on their progenitors and environments. We provide the nucleosynthesis yields table of the sub-Chandrasekhar-mass explosions, to discuss their roles in the galactic chemical evolution and archaeology.

*Unified Astronomy Thesaurus concepts:* Type Ia supernovae (1728); Hydrodynamical simulations (767); Explosive nucleosynthesis (503); Chemical abundances (224)

## 1. Introduction

Type Ia supernovae (SNe Ia) are known to have almost homogenized light curves and spectra, thus being used as a standard candle for studying the cosmic acceleration that led to the discovery of dark energy (e.g., Bergström & Goobar 2004; Branch & Wheeler 2017).

The basic properties of SNe Ia have been well modeled as the explosions of CO white dwarfs (WDs), which have both near-Chandrasekhar mass and sub-Chandrasekhar mass (e.g., Hillebrandt & Niemeyer 2000). However, it is still controversial which mass (near-Chandrasekhar vs. sub-Chandrasekhar) of the WD is the actual progenitor. For the pre-SN evolution in close binaries, both the single-degenerate (SD) scenario and the double-degenerate (DD) scenario have been discussed, but the actual evolutionary path remains unclear (e.g., Nomoto et al. 1997; Maoz et al. 2011).

Further, recent observations have shown the diversified properties of light curves and spectra of SNe Ia, including very peculiar ones (e.g., Li et al. 2001; Jha 2017; Jiang et al. 2017; Taubenberger 2017). The diversity can be characterized by a wide range of  $^{56}\text{Ni}$  and also differences in the ejecta composition and abundance. To understand this diversity, a wide range of theoretical models become necessary in order to extract the effects of each model parameter to explosion properties and nucleosynthesis yields.

To understand the origin of such diversities, we are computing SN Ia models for wide ranges of model and environmental parameters. In Nomoto & Leung (2017) and Leung & Nomoto (2018) we have studied how the model parameters, including the central density, metallicity, initial flame structure, and C/O ratio, affect the explosion properties of near-Chandrasekhar-mass WD models. For example, we have demonstrated how some

well-observed SNe Ia and supernova remnants (SNRs) can be explained by tracing the variation of isotopes in the yields with respect to the change of model parameters.

In this paper, we present our parameter survey for the sub-Chandrasekhar-mass WD model. The sub-Chandrasekhar-mass explosions could occur in both SD and DD scenarios as follows.

### 1.1. Sub-Chandrasekhar-mass Models in the SD Scenario

In the SD scenario, C+O WDs accrete matter from the nondegenerate companion stars, which include slightly evolved main-sequence stars, red giant stars, He main-sequence stars, evolved He stars. As a result of H burning in the H-rich accreted material or a direct accretion of He, the mass of an He layer increases above the C+O core, leading to eventual He ignition (e.g., Nomoto & Leung 2017, 2018).

If the accretion rate of He,  $\dot{M}_{\text{He}}$ , is higher than  $\sim 10^{-8} M_{\odot} \text{ yr}^{-1}$ , He shell burning makes weak flashes that recur many times to increase the WD mass toward the Chandrasekhar mass (e.g., Nomoto 1982a; Woosley & Kasen 2011). For lower rates of  $10^{-10} M_{\odot} \text{ yr}^{-1} \lesssim \dot{M}_{\text{He}} \lesssim 10^{-8} M_{\odot} \text{ yr}^{-1}$ , the compressional heating rate is lower and thus the temperature of the He layer is lower, which causes a delay in the He ignition until the mass of the He layer becomes large enough and the density at the bottom of the He layer high enough for He burning to grow into detonation. It eventually leads to double detonation (Nomoto 1982b; Woosley et al. 1986). The double-detonation model has been widely studied in one-dimensional and multidimensional simulations for various model parameters (e.g., Livne 1990; Livne & Glasner 1990, 1991; Livne & Arnett 1995; Arnett 1996; Fink et al. 2007, 2010;

Sim et al. 2012; Moll & Woosley 2013; Moore et al. 2013; Polin et al. 2019; Shen et al. 2018).

The important property of the sub-Chandrasekhar-mass progenitors in the SD scenario is that the mass of the He layer exceeds  $\sim 0.05 M_{\odot}$  to induce an He detonation (e.g., Nomoto 1982b; Woosley et al. 1986). This is in contrast to the sub-Chandrasekhar-mass models in the DD scenario as discussed below.

### 1.2. Sub-Chandrasekhar-mass Models in the DD Scenario

In the DD scenario, the detonation near the surface of the primary WD can be triggered during the violent merging of two WDs for suitable binary parameters (e.g., Rasio & Shapiro 1995; Segretain et al. 1997; Guerrero et al. 2004; Yoon et al. 2007; Fryer et al. 2010; Dan et al. 2011; Raskin et al. 2012, 2014; Moll et al. 2014; Sato et al. 2015). However, if there exists no He, the occurrence of the surface C detonation may still depend on the numerical resolution (e.g., Sato et al. 2015; Pakmor 2017). Then, Pakmor et al. (2013) and Dan et al. (2015) presented an He-ignited double-detonation model where the He detonation near the surface is triggered because a certain mass of He-rich envelope is assumed to exist on both WDs. In contrast to the double detonation in the SD scenario, the He-ignited detonation could be triggered for a lower-mass He-rich envelope because of shock compression.

In the above DD model, the collision point can reach a sufficiently high temperature for triggering an He detonation. The He detonation can produce a shock wave that propagates through the He envelope and into the CO core. The shock heating in the C-rich matter can induce a central or off-center C detonation. The WD is then disrupted by the C detonation. This model may produce the diversity of the different brightness, depending on the masses of the CO core and the He envelope (e.g., Arnett 1996; Sim et al. 2010; Woosley & Kasen 2011; Pakmor et al. 2013; Polin et al. 2019; Shen et al. 2018).

### 1.3. Motivation

In Leung & Nomoto (2017) and Nomoto & Leung (2017) we have studied how the model parameters, including the central density, metallicity, initial flame structure, and C/O mass fraction ratio, affect the chemical yield of SNe Ia evolved from a near-Chandrasekhar-mass WD. By tracing the variations of isotopes with respect to the change of model parameters, we have demonstrated how some well-observed SNe Ia can be explained by the near-Chandrasekhar-mass model.

However, the occurrence rate of SNe Ia evolved from a sub-Chandrasekhar-mass WD is suggested to be higher than the near-Chandrasekhar-mass WD in population synthesis (see, e.g., Yungelson 2005; Maoz et al. 2014). It becomes necessary to ask whether the double-detonation model can explain SNe Ia similarly to the Chandrasekhar-mass model, or can even replace the Chandrasekhar-mass model in certain parameter space.

Furthermore, through multidimensional hydrodynamics simulations, one can draw constraints on how to trigger the C detonation by the He detonation in the aspherical configuration systematically. This will set constraints on the criteria in triggering the C detonation through the aspherical He detonation with or without geometrical convergence.

To investigate possible origins of large diversities of SNe Ia, we perform two-dimensional hydrodynamical studies of explosions

and associated nucleosynthesis in the sub-Chandrasekhar-mass CO WDs for wide ranges of parameters. All simulations use the code based on the two-dimensional hydrodynamics code developed for the explosion phase of SNe (Leung et al. 2015b).

This work is a continuation of our previous work in Leung & Nomoto (2017) and Nomoto & Leung (2017), where we have studied the dependence on model parameters of SNe Ia using the Chandrasekhar-mass models (Leung et al. 2015a; Nomoto & Leung 2017, 2018; Leung & Nomoto 2018). In Leung & Nomoto (2018) we covered the density, metallicity, flame structure, and detonation criteria. We have also shown that some of the chemical abundance features observed in recently observed SNe Ia can be reproduced by our models.

In the present paper, we want to extend our understanding to the sub-Chandrasekhar-mass models for an even wider parameter region. We intend not only to explain the observed diversities of SNe Ia but also to provide the predictions of nucleosynthesis properties for coming observations (e.g., Timmes et al. 2019).

In Section 2 we summarize the numerical methods used in this work and the input physics specific to model the sub-Chandrasekhar-mass model. In Section 3 we describe our two-dimensional simulations to study the exploding WDs starting from the He detonation at the envelope. In Section 5 we describe the benchmark model, which is regarded as the representation of a typical sub-Chandrasekhar-mass model. In Section 6 we describe nucleosynthesis yields and their dependence on the model parameters, including the WD mass, He envelope mass, and initial He detonation pattern. We also present our cross-comparison with the classical double-detonation model with spherical symmetry, as well as its possible impacts on galactic chemical evolution. In the appendices we provide further numerical details and tests we have done for this work. We also discuss the implications of our models, including a comparison with models in the literature.

## 2. Methods

### 2.1. Input Physics

Here we briefly review the structure of our hydrodynamics code and then describe the change done to describe the He detonation and the onset of C deflagration or C detonation. We use the same two-dimensional hydrodynamics code as reported in Leung et al. (2015b) for our simulations. The code solves the Euler equations in cylindrical coordinates where the spatial discretization is done by the fifth-order weighted essentially non-oscillatory scheme and the time discretization is done by the five-step third-order non-strong-stability-preserving Runge-Kutta scheme. We use the Helmholtz subroutine (Timmes & Arnett 1999; Timmes & Swesty 1999) as the matter equation of state (EOS). This EOS includes the arbitrarily relativistic and degenerate electron gas, ions as a classical ideal gas, Planckian photon gas, and electron-positron annihilation pairs. In the hydrodynamics section, we describe the chemical composition by a seven-isotope network, which includes  $^4\text{He}$ ,  $^{12}\text{C}$ ,  $^{16}\text{O}$ ,  $^{20}\text{Ne}$ ,  $^{24}\text{Mg}$ ,  $^{28}\text{Si}$ , and  $^{56}\text{Ni}$ .

The one-equation model (Niemeyer & Hillebrandt 1995) is used to model the velocity fluctuations in the subgrid scale due to turbulence. To describe the geometry of the two detonation fronts, we use the individual level-set functions (Osher & Sethian 1988) as used in Reinecke et al. (1999). The geometry of the fronts is constructed by locating zero-value points in the

level-set function, and then the fractional volume in each mesh being burnt by flame or detonation is extracted. The energy from nuclear burning is injected instantaneously to Eulerian grids that have an increase in the area (volume) fractions  $\alpha$  in the two-dimensional (three-dimensional) models enclosed by the contours and their boundaries. To prevent double-counting the energy released by burnt matter,  $\alpha$  is set to be a monotonic increasing throughout the simulations. In each step, the code calculates the area fraction based on how the zero-contour intersects with the grid mesh. A fraction of  $\alpha^*$  is obtained where  $\alpha = 1$  for a completely burnt cell and 0 for pure fuel. The value of  $\alpha^*$  is compared with that in the previous step  $\alpha_{\text{old}}$  and the larger one is taken, i.e.,  $\alpha = \max(\alpha^*, \alpha_{\text{old}})$ . For He detonation, we assume that the detonation is in the form of Chapman–Jouguet detonation, where the detonation propagates in sound speed given by  $\sqrt{\gamma_2(\partial p/\partial \rho)_s}$ , where  $\gamma_2$  is the adiabatic index,  $p$  is the pressure, and  $\rho$  is the density. For CO detonation, we used the same prescription as Sharpe (1999) by the numerical speed of pathological detonation.

All simulations are done by a resolution size of  $400^2$  using the cylindrical coordinate. We choose reflecting and outgoing boundaries for the inner and outer boundaries for both the  $r$ -axis and  $z$ -axis. The resolution is fixed at either 15 km or 23 km. The lower one is for higher-mass WDs (mass  $> 1 M_\odot$ ), while the higher one is for lower-mass WDs. The grid size is chosen such that the simulation box is about 2–3 times the initial WD radius. We do that because we want most exothermic reactions, which rely on the level-set method, to finish before the star reaches the outer boundary of the simulation box. We follow Roepke & Hillebrandt (2005) by implementing the moving-boundary technique so that when the stellar outer radius reaches the simulation box boundary, the grid expands with a similar speed so that most matter can be contained in the simulation box. In our calculation, we choose the averaged radial velocity of the low-density matter (defined by 1–10 times the atmospheric density) to be the expansion velocity. Following with the expansion, we also adjust the atmosphere density such that the total mass of matter in the “atmosphere” (also the minimum density allowed in the simulation) remains  $\sim 10^{-4}$  of the star. We model only one quadrant of the WD by the use of reflecting boundary.

In our computation, it takes typically 2–3 days for a hydrodynamics simulation for a quadrant from the onset of He detonation until homologous expansion develops by a single CPU run. The assumed symmetry allows only two He detonation bubbles to be ignited simultaneously. A more general detonation form as a single He detonation bubble requires hydrodynamics simulations of a hemisphere. The computational time can be lengthened by a factor of  $\sim 4$ , with also a factor of 2 increase in memory. Thus, only a small number of models are computed. In Appendix B we present some exploratory models using the relaxed symmetry and compare with our “quadrant” models. We also check the dependence of the general detonation model on the chosen resolution and report in Appendix C.

## 2.2. Nuclear Reaction Scheme

For the nuclear reactions of He-rich matter, the region swept up by the level-set contour is regarded as burning from  $^4\text{He}$  to  $^{56}\text{Ni}$ . For CO-rich matter, similar to previous works (Leung & Nomoto 2018), we use the three-step burning scheme so as to include more flexible nuclear reactions, especially when there are contributions from shock wave collisions. In this

work, we assume that this process is instantaneous regardless of the local density. We follow the use of the burning timescale as an approximation to burning where density is low (i.e.,  $\rho < 5 \times 10^7 \text{ g cm}^{-3}$ ). That includes the nuclear quasi-statistical equilibrium (NQSE) timescale and the NSE timescale, given by, respectively (see Calder et al. 2007; Townsley et al. 2007),

$$\tau_{\text{NQSE}} = \exp(182/T_{f,9} - 46.1) \text{ s}, \quad (1)$$

$$\tau_{\text{NSE}} = \exp(196/T_{f,9} - 41.6) \text{ s}, \quad (2)$$

where  $T_{f,9} = T_f/10^9 \text{ K}$  is the final temperature of the ash. For a time step shorter than these two timescales, we assume that a fraction of matter given by linear interpolation with  $\tau$  is burnt. For a time step longer than those, complete conversion of fuel to ash is assumed. Similar treatment is done for He detonation. We describe more details in Appendix A.

To determine whether a detonation wave can start, we follow the scheme in Fink et al. (2007). For an Eulerian grid of CO matter, when the temperature exceeds the threshold temperature as a function of density (see Tables 1 and 2 in Fink et al. 2007), a bubble or ring of hot ashes (i.e., NSE matter from CO and  $^{56}\text{Ni}$  from He) is put artificially around that grid of 1.5 times the grid size. In practice, we set the level-set scalar field  $S$  such way that  $S(r, z) = -\sqrt{(r - r_0)^2 + (z - z_0)^2} + 1.5\Delta x$ . Here  $r_0$  and  $z_0$  are the center coordinates of the bubble and  $\Delta x$  is the resolution size. However, when multiple detonation seeds are triggered, those within  $10\Delta x$  from existing ones are discarded. At a density between  $2 \times 10^7$  and  $10^9 \text{ g cm}^{-3}$ , detonation propagates in the form of pathological detonation, where behind shock front matter with a speed below the frozen sound speed appears (Sharpe 1999). The propagation velocity is obtained by solving the detonation structure explicitly. To prevent double-counting in the burnt material due to numerical diffusion, once a grid reaches NSE, it is forbidden to carry out  $^{16}\text{O}$  and  $^{24}\text{Mg}$  burning in the second burning step. In the NSE state, the final composition is changed by solving iteratively by requiring that the change in the internal energy equals the change in the binding energy up to the required precision. Matter in the NSE state is also allowed to carry out electron capture with a rate obtained by interpolating the precomputed rate table using the prescription described in Seitenzahl et al. (2010).

To apply NSE calculation in the modeling, after each hydrodynamics step we obtain a current density  $\rho$ , current electron fraction  $Y_{e,i}$ , trial temperature  $T_i$ , specific internal energy density  $\epsilon_i$ , and the nuclear binding energy per mass  $q_i$ . We look for the electron capture rate  $\dot{Y}_e$  and its corresponding neutrino energy-loss rate per mass  $\dot{q}_\nu$ . To obtain the thermodynamics state in NSE, we solve the implicit equation

$$\begin{aligned} \epsilon_i - q_i &= \epsilon_f(\rho, T_f, X_f) - q_f(\rho, T_f) \\ &+ (m_n - m_p - m_e)N_A c^2 \dot{Y}_e(\rho, T_i, Y_{e,i}) \\ &+ \dot{q}_\nu(\rho, T_i, Y_{e,i}). \end{aligned} \quad (3)$$

Here  $\epsilon_f(\rho, T_f, X_f)$  and  $q_f(\rho, T_f)$  are those for the final state.  $(m_n - m_p - m_e)N_A c^2$  is the energy loss due to mass difference between neutron and electron–proton pair per mass. The above equation is solved by implicitly finding the  $T_f$  and its corresponding  $q_f$  such that the energy is balanced. The approximation  $\dot{Y}_e(\rho, T_i, Y_{e,i})$  is true when the electron capture



rate is much slower than the dynamical timescale, which is true for SNe Ia.

### 3. Initial Models

In this section we first describe the arrays of models we have performed for the SNe Ia using the sub-Chandrasekhar-mass WD. Then, we describe the explosion thermodynamics for each class of explosion.

In Table 1 we tabulate the models studied for the double-detonation model. The initial WD consists of a CO core and an He envelope. We regard the total WD mass  $M$ , the He envelope mass  $M_{\text{He}}$ , the initial metallicity  $Z$ , and the position of the He detonation seeds as input parameters. The initial WD is assumed to be isothermal at a temperature of  $10^8$  K.<sup>3</sup> For  $Z = 0.02$ , we choose 49%  $^{12}\text{C}$  and 49%  $^{16}\text{O}$  and 2%  $^{22}\text{Ne}$  in mass fractions, and for smaller  $Z$ , the mass fraction of  $^{22}\text{Ne}$  is smaller and C and O have equally larger mass fractions. For the He envelope, pure  $^4\text{He}$  is assumed. Notice that the prescription of  $^{22}\text{Ne}$  is not necessarily the only element that represents metallicity. For example, in Shen et al. (2018), the  $^{22}\text{Ne}$  mass fraction  $X(^{22}\text{Ne})$  scales as  $Z = 1.1X(^{22}\text{Ne})$ . A more precise matching between the abundances from the stellar evolutionary models and the hydrodynamics simulations will require a more detailed isotope network.

It is shown that the actual C/O ratio can be sensitive to  $M$  and  $Z$  (Umeda et al. 1999). We remark that a direct extension for different C/O ratio is not straightforward since it requires first a quantitative study on how C detonation is triggered as a function of density with a given composition.

To start the He detonation, we place a spherical detonation seed along the rotation symmetry axis. Due to the resolution limit, the initial detonation seed is 1.5 times the grid size in radius, i.e., 22 km. The position of the seed is regarded as an input parameter of the model, which ranges from 30 to 300 km. The detonation seed consists of hot ashes of  $^{56}\text{Ni}$ .

We notice that starting the explosion near the boundary may not be ideal in the two-dimensional models owing to the possibility of enhancing nuclear burning along the symmetry boundary. But for our case, the detonation propagates much faster than typical fluid velocity. The hydrodynamical instabilities, especially Rayleigh–Taylor instability, do not have adequate time to grow before the fuel is swept up by the detonation wave. So the boundary effect is less significant compared to the turbulent deflagration scenario. To construct the initial model, we choose models with a total mass  $M = 0.9\text{--}1.2 M_{\odot}$  and  $M_{\text{He}} = 0.05\text{--}0.35 M_{\odot}$ .

#### 3.1. Model Names

First, we describe how these models are named and how they are chosen. Each model is named by their parameters, including  $M$ ,  $M_{\text{He}}$ ,  $Z$ , and the initial position of the detonation bubble (sphere). For example, Model 105-050-2-50 stands for a WD with  $M = 1.05 M_{\odot}$ ,  $M_{\text{He}} = 0.05 M_{\odot}$ ,  $Z = 0.02$ , and the initial He detonation triggered at 50 km above the core-envelope interface.

The endings “–S50” and “–B50” stand for different initial He detonations. The term “S50” stands for a spherical detonation triggered at 50 km above the He/CO interface, and “B50” stands for a belt (ring) around the “equator” of the WD. “R50” stands for a bubble triggered at 50 km above the He/CO interface. For “2R50” or “3R50” we put two or three “bubbles” (a combination of torus and bubble) in the He envelope. Note that with the rotation and reflection symmetry, a bubble in the two-dimensional plane can be a “ring” if the bubble is away from the rotation axis, in its three-dimensional projection. The distance 50 km is chosen such that the surface of the initial bubble is slightly separated by at least one grid from the interface. We find that this separation is necessary to avoid overlapping the initial He detonation bubble with the CO-rich matter.

In Groups A–M in Table 1, the following effects are studied.

- (1) Initial mass  $M$ : In Groups A, B, C, and M we study the effects of progenitor mass on nucleosynthesis. For initial detonation with higher symmetry (“–S50” and “–B50” series), a lower He envelope mass of  $0.05 M_{\odot}$  is used, while for that with lower symmetry, the He envelope mass is fixed at  $M_{\text{He}} = 0.10$  or  $0.15 M_{\odot}$ . Metallicity is fixed at the solar metallicity. The progenitor varies from 0.9 to  $1.2 M_{\odot}$ .
- (2) He envelope mass  $M_{\text{He}}$ : In Groups D, E, F, and G we study the effects of He envelope mass  $M_{\text{He}}$ . Each group includes models of the same mass from 0.9 to  $1.2 M_{\odot}$  in a  $0.1 M_{\odot}$  interval, but with a different  $M_{\text{He}}$  from 0.05 to  $0.2 M_{\odot}$ . In all models, solar metallicity is assumed. We remark that different  $M_{\text{He}}$  masses are used for different initial detonation geometries. This is because for an He detonation with a lower symmetry, the effects of shock convergence by geometry are smaller. To make sure the second detonation can be triggered for comparison, a higher  $M_{\text{He}}$  is studied.
- (3) Metallicity  $Z$ : In Groups H, I, and J we study the effects of metallicity on the explosive nucleosynthesis. Each group consists of models of the same  $M$ ,  $M_{\text{He}}$ , and detonation configuration. Models vary by their metallicity from 0 to  $5 Z_{\odot}$ . We choose this large metallicity because in Leung & Nomoto (2018) we have already shown that such a high-metallicity model can be a clue to explain the observed SNRs. For Groups H and I we pick these models because they are the benchmark models of our sub-Chandrasekhar-mass SN Ia models.
- (4) Initial detonation geometry: In Groups K and L we study the effects of initial He detonation geometry. All models have the same  $M$  and  $M_{\text{He}}$  and are at solar metallicity. Group K consists of models with the detonation seed at different positions. Group L consists of models with different detonation geometries. It spans from a different number of detonation “bubbles” to those with a higher symmetry, such as spherical detonation.

### 4. Detonation Trigger

In the last column we classify the trigger mechanisms into four types. In all simulation groups (from Group C to M except Group L), all He detonations are started by placing a detonation spot at the radius 50 km along the rotation axis. This mimics a single hot spot that induces thermonuclear runaway in the form of a bubble. In general, the detonation propagates along the He

<sup>3</sup> In general, the WD can be away from the isothermal profile owing to the hydrostatic burning and convection. The exact profile depends on the competition between the compressional heating due to mass accretion and radiative cooling. In view of uncertainties during accretion, we neglect this factor and prepare identical initial models.



**Table 1**  
Model Parameters and the Global Properties of the Energetics and Nucleosynthesis of the SN Ia Model Performed in This Article

Group	Model	$\rho_c$	$M_{\text{He}}$	$R_{\text{seed}}$	$M$	$R$	$E_{\text{fin}}$	$E_{\text{nuc}}$	$t_{\text{det}}$	$\rho_{\text{det}}$	$R_{\text{det}}$	$M_{\text{Ni}}$	Type
A	090-050-2-B50	1.67	0.05	50	0.90	7160	3.82	5.08	2.71	1.00	4170	$<10^{-2}$	“Y”
A	095-050-2-B50	2.26	0.05	50	0.95	6710	4.70	6.17	2.29	1.00	3860	0.11	“Y”
A	100-050-2-B50	3.21	0.05	50	1.00	6180	7.62	9.34	1.74	1.07	2870	0.31	“Y”
A	110-050-2-B50	6.17	0.05	50	1.10	4930	10.8	13.1	1.18	1.24	3770	0.68	“Y”
B	090-050-2-S50	1.67	0.05	50	0.90	7160	3.53	4.68	1.35	6.53	20	0.02	“S”
B	095-050-2-S50	2.26	0.05	50	0.90	6710	7.28	8.56	1.18	6.15	40	0.45	“S”
B	100-050-2-S50	3.21	0.05	50	1.00	6180	8.70	10.2	0.98	6.03	70	0.60	“S”
B	110-050-2-S50	6.71	0.05	50	1.10	4930	11.7	13.8	0.83	11.7	40	0.82	“S”
C	090-100-2-50	1.67	0.10	50	0.90	7160	−0.50	0.77	nil	nil	nil	$<10^{-2}$	“N”
C	095-100-2-50	2.26	0.10	50	0.90	6710	−0.43	0.94	nil	nil	nil	$<10^{-2}$	“N”
C	100-100-2-50	3.21	0.10	50	1.00	6180	−0.36	1.38	nil	nil	nil	$<10^{-2}$	“N”
C	110-100-2-50	6.71	0.10	50	1.10	4930	11.1	13.0	0.94	1.04	3430	0.62	“X”
D	090-100-2-50	1.67	0.100	50	0.90	7160	−0.50	0.77	nil	nil	nil	$<10^{-2}$	“N”
D	090-150-2-50	1.67	0.150	50	0.90	7160	5.65	7.04	2.35	1.51	2100	0.14	“Y”
D	090-200-2-50	1.67	0.200	50	0.90	7160	7.92	9.02	1.21	1.03	3940	0.28	“X”
D	090-300-2-50	1.67	0.300	50	0.90	7160	11.6	12.9	0.83	1.00	3370	0.54	“D”
E	100-050-2-50	3.21	0.050	50	1.00	6180	−1.45	0.27	nil	nil	nil	$<10^{-2}$	“N”
E	100-075-2-50	3.21	0.075	50	1.00	6180	−1.08	0.63	nil	nil	nil	$<10^{-2}$	“N”
E	100-100-2-50	3.21	0.100	50	1.00	6180	−0.36	1.39	nil	nil	nil	$<10^{-2}$	“N”
E	100-150-2-50	3.21	0.150	50	1.00	6180	8.64	10.3	0.99	1.06	3370	0.47	“X”
E	100-200-2-50	3.21	0.200	50	1.00	6180	15.0	13.3	0.75	1.00	3360	0.61	“D”
F	110-050-2-50	6.17	0.050	50	1.10	4930	−1.89	0.39	nil	nil	nil	$1.1 \times 10^{-2}$	“N”
F	110-075-2-50	6.17	0.075	50	1.10	4930	9.88	12.1	1.11	1.04	3560	0.56	“X”
F	110-100-2-50	6.17	0.100	50	1.10	4930	11.1	13.0	0.94	1.04	3430	0.62	“X”
F	110-125-2-50	6.17	0.125	50	1.10	4930	14.4	14.9	0.69	1.10	3270	0.78	“X”
F	110-150-2-50	6.17	0.150	50	1.10	4930	14.8	15.4	0.45	1.03	3190	0.69	“D”
F	110-200-2-50	6.17	0.200	50	1.10	4930	15.7	17.9	0.32	1.09	3000	0.79	“D”
G	120-050-2-50	14.8	0.050	50	1.20	4250	14.4	17.5	0.90	1.10	3010	0.83	“X”
G	120-100-2-50	14.8	0.100	50	1.20	4250	16.7	19.8	0.39	1.00	2790	0.92	“D”
G	120-150-2-50	14.8	0.200	50	1.20	4250	18.9	22.1	0.26	1.56	2570	0.96	“D”
G	120-200-2-50	14.8	0.150	50	1.20	4250	20.2	23.2	0.27	1.61	2440	1.00	“D”
H	090-150-0-50	1.67	0.150	50	0.90	7160	5.68	6.95	2.35	1.63	2080	0.15	“Y”
H	090-150-2-50	1.67	0.150	50	0.90	7160	5.77	7.04	2.35	1.51	2100	0.14	“Y”
H	090-150-6-50	1.67	0.150	50	0.90	7160	5.79	7.06	2.35	1.47	2100	0.14	“Y”
H	090-150-10-50	1.67	0.150	50	0.90	7160	5.80	7.07	2.35	1.73	2080	0.12	“Y”
I	110-100-0-50	6.17	0.050	50	1.10	4930	11.3	13.8	0.94	1.02	3430	0.67	“X”
I	110-100-2-50	6.17	0.100	50	1.10	4930	11.1	13.0	0.94	1.04	3430	0.62	“X”
I	110-100-6-50	6.17	0.050	50	1.10	4930	11.2	13.4	0.93	1.01	3410	0.51	“X”
I	110-100-10-50	6.17	0.050	50	1.10	4930	11.8	13.9	0.93	1.01	3410	0.52	“X”
J	105-125-0-50	4.33	0.125	50	1.05	5300	9.85	12.2	0.96	1.06	3580	0.56	“X”
J	105-125-2-50	4.33	0.125	50	1.05	5300	10.3	15.2	0.94	1.04	3560	0.57	“X”
J	105-125-6-50	4.33	0.125	50	1.05	5300	10.3	12.4	0.96	1.03	3560	0.50	“X”
J	105-125-10-50	4.33	0.125	50	1.05	5300	10.0	11.9	0.96	1.04	3560	0.43	“X”
K	110-100-2-50	6.17	0.100	50	1.10	4930	11.1	13.0	0.94	1.04	3430	0.62	“X”
K	110-100-2-100	6.17	0.100	100	1.10	4930	11.1	13.1	0.93	1.04	3430	0.62	“X”
K	110-100-2-150	6.17	0.100	150	1.10	4930	11.8	13.6	0.93	1.06	3410	0.65	“X”
L	105-050-2-S50	4.33	0.050	50	1.05	5300	12.9	14.7	0.94	1.73	40	0.50	“S”
L	105-050-2-50	4.33	0.050	50	1.05	5300	−1.73	0.31	nil	nil	nil	$8.6 \times 10^{-3}$	“N”
L	105-050-2-2R50	4.33	0.050	50	1.05	5300	9.61	11.6	1.48	4.63	3090	0.48	“Y”
L	105-050-2-3R50	4.33	0.050	50	1.05	5300	−1.67	0.33	nil	nil	nil	$9.86 \times 10^{-2}$	“N”
M	090-150-2-50	1.67	0.150	50	0.90	7160	5.65	7.04	2.35	1.51	2100	0.14	“Y”
M	095-150-2-50	2.23	0.150	50	0.95	6710	8.64	10.1	1.33	1.00	4000	0.32	“X”
M	100-150-2-50	3.21	0.150	50	1.00	6180	8.64	10.3	0.99	1.06	3370	0.47	“X”
M	105-150-2-50	4.33	0.150	50	1.05	5300	13.6	14.7	0.73	1.04	3360	0.71	“X”
M	110-150-2-50	6.17	0.150	50	1.10	4930	14.8	15.4	0.45	1.03	3190	0.69	“D”

**Table 1**  
(Continued)

Group	Model	$\rho_c$	$M_{\text{He}}$	$R_{\text{seed}}$	$M$	$R$	$E_{\text{fin}}$	$E_{\text{nuc}}$	$t_{\text{det}}$	$\rho_{\text{det}}$	$R_{\text{det}}$	$M_{\text{Ni}}$	Type
M	115-150-2-50	9.19	0.150	50	1.15	4550	16.5	17.7	0.33	1.09	2910	0.86	“D”
M	120-150-2-50	14.8	0.150	50	1.20	4250	18.9	22.1	0.26	1.56	2570	0.96	“D”

**Note.**  $E_{\text{nuc}}$  and  $E_{\text{tot}}$  are the energy released by nuclear reaction and the total energy, respectively, in units of  $10^{50}$  erg.  $M$ ,  $M_{\text{He}}$ , and  $M_{\text{Ni}}$  are the masses of the initial WD model, initial He envelope, and the final synthesized  $^{56}\text{Ni}$ , respectively in units of  $M_{\odot}$ .  $R$ ,  $R_{\text{seed}}$ , and  $R_{\text{det}}$  are the radii of the initial WD model, the distance of the initial detonation seed from the He/CO interface, and the radius where the second detonation is started, respectively, in units of km.  $t_{\text{det}}$  is the time when the second detonation is triggered.  $\rho_c$  and  $\rho_{\text{det}}$  are the initial central density and the density at which the second detonation is triggered, respectively, in units of  $10^7 \text{ g cm}^{-3}$ . The category “Type” classifies the final results into five types. “N” stands for no second detonation induced. “Y” stands for the second detonation that starts at a location closer to the  $z$ -axis (the rotation symmetry axis). “X” stands for the second detonation that starts at a location closer to the  $r$ -axis (the symmetry plane axis). “D” stands for the second detonation that starts somewhere between “Y” and “X.” “S” stands for the central detonation.

**Table 2**

Models for the Study of Reflection Symmetry Effects in the Sub-Chandrasekhar SNe Ia

Model	Delay Time	C-det?	Position	$t_{\text{C-det}}$	$\rho_{\text{C-det}}$	$T_{\text{C-det}}$
Test-QS	0	Yes	(3420, 0)	0.94	1.04	2.55
Test-HS-0	0	Yes	(3380, 0)	0.94	1.06	2.84
Test-HS-1	0.2	Yes	(3290, -720)	1.03	1.09	2.83
Test-HS-2	0.4	Yes	(3120, -1400)	1.15	1.04	2.89
Test-HS-3	1.0	Yes	(1330, -2910)	1.43	1.00	2.00

**Note.** Delay time is the difference between the two He detonation bubbles in units of s. “C-det?” corresponds to whether C detonation can be triggered or not. If yes,  $\rho_{\text{C-det}}$  and  $T_{\text{C-det}}$  are the density and temperature of the triggered grid in units of  $10^7 \text{ g cm}^{-3}$  and  $10^9 \text{ K}$ , respectively.  $t_{\text{C-det}}$  is the ignition time in units of s. Position is the coordinate in units of km.

**Table 3**

Model Parameters for the One-dimensional Resolution Study

Model	$\Delta x$	$M$	$M_{\text{He}}$	$t_{\text{burn}}$	$E_{\text{fin}}$	$T_{\text{max}}$
Test1-fine	7.5	1.1	0.1	0.31	15.9	7.0
Test1	15.0	1.1	0.1	0.34 (9.6)	15.8 (0.63)	6.6 (5.7)
Test1-coarse	30.0	1.1	0.1	0.38 (11.8)	15.3 (3.2)	6.2 (6.1)

**Note.**  $M$  and  $M_{\text{He}}$  are in units of  $M_{\odot}$ .  $\Delta x$  is grid size in units of km.  $t_{\text{burn}}$  is the time needed for the C-detonation wave to burn everything in units of s.  $E_{\text{fin}}$  is the final asymptotic energy given by the simulation, in units of  $10^{50}$  erg.  $T_{\text{max}}$  is the maximum central temperature experienced in the simulations. The numbers in parentheses stand for the percentage difference between that model and the higher-resolution model.

envelope without penetrating into the CO core. Depending on  $M_{\text{He}}$  and the interface density, different detonation types are observed.

#### 4.0.1. Type “N”

Type “N” (no detonation) stands for no second detonation occurring. Type “N” can be found in models with a thin He envelope; the shock wave sent by the He detonation is not strong enough to compress the matter at both the center and the

surface of the CO core. The CO core has a temperature always below the threshold temperature.

#### 4.0.2. Type “D”

Type “D” (diagonal) stands for the detonation first appearing somewhere other than the symmetry axis. Type “D” occurs for models with high progenitor masses. In these cases, the typical density of the interface can be as high as  $\sim 10^7 \text{ g cm}^{-3}$ .

In Figure 1 we plot the temperature and explosion geometry for Model 110-150-2-50 (D). When the detonation reaches the interface, the temperature of the CO matter can easily reach the critical temperature to start the CO detonation.

The temperature can reach  $3 \times 10^9 \text{ K}$ , where the shock penetrates. Notice that even the temperature in the other detonated part can reach  $\sim 2 \times 10^9 \text{ K}$ . The propagation is along the isodensity contour, where there is almost no heating in the radial direction. This makes no heating in the CO material. Therefore, while the He detonation is still burning the matter in the envelope, the second detonation is already triggered.

#### 4.0.3. Type “X”

Types “Y” and “X” stand for the detonation that is first started along the rotation axis (in  $x$ - $y$  plane the  $y$ -axis) and symmetry axis (in  $x$ - $y$  plane the  $x$ -axis).

Type “X” occurs when Type “D” cannot be started. This applies to models with lower  $M$ . Notice that in our simulations, a quarter of the star is simulated. When the detonation propagates, its burning rate increases owing to the ring-shape structure, which has a local volume proportional to  $r$ . When the detonation approaches the symmetry axis, the high-velocity flow creates a strong compression of the remaining fuel. By symmetry, part of the fuel is compressed toward the core. This heats up the near-interface material and provides the required temperature for the first spot.

Figure 2 shows a typical “X”-type detonation for Model 110-100-2-50 (X). The second detonation is triggered at the  $r$ -axis, where the detonation wave compresses materials. The temperature due to the compression at the  $r$ -axis can be higher than the temperature rise in other regions due to detonation heating. As an example, the actual temperature can reach  $3 \times 10^9 \text{ K}$  near the  $r$ -axis, compared to other region, which is  $\sim 2 \times 10^9 \text{ K}$ . We remark that this shock heating is not related to the geometric convergence. Here the detonation waves approach the symmetry boundary, i.e., two laminar detonation waves approaching each other (the collision site along the equator is locally flat).

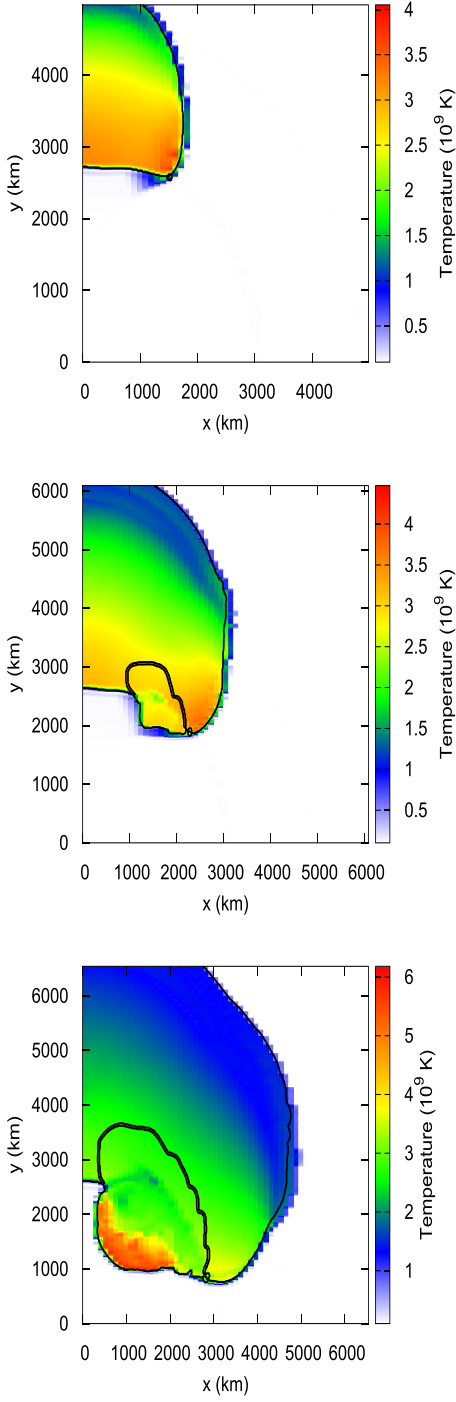


**Figure 1.** Flame and detonation geometry and the temperature for Model 110-200-2-R50 (D). The detonation is captured at  $-0.34$ ,  $0.03$ ,  $0.15$ , and  $0.40$  s from the detonation transition.

#### 4.0.4. Type “Y”

In Figure 3 we demonstrate the “Y”-type detonation by using Model 110-050-2-B50 (Y) as an example. Type “Y” occurs when both Type “X” and Type “D” cannot be triggered beforehand. After the He shell is fully burnt, the first converging shock is not strong enough to detonate CO matter near the interface. Instead, the mild shock continues to travel along the density contour in the envelope. The flow creates

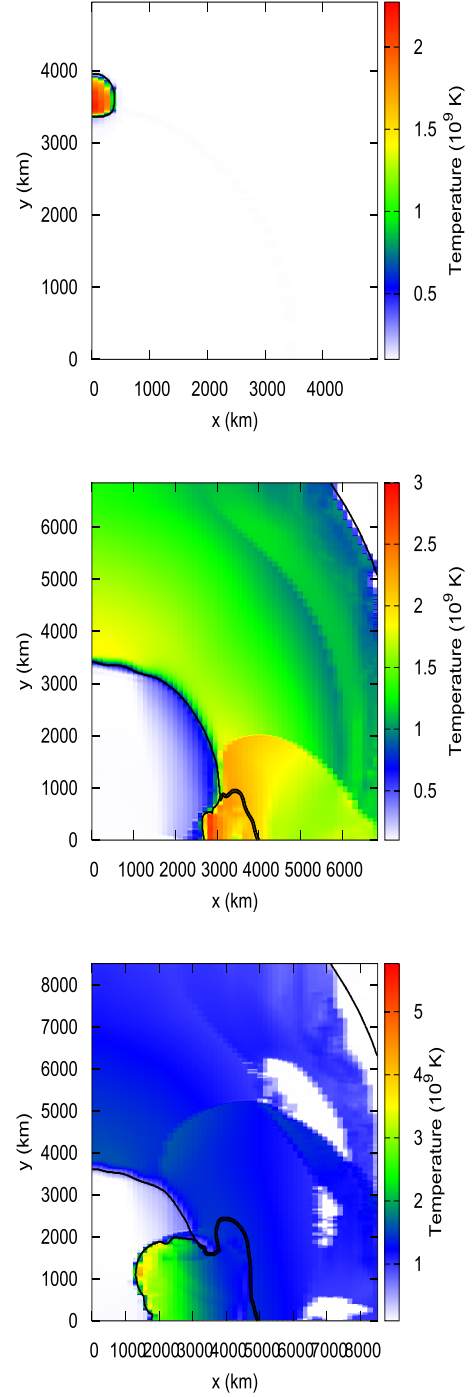


**Figure 2.** Similar to Figure 1, but for Model 110-100-2-R50 (Type “X”). The detonation is captured at  $-0.82$ ,  $0.15$ , and  $0.40$  s from the detonation transition.

another converging shock when the shock front returns to the rotation axis, which again creates the first hot spot for the C detonation.

#### 4.0.5. Type “S”

Type “S” can be found in models with detonation seeds that have spherical symmetry, while the He envelope is not massive enough to ignite the near-interface C. The converging shock



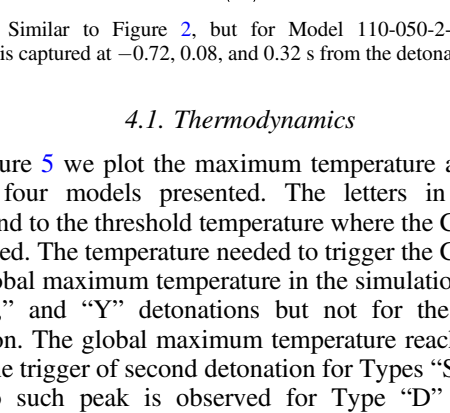
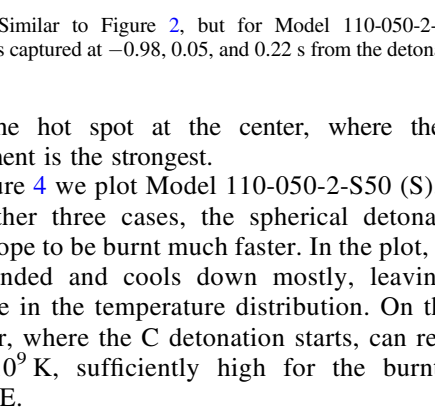
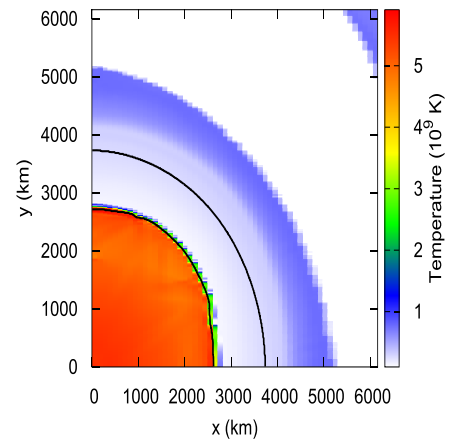
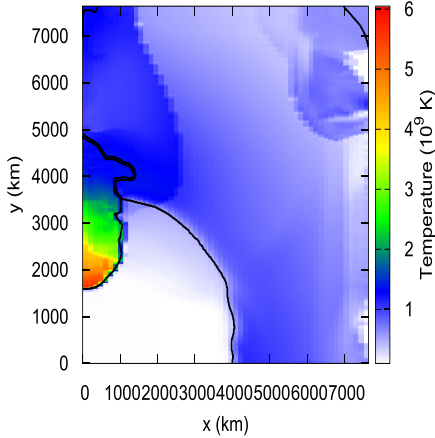
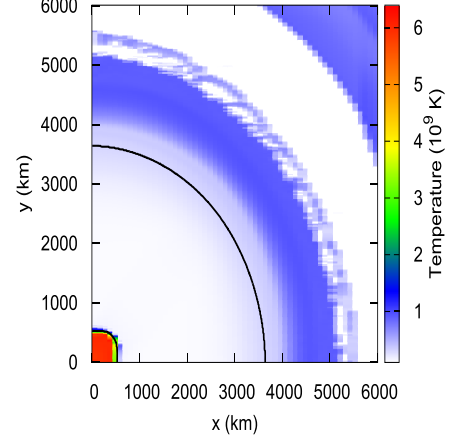
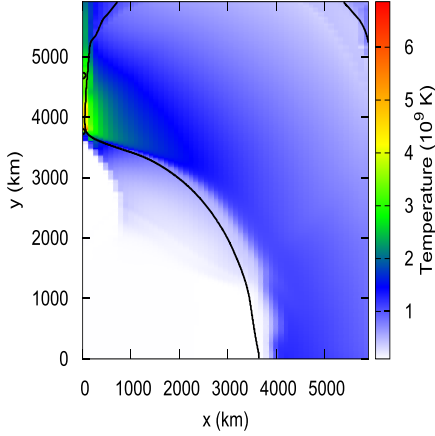
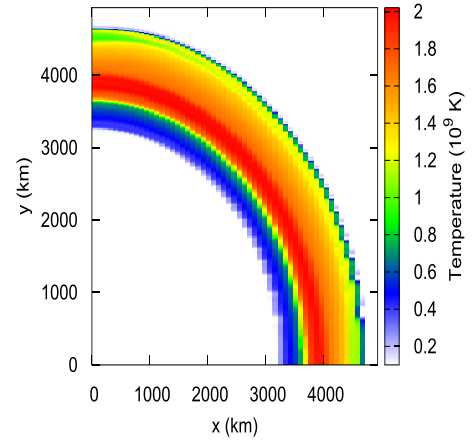
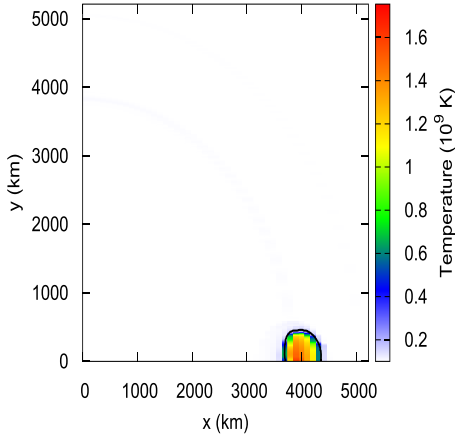


**Figure 3.** Similar to Figure 2, but for Model 110-050-2-B50 (Y). The detonation is captured at  $-0.98$ ,  $0.05$ , and  $0.22$  s from the detonation transition.

**Figure 4.** Similar to Figure 2, but for Model 110-050-2-S50 (S). The detonation is captured at  $-0.72$ ,  $0.08$ , and  $0.32$  s from the detonation transition.

creates the hot spot at the center, where the geometric enhancement is the strongest.

In Figure 4 we plot Model 110-050-2-S50 (S). In contrast to the other three cases, the spherical detonation allows the envelope to be burnt much faster. In the plot, the He shell has expanded and cools down mostly, leaving almost a mild trace in the temperature distribution. On the contrary, the center, where the C detonation starts, can reach as high as  $6 \times 10^9$  K, sufficiently high for the burnt matter to reach NSE.

#### 4.1. Thermodynamics

In Figure 5 we plot the maximum temperature against time for the four models presented. The letters in the figure correspond to the threshold temperature where the C detonation is triggered. The temperature needed to trigger the C detonation is the global maximum temperature in the simulations for Type “S,” “X,” and “Y” detonations but not for the Type “D” detonation. The global maximum temperature reaches its peak during the trigger of second detonation for Types “S,” “X,” and “Y.” No such peak is observed for Type “D” detonation.

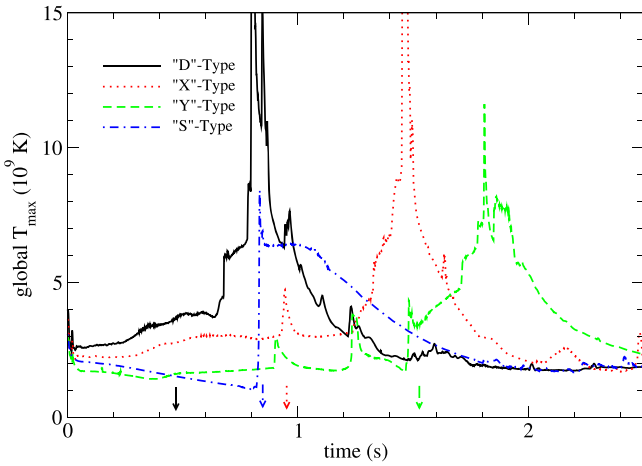


**Figure 5.** Maximum temperature in the simulations against time for Models 110-150-2-50 (D), 110-100-2-50 (X), 110-100-2-2R50 (Y), and 110-050-2-S50 (S), respectively. The arrows stand for the time where DDT is triggered for each model.

Furthermore for Type “S” detonation, the maximum temperature when the C detonation is triggered is the highest temperature reached in the simulation. This means that for a nonspherical trigger, even the hot ash can be higher than the threshold temperature, unless certain shock convergence occurs, in which case the CO matter near the interface can remain at a temperature below the critical temperature.

Another feature is that in most cases, when the C detonation approaches the center, nuclear burning, despite its low density, can be enhanced when the convergence effect is strong. This effect is robust under different resolution, and is even stronger when a finer resolution is used. This is because the shock strength can increase in the way of  $\sim 1/r$  for a cylindrical detonation and  $\sim 1/r^2$  for a spherical. Locally, the density growth in the core will be higher for a finer-resolution run, which allows more rapid reactions. However, globally the energy production will not diverge because the finer the resolution is, the smaller contribution such a temperature peak gives. On the other hand, by using different geometry (e.g., Cartesian coordinate) or higher dimensions (i.e., three-dimensional model), the level of shock convergence will be changed because it depends on how the geometry describes the structure with a high symmetry such as a ring or a sphere.

The peak temperature, albeit contributing to an extremely small amount of mass ( $\sim 10^{-8-11} M_{\odot}$ ), can reach above  $10^{10}$  K. One feature in “Y”-type detonation does not appear in other types of detonation, namely, the multiple peaks prior to detonation. This reflects the shock interaction from multiple detonations. For example, they correspond to the first collision of He detonations and the arrival of the reflected shock on the  $r$ -axis and the  $z$ -axis, respectively.

This shows that the exact peak temperature can vary a lot depending on the geometric convergence. But how the convergence of shock and its subsequent divergence in temperature take place are related to the spatial resolution. In Appendix D we perform a numerical study to see how the spatial resolution affects the thermodynamics properties in local and global properties in some of the explosion models.

Below, we discuss the hydrodynamics behavior of these models.

#### 4.1.1. Effects of He Envelope Mass

In Groups D, E, F, and M we cover the effects of  $M_{\text{He}}$  for different progenitor masses from 0.9 to  $1.2 M_{\odot}$ . Some common trends can be seen in these series. At low  $M_{\text{He}}$ , no second detonation can be triggered. By increasing  $M_{\text{He}}$ , the second detonation can be triggered by “Y”-type, “X”-type, and then “D”-type in ascending  $M_{\text{He}}$ . The created  $^{56}\text{Ni}$  increases with  $M_{\text{He}}$ . The explosion energy follows the same trend. Due to the change of detonation channel, the detonation trigger time becomes earlier for a higher  $M_{\text{He}}$ . We remark that “S” type is independent from the other three detonation types because it requires always a spherical He detonation independent of  $M_{\text{He}}$ . Models with a high  $M_{\text{He}}$  favor the “D”-type detonation. For  $M \geq 1.0 M_{\odot}$ , transition from “X”-type to “D”-type detonation occurs when  $M_{\text{He}} > 0.1\text{--}0.15 M_{\odot}$ . For  $M \leq 1.0 M_{\odot}$ , transition from “Y”-type to “X”-type and then “D”-type detonation takes place for the transition  $M_{\text{He}}$  at 0.15 and  $0.2 M_{\odot}$ , respectively. The critical  $M_{\text{He}}$  where no second detonation takes place depends on  $M$ , which decreases when  $M$  increases, and the detonation geometry. He detonation with rotation or spherical geometry can trigger the second detonation with  $M_{\text{He}}$  as low as  $0.05 M_{\odot}$ . For other types of He detonation, the minimum value of  $M_{\text{He}}$  is  $\sim 0.15 M_{\odot}$  for  $M = 0.9\text{--}1.0 M_{\odot}$ ,  $0.1 M_{\odot}$  for  $M = 1.1 M_{\odot}$  and  $0.05 M_{\odot}$  for  $M = 1.2 M_{\odot}$ .

#### 4.1.2. Effects of Metallicity

In Groups H, I, and J we cover the effects of  $Z$  for three different models. The latter two are the benchmark models decided by its  $M_{\text{Ni}}$  at solar metallicity. We can see that metallicity has a very mild influence on the explosion energy and final energy. The detonation position, its channel, and its trigger time are insensitive to  $Z$ . The major difference can be seen from the  $^{56}\text{Ni}$  mass, which drops when  $Z$  increases.

#### 4.1.3. Effects of Detonation Pattern

In Groups K and L we explore the effects of the detonation pattern, determined by its initial He detonation spot and its geometry. Again, all models share the same  $M$ ,  $M_{\text{He}}$ , and  $Z$ . The initial He detonation spot has almost no impact on the explosion energetics and explosion properties. The Ni production is also insensitive to the change of detonation position. On the other hand, the choice of detonation geometry influences greatly the explosion properties. Some models (Models 105-050-2-50 (N) and 105-050-2-3R50 (N)) cannot trigger C detonation spontaneously, while some (Models 105-050-2-S50 (S) and 105-050-2-2R50 (Y)) can. This reflects that the symmetry of the initial shock and how the detonation waves collide with each other determine the final fate of the WD. The resultant  $M_{\text{Ni}}$  can vary from  $\sim 10^{-2} M_{\odot}$  in a failed detonation to  $\sim 0.5 M_{\odot}$  in a successful detonation. We note that Models 105-050-2-3R50 (N) and 105-050-2-2R50 (Y) behave differently. To show that the result is robust in our study, in Appendix E we do a resolution study to demonstrate how the trigger of C detonation depends on the spatial resolution.

#### 4.1.4. Effects of Initial Mass

In Group J we explore the effects of  $M$  on the explosion energetics. Compared to the near-Chandrasekhar-mass WD studied in Leung & Nomoto (2018), the mass range for sub-Chandrasekhar mass is much wider (from 0.9 to  $1.2 M_{\odot}$ ). We

do not explore mass below  $0.9 M_{\odot}$  since the central density of these models is below  $10^7 \text{ g cm}^{-3}$ , where the incomplete burning dominates. We also do not extend the upper bound to  $1.3 M_{\odot}$  since it is unclear, if there is nuclear runaway, whether the explosion is carried out as deflagration or detonation (Nomoto et al. 1976; Nomoto 1982b; Nomoto et al. 1984). We can see that when  $M$  increases, some effects are similar to increasing  $M_{\text{He}}$ . The explosion energy increases. Also, the explosion time becomes earlier, with its position being closer to the core. The detonation channel also changes from Type “Y” to Type “X” and then Type “D.”

## 5. Benchmark Models

In this section, we study in detail some models that behave most similarly to a standard SN Ia, determined by their  $^{56}\text{Ni}$  production, which should be  $\sim 0.6 M_{\odot}$  as observed in the majority of normal SNe Ia. Since there is a degeneracy in the models to produce this feature, we pick the one with the lowest amount of  $M_{\text{He}}$ . We selected Models 110-100-2-50 (X), 100-050-2-S50 (S), and 110-050-2-B50 (Y). All of them have a healthy explosion of  $^{56}\text{Ni}$  mass,  $\sim 0.6 M_{\odot}$ .

In contrast, for sub-Chandrasekhar-mass WDs, we do not impose the constraints of Mn and Ni as we have done in Leung & Nomoto (2018) because all models we built always underproduce Mn and Ni. Chosen by the  $^{56}\text{Ni}$  production, there exists a degeneracy of models that satisfy this constraint. As a result, from each detonation trigger, we choose one model with  $M_{\text{Ni}} = 0.6 M_{\odot}$ . They include Models 110-100-2-50 (X), 105-050-2-B50 (Y), and 100-050-2-S50 (S). No model with Type “D” produces an explosion with  $M(^{56}\text{Ni}) \sim 0.6 M_{\odot}$ .

### 5.1. Energy Evolution

In Figure 6 we plot the time evolution of the total energy, kinetic energy, internal energy, and gravitational energy for the benchmark models. Here we give an analysis on the energy evolution of only Model 110-100-2-50 (X). The other two benchmark models have similar evolution to this one, except with different detonation triggers and different He detonation convergence effects.

Before 0.9 s, there is only He detonation. The energy release  $\sim 1 \times 10^{50} \text{ erg}$  is insufficient to unbound the star owing to the small amount of He and its low density. There is almost no change in the gravitational energy and kinetic energy. Almost all of the energy change is reflected in the change of internal energy, showing that the He detonation does not influence the global dynamics. From 0.9 to 1.6 s C detonation takes place. The total energy sharply increases by  $10^{51} \text{ erg}$  at  $\sim 1.3 \text{ s}$ , showing that the C detonation is rapidly turning the CO fuel into ash. At the same time, the internal energy drops while internal energy and gravitational energy increase and reach their equilibrium values at  $\sim 2 \text{ s}$ . This corresponds to the phase in which the thermalized ash is quickly expanding to accelerate the matter outward until homologous expansion is developed.

### 5.2. Luminosity Evolution

In Figure 7 we plot the luminosity of the three benchmark models 110-100-2-50 (X), 110-050-2-B50 (Y), 100-050-2-S50 (S)

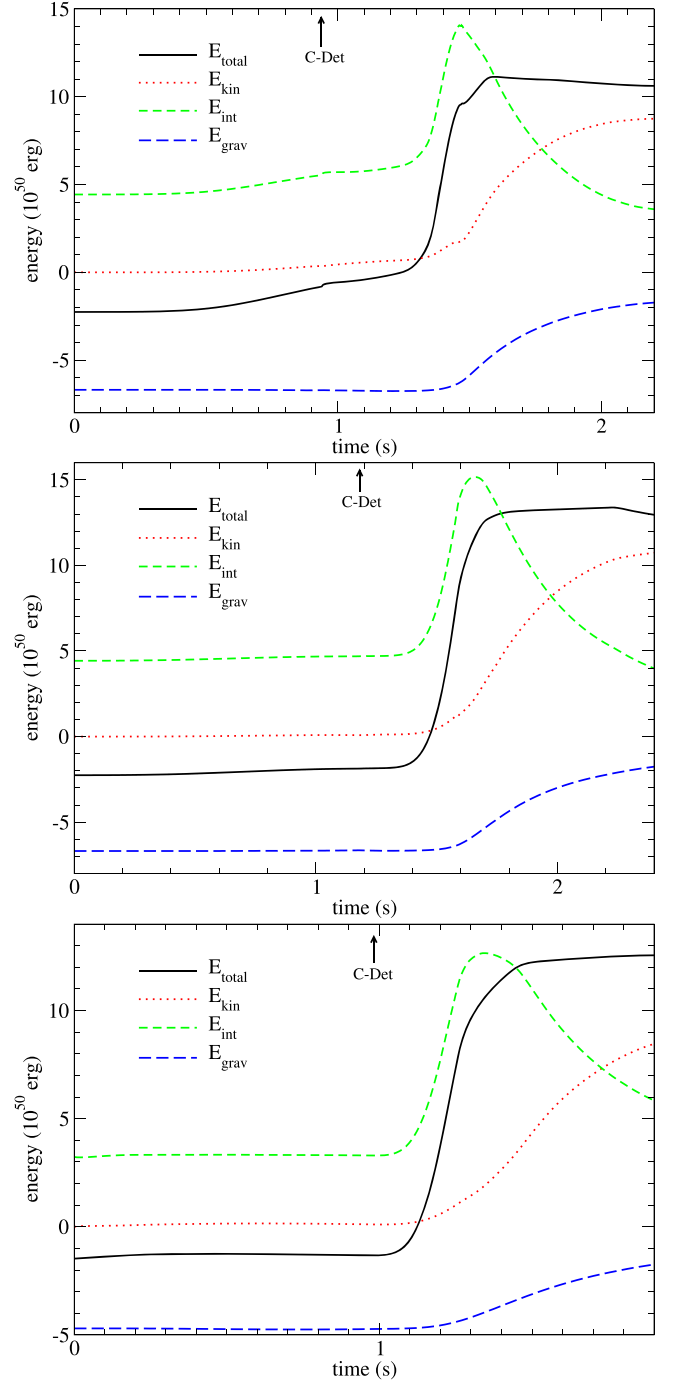


**Figure 6.** Total energy, kinetic energy, internal energy, and gravitational energy against time for Models 110-100-2-50 (X) (top panel), 110-050-2-B50 (Y) (middle panel), and 100-050-2-S50 (S) (bottom panel).

in the top, middle, and bottom panels, respectively. First, we analyze the evolution of Model 110-100-2-50 (X).

Before 0.9 s, the total luminosity and the He detonation overlap with each other. This means that most energy is produced directly from detonation where NQSE and NSE do not actively contribute to the energy evolution. There is a peak at 0.9 s, which is the moment where the He detonation reaches the symmetry axis. The compression causes a sudden jump in the density and temperature, which allows He burning to proceed much more efficiently. After that, the He detonation ceases, as there is not any pure He left but only partially burnt



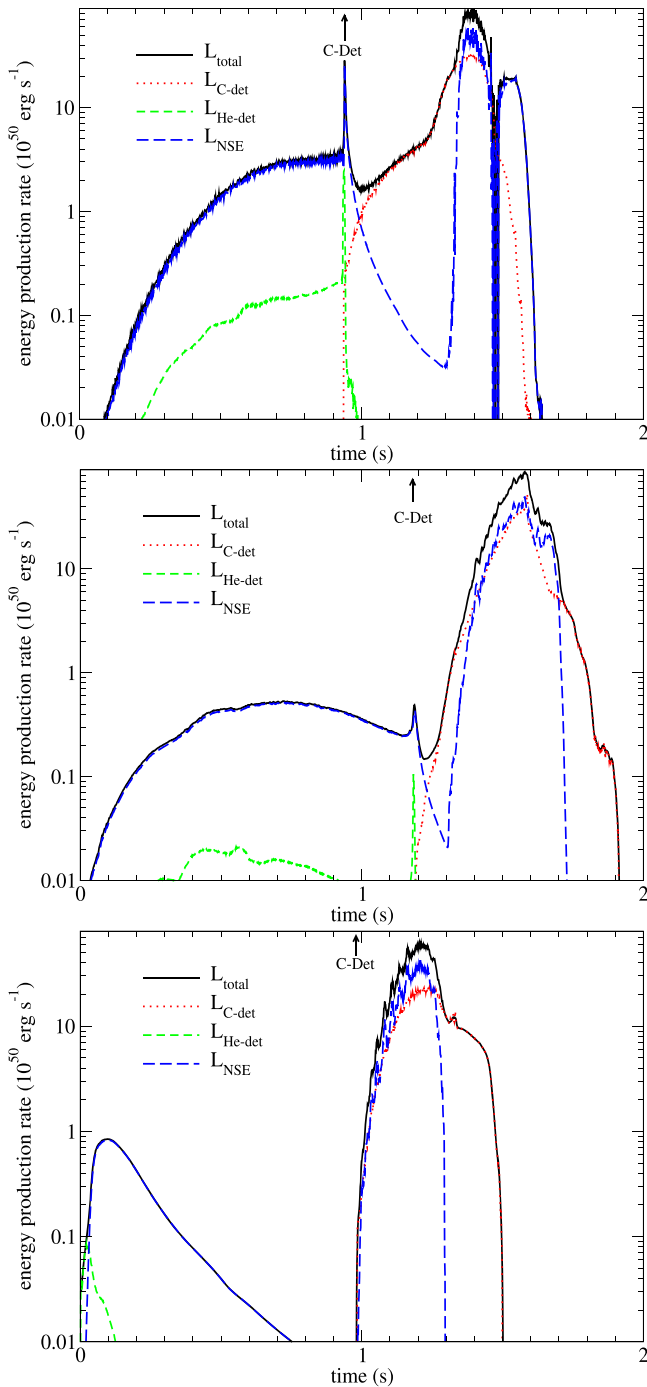


**Figure 7.** Total luminosity, C detonation luminosity, He detonation luminosity, and NSE burning luminosity against time for Models 110-100-2-50 (X) (top panel), 110-050-2-B50 (Y) (middle panel), and 100-050-2-S50 (S) (bottom panel).

He in the ash. At  $t = 0.9$  s, the C burning takes place in the major nuclear reactions. But there is no advanced burning, showing that the detonation is still incinerating material in the low-density region. At  $t = 1.5$  s, the advanced burning exceeds the C detonation to become the major energy production channel. This shows that the detonation has finally reached the center, which is dense and hot enough to carry out silicon burning up to NSE. Around 1.5 s, the C detonation begins to cease. Also, beyond 1.6 s, all matter becomes too cold or of too low density for further exothermic nuclear reactions to occur.

Model 110-050-2-B50 (Y) has a similar evolution to Model 110-100-2-50 (X) but has the “Y”-type detonation. The shapes of the energy production rates are similar, but with two major differences. However, the delay between the C detonation and NSE luminosity rise is shorter than in the Type-“X” detonation model. This feature is similar to the “S”-type detonation (see below), despite its off-center ignition. One reason is that during the geometric convergence, it not only heats up the CO-rich matter below the interface but also generates a strong inward flow, which helps to guide the detonation reaching the high-density region. Such channeling is weaker in the “X”-type model owing to the absence of geometric convergence.

Model 110-050-2-S50 (S) is the “S”-type detonation. It has a different structure from the other two by the absence of an He-burning peak at the onset of second detonation and the similarity between the total luminosity and that by the NSE burning. Due to the detonation symmetry, there is no geometric convergence for the He detonation. The He detonation creates an inward-moving shock while propagating outward to burn the remaining He. Hence, no luminosity peak during the transition is observed. Then, after the C detonation is triggered, the total energy release, NSE burning, and C burning closely follow each other. This is because the detonation starts from the center. The higher density compared to the envelope allows the burning to reach NSE in much shorter than the dynamical timescale. This feature is not observed in Type-“X”- or Type-“Y” detonation. At 1.3 s the energy production by C burning drops rapidly, showing that the detonation wave has finished sweeping all C fuel in the star. Accompanying with the expansion of the star, the recombination of  $^4\text{He}$  into  $^{56}\text{Ni}$  becomes the only energy production, which also ceases at 1.5 s.

### 5.3. Chemical Abundance

We use the tracer particle scheme to reconstruct the detailed nucleosynthesis. The massless tracers are advected by the fluid motion but have no effect on the fluid. They record the local density and temperature accordingly. Here we examine the typical chemical abundances of the three benchmark models presented in previous parts.

In Figure 8 we plot the final chemical abundance of the three benchmark models mentioned above.  $[X_i/^{56}\text{Fe}]$  is defined as  $\log_{10}(X_i/X(^{56}\text{Fe})) - \log_{10}(X_i/X(^{56}\text{Fe}))_{\odot}$ .

For Model 110-100-2-50 (X), the intermediate-mass elements (IMEs) up to  $^{40}\text{Ca}$  are underproduced. Starting from Ti, the production becomes similar to the solar abundance, where some of them are even overproduced, including  $^{48}\text{Ti}$ ,  $^{51}\text{V}$ , and  $^{52}\text{Cr}$ . They are from three to six times higher than the observed solar values. Most Fe and Ni isotopes are very close to the solar values. Isotopes beyond Ni are underproduced. The pattern for Ni where  $^{60}\text{Ni}$  and  $^{62}\text{Ni}$  are more abundant can be observed. Also, as expected,  $^{55}\text{Mn}$ , which comes mostly from the low electron fraction matter, is underproduced. In order to produce Mn, two channels are possible. First, Mn can be directly formed from NSE when the electron fraction of the matter is  $Y_e = 0.45$ . Second, it is formed during alpha-chain burning of  $^{52}\text{Fe}$ , where  $^{52}\text{Fe}(\alpha, p)^{55}\text{Co}$ . The  $^{55}\text{Co}$  will later decay by  $^{55}\text{Co}(e^-, \nu_e)^{55}\text{Fe}(e^-, \nu_e)^{55}\text{Mn}$ . The formation of  $^{55}\text{Co}$  is favorable at  $Y_e = 0.49$ . For pure C+O matter,  $Y_e = 0.5$ , therefore directly NSE burning without electron capture or alpha-chain burning cannot form seeds of  $^{55}\text{Mn}$ , which is the case of the sub-Chandrasekhar-mass model.

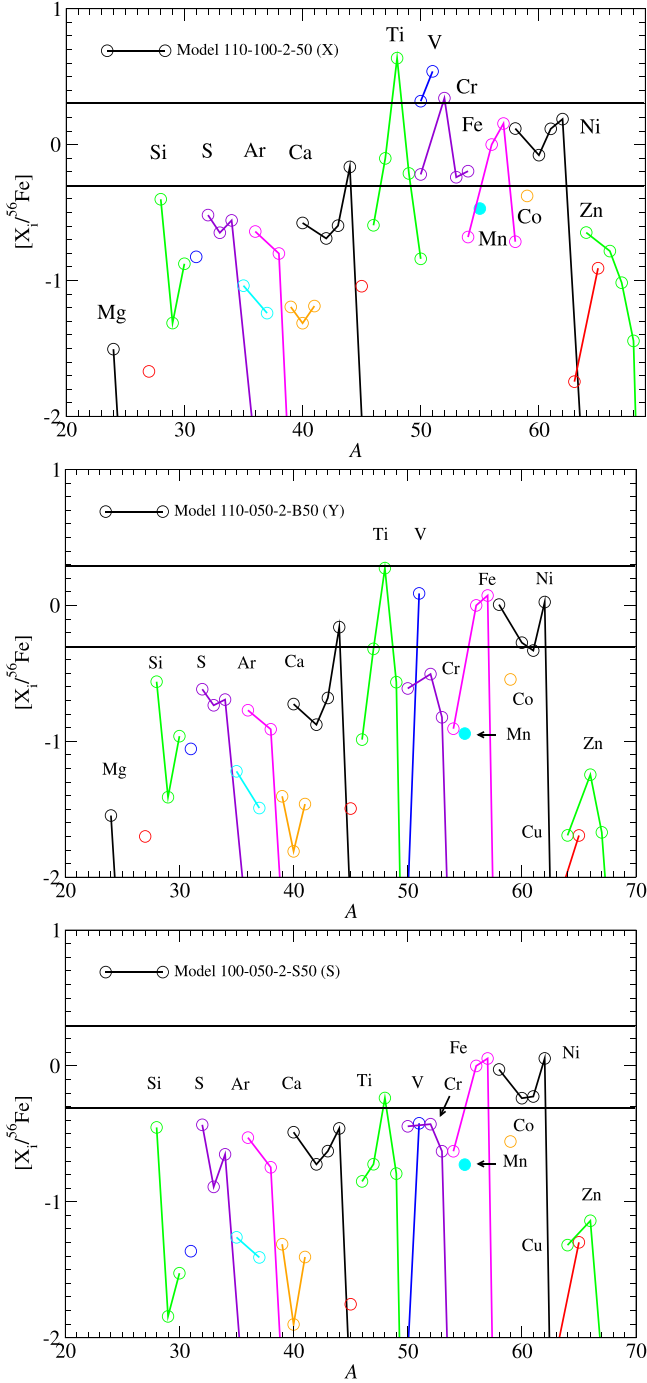


**Figure 8.**  $[X_i/^{56}\text{Fe}]$  after all short-lived isotopes have decayed for Models 110-100-2-50 (X) (top panel), 110-050-2-B50 (Y) (middle panel), and 100-050-2-S50 (S) (bottom panel).  $[X_i/^{56}\text{Fe}]$  is defined as  $\log_{10}(X_i/X(^{56}\text{Fe})) - \log_{10}(X_i/X(^{56}\text{Fe}))_{\odot}$ . The upper and lower horizontal lines stand for two times and half of the solar value.

For Model 110-050-2-B50 (Y), the nucleosynthesis pattern is very similar to the previous model. There are minor variations, such as the much lower  $^{50}\text{V}$ , and no trace of  $^{54}\text{Cr}$ . This is because there is no shock convergence by the C detonation in the core due to the propagation direction. The effects of the hot spot become less significant in this benchmark model.

For Model 100-050-2-S50 (S), the nucleosynthesis pattern is very different from that of the previous two models. Due to the imposed He detonation symmetry, a much lower amount of He

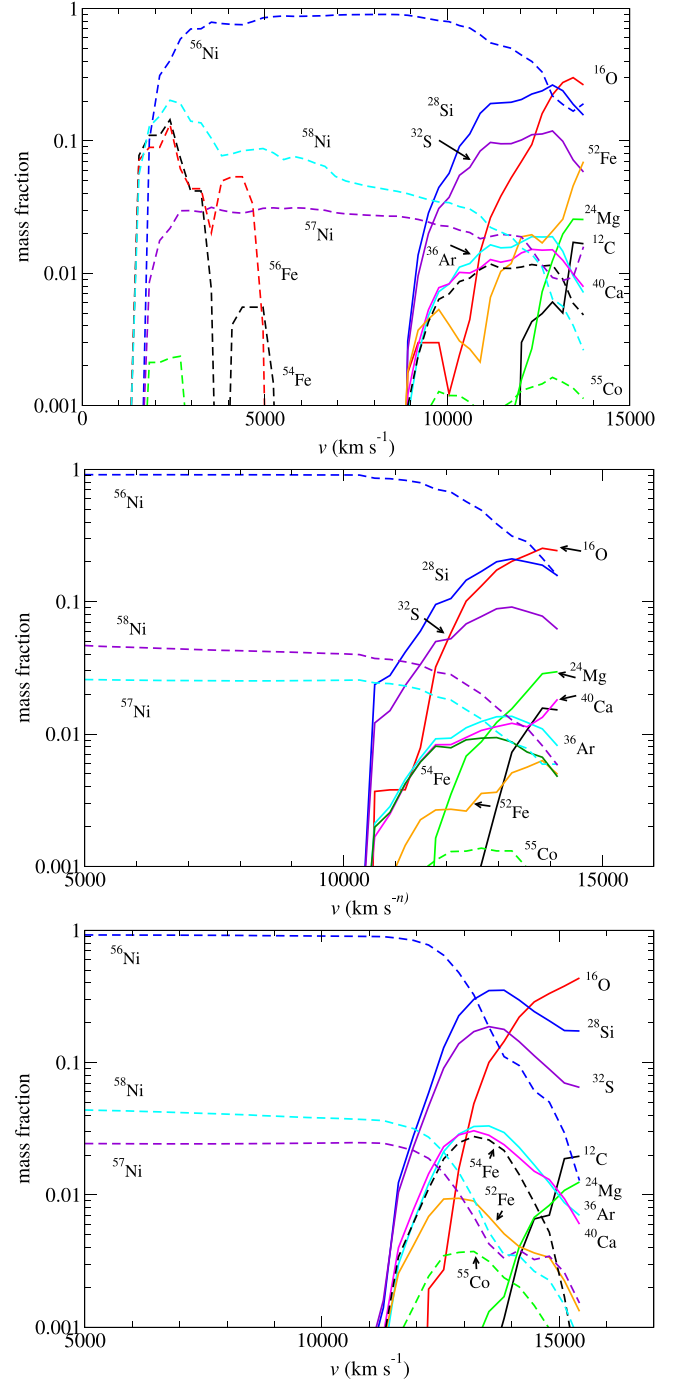


**Figure 9.** Mass fraction against velocity of the final abundance before the decay of short-lived isotopes for the benchmark models 110-100-2-50 (X) (top panel), 105-100-2-B50 (Y) (middle panel), and 100-050-2-S50 (S) (bottom panel).

envelope mass is needed to trigger the C detonation. As a result, the resultant chemical pattern, related to He burning, is highly suppressed. A major drop of the abundances in  $^{47-48}\text{Ti}$ ,  $^{51}\text{V}$ , and  $^{52}\text{Cr}$  becomes solar or even subsolar. Other abundances, which are basically the C detonation products, remain the same as the other two models.

#### 5.4. Ejecta Composition

In Figure 9 we plot the velocity distribution of some representative isotopes for the benchmark Models 110-100-2-

50 (X), 110-050-2-B50 (Y), and 100-050-2-S50 (S) in the top, middle, and bottom panels, respectively. We extract the chemical abundances and velocities of the tracer particles.

In Model 110-100-2-50 (X), this benchmark model possesses the typical sub-Chandrasekhar-mass SN Ia ejecta profile with asymmetric effects. Here, we refer to, e.g., Shigeyama et al. (1992) for a typical sub-Chandrasekhar-mass SN Ia. For the typical one, we can see that in the core, up to  $10,000 \text{ km s}^{-1}$ , the ejecta is made of mainly  $^{56-58}\text{Ni}$ . Beyond that, IMEs, including  $^{28}\text{Si}$ ,  $^{32}\text{S}$ ,  $^{36}\text{Ar}$ , and  $^{40}\text{Ca}$ , become more abundant. However, in this model  $^{56}\text{Ni}$  remains the most abundant almost throughout the star within  $v < 13,000 \text{ km s}^{-1}$ . Traces of  $^{12}\text{C}$  and  $^{16}\text{O}$  can be found when  $v > 12,000 \text{ km s}^{-1}$ . They correspond to the products from the incomplete C burning. These features are common to all three benchmark models presented here.

In Models 110-100-2-50 (X) and 110-050-2-B50 (Y), we can see a mild rise of  $^{52}\text{Fe}$  near the surface. Also,  $^{54}\text{Fe}$  remains to maintain a few percent mass fraction even to the outermost ejecta. They come from He burning, especially when there is shock convergence or detonation wave collision. The further compressional heating with this hydrodynamical origin can enhance the formation of these isotopes. On the other hand, we see a clear cut of  $^{54}\text{Fe}$  inside the outermost ejecta of Model 100-050-2-S50, and  $^{52}\text{Fe}$  has a clear falling trend when  $v > 13,000 \text{ km s}^{-1}$ .

Major differences appear in the innermost part of the ejecta because of the C detonation convergence. As discussed in previous sections, the further C-detonation-induced geometric convergence can create a hot spot that allows the matter to be heated up to a temperature above which it can normally reach through simple detonation. In that sense, this allows a small part of matter to undergo complete burning and even electron capture. This property can be found in Model 110-100-2-50 (X). We can see that at the innermost part of the ejecta, neutron-rich isotopes, including  $^{54}\text{Fe}$  and  $^{56}\text{Fe}$ , are produced. Some  $^{55}\text{Co}$  can even be produced. Notice that these features are usually found in the Chandrasekhar-mass model (see, e.g., Nomoto 1984; Iwamoto et al. 1999, for the detailed ejecta profile of some classical models). This demonstrates that the asphericity of the He detonation and hence the C detonation can be reflected by the low-velocity ejecta.

### 5.5. Thermodynamics

In Figure 10 we plot the  $\rho_{\text{max}}$  against  $T_{\text{max}}$  for the benchmark model obtained from the tracer particles. The sampling is done by grouping the tracer particles into bins according to their  $\rho_{\text{max}}$ , which is defined by their individual thermodynamics history. Then, the average, upper limit, and lower limit of  $T_{\text{max}}$  in each density bin are taken.  $T_{\text{max}}$  is also the maximum value in the thermodynamics history. In most cases, the particle achieves its  $\rho_{\text{max}}$  and  $T_{\text{max}}$  at the same time, when the detonation wave swept across the particle. However, in the case where multiple detonation shocks appear, the two moments can be nonsimultaneous. Notice that the initial central density of this model is  $\sim 6 \times 10^7 \text{ g cm}^{-3}$ . Due to the shock wave compression, which is further enhanced by the geometric convergence, as well as shock wave collision, the matter can reach a maximum density as high as  $3 \times 10^8 \text{ g cm}^{-3}$ . Together with the rise of the density, the temperature can rise as high as  $7 \times 10^9 \text{ K}$ . Certain particles that are directly under shock interaction can reach a maximum density of  $5 \times 10^8 \text{ g cm}^{-3}$  with a maximum temperature of  $9 \times 10^9 \text{ K}$ . This can be

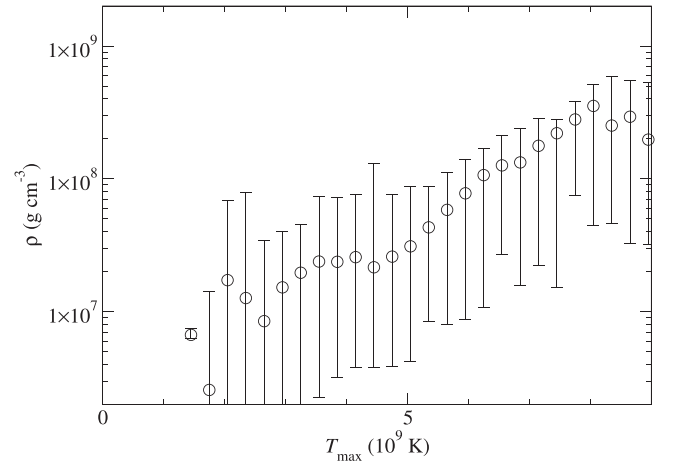


**Figure 10.** The  $\rho_{\text{max}}$  against  $T_{\text{max}}$  for the benchmark model obtained from the tracer particle thermodynamics histories for Model 110-100-2-50 (X). The error bars stand for the temperature ranges of the tracer particles at a specific density bin, with the circle being the average.

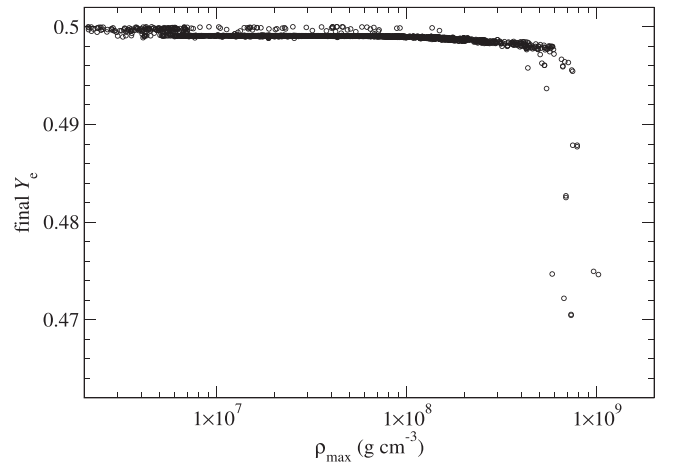


**Figure 11.** Same as Figure 10, but for the final  $Y_e$  against  $\rho_{\text{max}}$  for the benchmark model 110-100-2-50 (X) obtained from the tracer particle thermodynamics histories.

compared with Figure 12 in Leung & Nomoto (2018). In that figure, the tracer particles show a uniform  $\rho_{\text{max}}$  against  $T_{\text{max}}$  for the particles inside deflagration zones and a spread of  $T_{\text{max}}$  in the detonation zone. Our model here shows a similar behavior for the detonation, except that the effects are more pronounced because of the inward motion during the shock propagation.

At last, in Figure 11 we plot also the final  $Y_e$  of the tracer particles against  $T_{\text{max}}$ . We can see three groups of particles. The first group is the particle from the He envelope. It has a uniform final  $Y_e = 0.5$ , which has a density from  $10^6$  to  $10^8 \text{ g cm}^{-3}$ . This shows that the He envelope has in general low density where electron capture processes are inefficient. The second group is the  $10^6$ – $5 \times 10^8 \text{ g cm}^{-3}$ . This corresponds to the tracer particles experiencing a single pass of detonation wave. The final  $Y_e$  shows a mildly decreasing function as  $\rho_{\text{max}}$ , which suggests that electron capture becomes important near  $10^8 \text{ g cm}^{-3}$ . The third group of particles are those with  $Y_e$  from 0.47 to 0.495 with a  $\rho_{\text{max}}$  from 5 to  $10 \times 10^8 \text{ g cm}^{-3}$ . This corresponds to tracer particles that are excited by shock compression. There are much fewer particles of this type since it occurs to the particles very close to the symmetry boundary



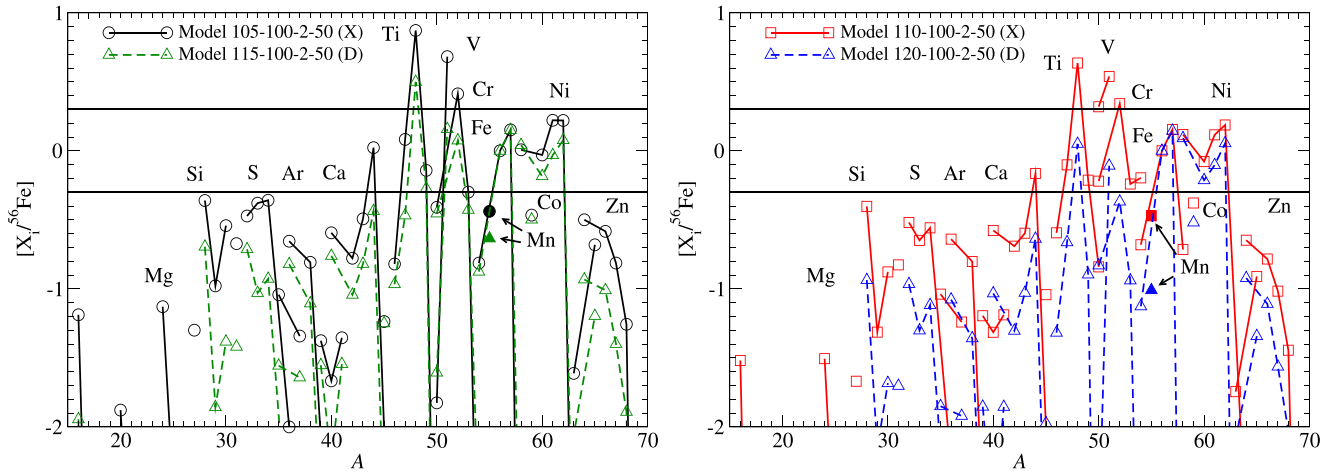


**Figure 12.**  $[X_i/^{56}\text{Fe}]$  for Models 105-100-2-50 (X) ( $M = 1.05 M_\odot$ ) and 115-100-2-50 (D) ( $M = 1.15 M_\odot$ ) in the left panel and Models 110-100-2-50 (X) ( $M = 1.10 M_\odot$ ) and 120-100-2-50 (D) ( $M = 1.20 M_\odot$ ) in the right panel. All models assume  $M_{\text{He}} = 0.1 M_\odot$ ,  $Z = 0.02$ , and a bubble-shape initial He detonation at 50 km above the CO-envelope interface.

or lying inside the collision site of C detonation shock. Again, this figure can be compared with Figure 12 in Leung & Nomoto (2018). In that figure, the distribution of particles is more uniform and there exists a one-to-one correspondence for a given  $\rho_{\text{max}}$  to final  $Y_e$ . In this work, this correspondence is broken down because of the He envelope. Also, the pronounced shock interactions provide a wider diversity to the thermodynamics history in the tracer particles.

## 6. Nucleosynthesis

To calibrate the nucleosynthesis yield, we use the post-process scheme as described in Travaglio et al. (2004) and Seitenzahl et al. (2010). In the hydrodynamics simulations we place massless particles that record the thermodynamics history of the local density and temperature of the Eulerian grid. The density and temperature evolution, together with the initial chemical composition depending on its initial position, are sent to the nuclear reaction network to calculate the chemical abundance of the corresponding model. Similar to previous works, we use the nuclear reaction network as developed in Timmes (1999). It includes a network of 495 isotopes ranging from  $^1\text{H}$  to  $^{91}\text{Tc}$ . The nuclear reaction rates are updated by the values provided in Rauscher & Thielemann (2000). We include the electron screening by Kitamura (2000) and Benvenuto et al. (2015). The formula aims for strong electron screening, and it reduces to the weak electron screening given in Abe (1959). We include the corresponding free energy for the calculation of NSE as described in Seitenzahl et al. (2010). The chemical potential assumes the classical ideal gas form, which is suitable for the density ( $\sim 10^9 \text{ g cm}^{-3}$ ) and temperature ( $10^9 \text{ K}$ ) used here. We have also updated the electron capture rate table by including the rate table from Nabi & Klapdor-Kleingrothaus (1999, 2004). We use this rate table when there is no rate given in the original version of the nuclear reaction network, although we remark that the electron capture and its related weak interaction processes are of less importance owing to the typically lower density than the near-Chandrasekhar-mass explosion model.

**Table 4**  
Model Parameters for the One-dimensional Resolution Study

Model	$\Delta x$	$M$	$M_{\text{He}}$	$t_{\text{burn}}$	$\rho_{\text{max}}$	$T_{\text{max}}$
Test2-fine	7.5	1.1	0.05	1.13	11.1	9.0
Test2	15.0	1.1	0.05	1.16 (2.6)	8.0 (2.8)	8.0 (11.1)
Test2-coarse	30.0	1.1	0.05	1.19 (2.6)	3.8 (5.2)	7.5 (6.3)

**Note.**  $M$  and  $M_{\text{He}}$  are in units of  $M_\odot$ .  $\Delta x$  is grid size in units of km.  $t_{\text{burn}}$  is the time needed for the C-detonation wave to burn  $1 M_\odot$  in units of s.  $\rho_{\text{max}}$  is the maximum central density in the simulation, in units of  $10^8 \text{ g cm}^{-3}$ .  $T_{\text{max}}$  is the maximum central temperature experienced in the simulations in units of  $10^9 \text{ K}$ . The numbers in parentheses stand for the percentage difference between that model and the higher-resolution model.

### 6.1. Dependence on WD Mass

#### 6.1.1. One-bubble Configuration

In Figure 12 we plot  $[X_i/^{56}\text{Fe}]$  for the isotopes from Models 105-100-2-50 (X), 110-100-2-50 (X), 115-100-2-50 (D), and 120-100-2-50 (D). The isotopes are obtained from the nucleosynthesis by the post-processing as described above, but after all short-lived isotopes decayed. In practice, after the nucleosynthesis yield is computed by post-processing, we allow further radioactive decays by computing the network while suppressing thermonuclear reactions. We fixed the period to be  $10^6 \text{ yr}$ . The period is chosen to be long enough to allow certain long-lived isotopes, such as  $^{59}\text{Ni}$ , to completely decay to compute the asymptotic chemical yield. But we also note that there are still some isotopes with even longer half-lives, such as  $^{27}\text{Al}$  and  $^{60}\text{Fe}$ .

These models in this figure have the same configurations by setting the same  $M_{\text{He}}$ , initial He detonation pattern, and metallicity. As a result, the mass of the CO fuel increases when the total mass increases. By increasing the mass, there is a systematic decrease in  $[X_i/^{56}\text{Fe}]$ . This is because when the mass increases, the produced  $^{56}\text{Ni}$  increases as shown in Table 1. The final  $^{56}\text{Fe}$  yield thus increases. For IME, there is a drop from Mg to Ca by a factor of  $\sim O(1)$ . Similar effects are observed in Fe-peak isotopes. This shows that when the mass

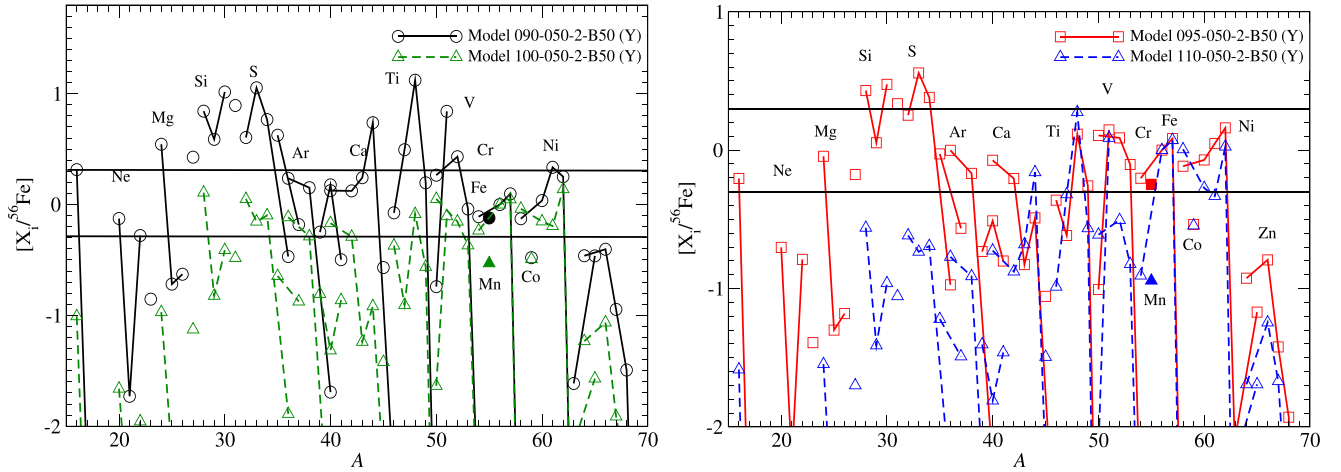


**Figure 13.**  $[X_i/^{56}\text{Fe}]$  fractions for Models 090-050-2-B50 (Y) ( $M = 0.90 M_\odot$ ) and 100-050-2-B50 (Y) ( $M = 1.00 M_\odot$ ) in the left panel and Models 095-050-2-B50 (Y) ( $M = 0.95 M_\odot$ ) and 110-050-2-B50 (Y) ( $M = 1.10 M_\odot$ ) in the right panel. All models assume  $M_{\text{He}} = 0.05 M_\odot$ ,  $Z = 0.02$ , and a belt-shape initial He detonation at 50 km above the CO-envelope interface.

**Table 5**  
Model Parameters for the One-dimensional Resolution Study

Model	$\Delta x$	$M$	$M_{\text{He}}$	$t_{\text{burn}}$	$T_{\text{max}}$	$E_{\text{fin}}$	Second Detonation
Test3-fine	7.5	1.1	0.05	0.49	4.3	$\sim -1.63$	No
Test3	15.0	1.1	0.05	0.58 (18.4)	4.8 (11.6)	$-1.64$ (0.6)	No
Test3-coarse	30.0	1.1	0.05	0.75 (29.3)	5.3 (10.4)	$-1.66$ (1.2)	No

**Note.**  $M$  and  $M_{\text{He}}$  are in units of  $M_\odot$ .  $\Delta x$  is grid size in units of km.  $t_{\text{burn}}$  is the time needed for the C-detonation wave to burn everything in units of s.  $E_{\text{fin}}$  is the final asymptotic energy given by the simulation, in units of  $10^{50}$  erg.  $T_{\text{max}}$  is the maximum central temperature experienced in the simulations in units of  $10^9$  K. “Second Detonation” indicates whether the carbon detonation is triggered throughout the simulation. The numbers in parentheses stand for the percentage difference between that model and the higher-resolution model.

increases, the extra ash contributes to the production of  $^{56}\text{Fe}$ . Therefore, the qualitative features of the mass fraction remain.

Nevertheless, even for a massive progenitor like Model 115-100-2-50 (D), the overproduction of  $^{48}\text{Ti}$  cannot be resolved, as they are mostly produced in the He envelope. Some of the isotopes, such as  $^{51}\text{V}$ ,  $^{52}\text{Cr}$ , and  $^{70}\text{Zn}$ , become comparable to the solar abundance when  $M = 1.15 M_\odot$ . However, compared to the Chandrasekhar-mass SN Ia, none of the isotopes show a drastic boost when  $M$  increases. This can be compared to the Chandrasekhar-mass WD scenario, by increasing the mass from 1.30 to  $1.37 M_\odot$ ; some of the isotopes, such as  $^{54}\text{Cr}$  and  $^{60}\text{Fe}$ , can be drastically enhanced. One reason is that the density related to the sub-Chandrasekhar-mass model is low enough that the electron capture does not play an important role in most parts of the star. The major changes come from the increment of  $^{56}\text{Ni}$ , which systematically lowers all mass fractions of all isotopes.

### 6.1.2. One-ring Configuration

Figure 13 is similar to Figure 12, but for Models 090-050-2-B50 (Y), 095-050-2-B50 (Y), 100-050-2-B50 (Y), and 110-050-2-B50 (Y), respectively. These models correspond to the series of models of the same  $M_{\text{He}}$  but at different masses, each with the same initial He detonation by an He ring. Due to the detonation symmetry that may trigger the second detonation with a lower He mass, the effects of the He incomplete burning products, such as Ti, V, and Cr, become better fit to the solar

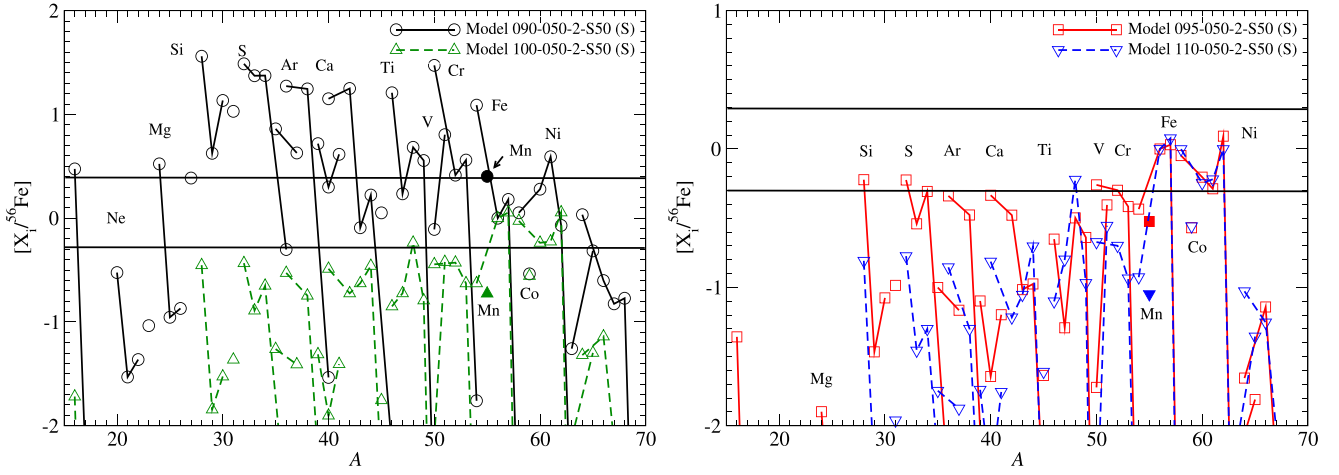
abundance. The qualitative trends for an increasing mass can be observed.

At lower mass, the lower production of  $^{56}\text{Ni}$  causes a strong overproduction of elements like Si and S. Ti and V are overproduced, but this feature is suppressed at Model 090-050-2-B50 (Y). As mass increases, the relative productions of IMEs drop. This includes Si, S, Ar, and Ca. Relative productions of Ti, V, and Cr also decrease when the mass increases, but they remain saturated around the solar values. Fe and Ni are overall insensitive to the mass change.

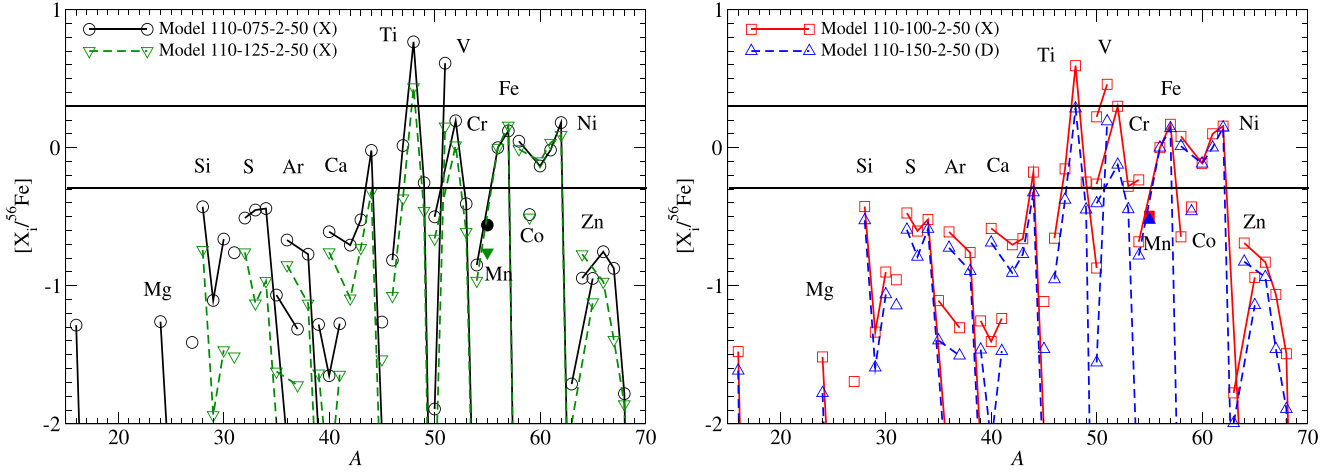
### 6.1.3. Spherical Configuration

Figure 14 is similar to Figure 12, but for Models 090-050-2-S50 (S), 095-050-2-S50 (S), 100-050-2-S50 (S), and 110-050-2-S50 (S), respectively, using the spherical He detonation as the initial trigger. Again, the higher He detonation symmetry allows triggering the second detonation at a lower He envelope. The overproduction of intermediate  $\alpha$ -chain burning production is less severe for the models with a normal amount of  $^{56}\text{Ni}$  ( $\sim 0.6 M_\odot$ ). Due to the spherical symmetry, the second detonation all starts at the core for all models, so that the variations of elements become more regular.

The IMEs Si, S, Ar, and Ca show a flat distribution and decrease with an increasing mass. The overproductions of  $^{50}\text{Ti}$ ,  $^{51}\text{V}$ , and  $^{52}\text{Cr}$ , as the major products in He detonation before reaching  $^{56}\text{Ni}$ , are largely suppressed once the mass reaches above  $0.95 M_\odot$ . The isotopes of Fe remain nonsensitive to the variation of mass except for  $^{54}\text{Fe}$ . A systematic drop of  $^{55}\text{Mn}$



**Figure 14.**  $[X_i/^{56}\text{Fe}]$  for Models 090-050-2-S50 (S) ( $M = 0.90 M_\odot$ ) and 100-050-2-S50 (S) ( $M = 1.00 M_\odot$ ) in the left panel and Models 095-050-2-S50 (S) ( $M = 0.95 M_\odot$ ) and 110-050-2-S50 (S) ( $M = 1.10 M_\odot$ ) in the right panel. All models assume  $M_{\text{He}} = 0.05 M_\odot$ ,  $Z = 0.02$ , and a spherical initial He detonation at 50 km above the CO-envelope interface.



**Figure 15.**  $[X_i/^{56}\text{Fe}]$  for models comparing the effects of He envelope mass, including Models 110-075-2-50 (X) ( $M_{\text{He}} = 0.075 M_\odot$ ) and 110-125-2-50 (X) ( $M_{\text{He}} = 0.125 M_\odot$ ) in the left panel and Models 110-100-2-50 (X) ( $M_{\text{He}} = 0.100 M_\odot$ ) and 110-150-2-50 (D) ( $M_{\text{He}} = 0.150 M_\odot$ ) in the right panel. All models assume  $M = 1.10 M_\odot$ ,  $Z = 0.02$ , and a bubble-shape initial He detonation at 50 km above the CO-envelope interface.

can also be seen, showing that the amount of  $^{55}\text{Mn}$  is not increased significantly when the mass increases.

## 6.2. Dependence on He Envelope Mass

### 6.2.1. One-bubble Configuration

Figure 15 is similar to Figure 12, but for Models 110-075-2-50 (X), 110-100-2-50 (X), 110-125-2-50 (X), and 110-150-2-50 (D). These models also have the same configurations except for the He envelope mass. Notice that among these models, Model 110-150-2-50 (D) has a different detonation mechanism, as it has a “D”-type detonation instead of an “X”-type detonation. By increasing  $M_{\text{He}}$ , the mass fractions of IMEs reduce. However, by comparing Models 110-125-2-50 (X) and 110-150-2-50 (D), the IME mass fractions increase. This is because the “Y”-type detonation allows an earlier detonation, which ensures that the low-density matter is well detonated before it expands and the density becomes too low for nuclear reaction. For Fe-peak elements, clear trends can be seen in elements like Ti, Cr, and V. Again, a decreasing trend is

observed when  $M_{\text{He}}$  increases, but there is not much difference in Fe and Ni.

### 6.2.2. One-ring Configuration

Figure 16 is similar to Figure 15, but for Models 100-050-2-B50 (Y), 100-100-2-B50 (Y), 110-050-2-B50 (Y), and 110-100-2-B50 (Y), where all models share the same initial masses  $M = 1.00$  and  $1.10 M_\odot$  and He detonation configuration. Different He envelope masses are used. We remind that Model 110-050-2-B50 (Y) is the benchmark model, and we choose a progenitor mass for comparison to extract the effects of  $M_{\text{He}}$  at different masses.

For  $M = 1.10 M_\odot$ , the chemical abundances do not change strongly with  $M_{\text{He}}$ . This is because the overall production is dominated by  $^{56}\text{Ni}$ . A small suppression of IMEs for  $^{28}\text{Si}$ ,  $^{32}\text{S}$ , and  $^{36}\text{Ar}$  can be observed. Almost no change can be found for Fe-peak elements from Ti to Ni. On the other hand, for  $M = 1.00 M_\odot$ , the chemical abundances scale strongly with  $M_{\text{He}}$ . Besides the more obvious drop in the IMEs, there is a



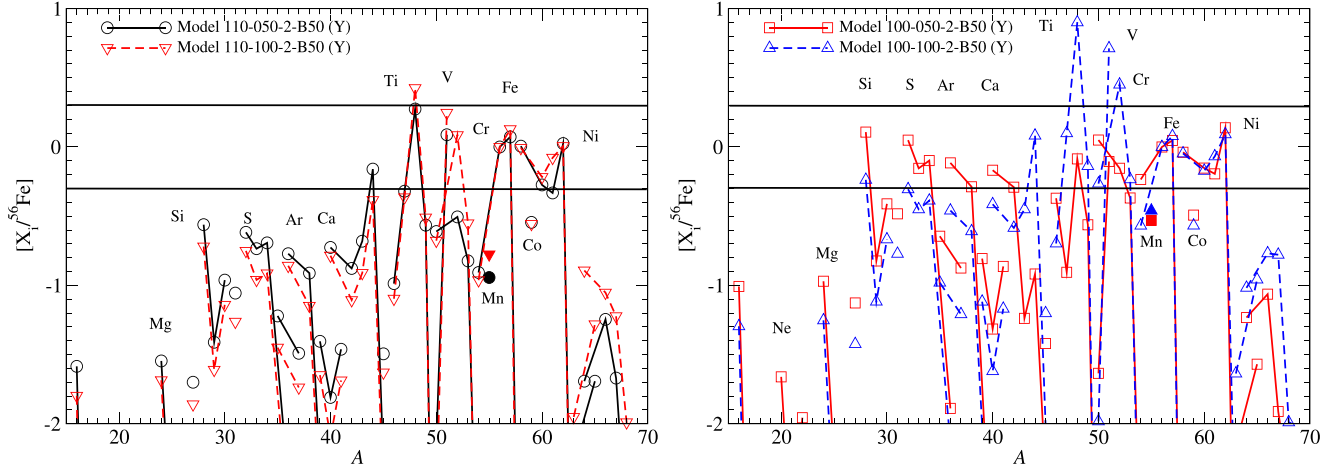


**Figure 16.** Similar to Figure 15, but for Models 100-050-2-B50 (Y) ( $M = 1.00 M_{\odot}$ ) and 110-050-2-B50 (Y) ( $M = 1.10 M_{\odot}$ ) in the left panel and Models 100-100-2-B50 (Y) ( $M = 1.00 M_{\odot}$ ) and 110-100-2-B50 (Y) ( $M = 1.10 M_{\odot}$ ) in the right panel. All models assume  $M_{\text{He}} = 0.05$  (0.10)  $M_{\odot}$  in the left (right) panel,  $Z = 0.02$ , and a belt-shape initial He detonation at 50 km above the CO-envelope interface.

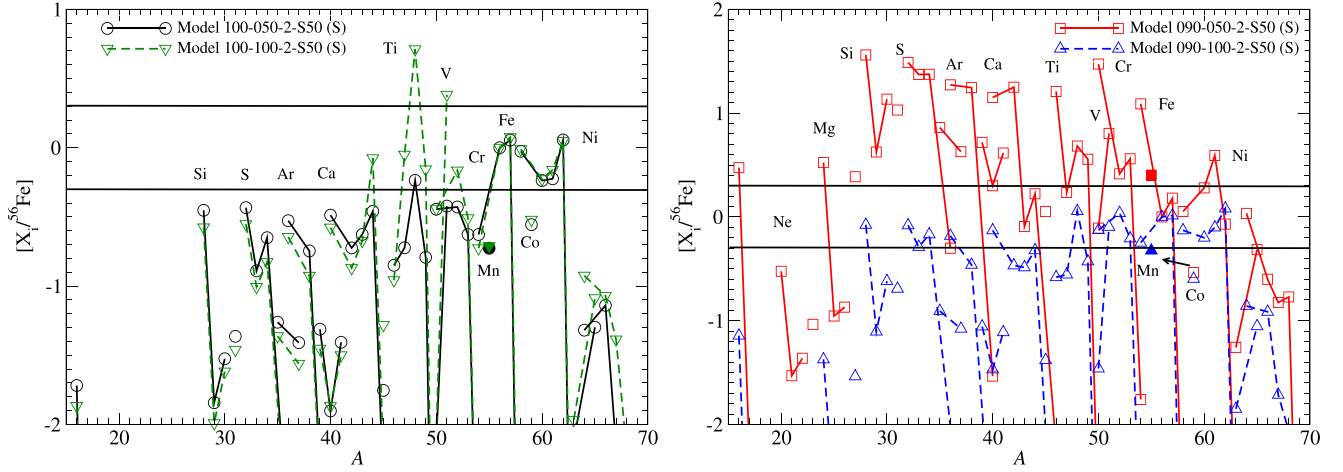


**Figure 17.** Similar to Figure 15, but for Models 100-050-2-S50 (S) ( $M = 1.00 M_{\odot}$ ) and 110-050-2-S50 (S) ( $M = 1.10 M_{\odot}$ ) in the left panel and Models 100-100-2-S50 (S) ( $M = 1.00 M_{\odot}$ ) and 110-100-2-S50 (S) ( $M = 1.10 M_{\odot}$ ) in the right panel. All models assume  $M_{\text{He}} = 0.05$  (0.10)  $M_{\odot}$  in the left (right) panel,  $Z = 0.02$ , and a spherical initial He detonation at 50 km above the CO-envelope interface.

huge jump in  $^{48}\text{Ti}$ ,  $^{51}\text{V}$ , and  $^{52}\text{Cr}$  when  $M_{\text{He}}$  increases. Again, Fe-peak elements like Fe, Mn, and Ni are less changed by  $M_{\text{He}}$ .

### 6.2.3. Spherical Configuration

Figure 17 is similar to Figure 15, but for the Models 090-050-2-S50 (S), 090-100-2-S50 (S), 100-050-2-S50 (S), and 100-100-2-S50 (S). The models consist of initial masses of 1.00 and 1.10  $M_{\odot}$ . All models assume a spherical He detonation as the initial trigger. Again, we remind that Model 100-050-2-S50 is the benchmark model of this work.

For the spherical model, due to its stronger explosion, a lower-mass model is used for the benchmark model. So compared to the one-ring structure, the effects of the He envelope are larger. Besides a more prominent decrease in IMEs, the  $\alpha$ -chain products including  $^{48}\text{Ti}$ ,  $^{52}\text{Cr}$ , and  $^{51}\text{V}$  are vastly increased for a more massive He envelope. No significant change is observed for Fe, Mn, and Ni. The effects are more significant for the lower-mass cases owing to a smaller  $^{56}\text{Ni}$  mass. A flat distribution in  $^{28}\text{Si}$ ,  $^{32}\text{S}$ ,  $^{36}\text{Ar}$ ,  $^{40}\text{Ca}$ ,  $^{42}\text{Ca}$ ,  $^{44}\text{Ti}$ , and  $^{48}\text{Cr}$  can be seen. The  $^{55}\text{Mn}$  is even overproduced because of the suppressed  $^{56}\text{Ni}$  and hence  $^{56}\text{Fe}$ . A

higher  $M_{\text{He}}$  results in a global suppression of this relative production rate.

## 6.3. Dependence on Metallicity

### 6.3.1. One-bubble Configuration

In Figure 18 we plot  $[X_i/^{56}\text{Fe}]$  of stable isotopes after all short-lived radioactive isotopes have decayed for Models 110-100-0-50 (X), 110-100-2-50 (X), 110-100-6-50 (X), and 110-100-10-50 (X). Similar to Chandrasekhar-mass SNe Ia (Leung & Nomoto 2018), metallicity is important to the production of isotopes with a neutron-to-proton ratio close to unity. Also, the presence of  $^{22}\text{Ne}$  slightly lowers the energy release of C detonation. We can observe a boost of IMEs including  $^{30}\text{Si}$ ,  $^{34}\text{S}$ ,  $^{38}\text{Ar}$ , and  $^{42}\text{Ca}$ . The boost factors can be as large as beyond two orders of magnitude when the metallicity increases from 0 to 5  $Z_{\odot}$ . For Fe-peak elements, we also observe a boost in the production of  $^{46}\text{Ti}$ ,  $^{50}\text{Cr}$ ,  $^{54}\text{Fe}$ ,  $^{55}\text{Mn}$ , and  $^{58}\text{Ni}$ . The boost can range from 10 to 100 when contrasting Models 110-100-0-50 (X) and 110-100-10-50 (X). In Tables 6 (7), 8 (9) and 10 (11) we tabulate the masses of the stable (radioactive) isotopes in

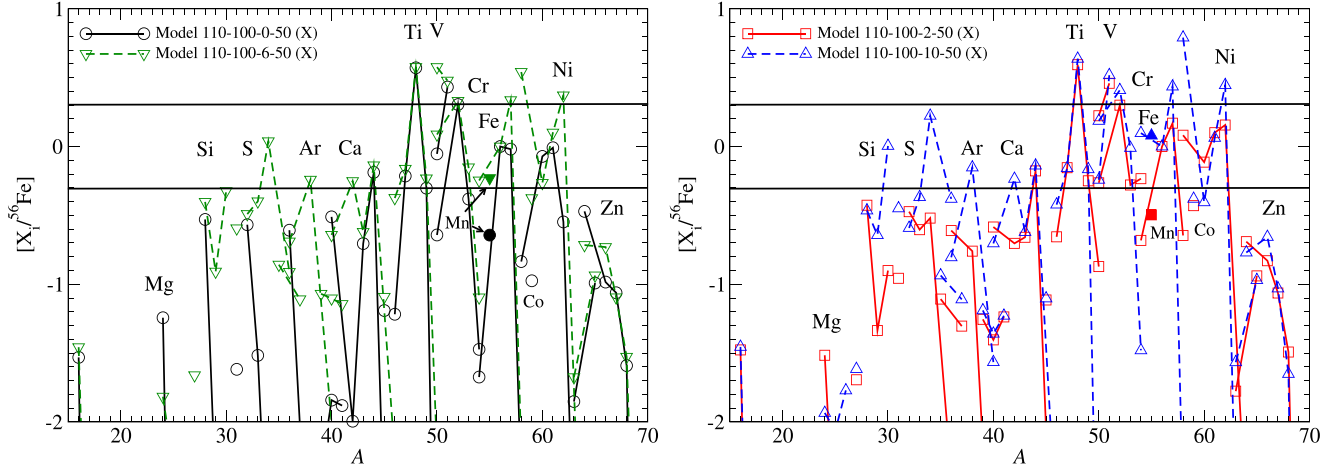


**Figure 18.** Similar to Figure 12, but for Models 110-100-0-50 (X) ( $Z = 0$ ) and 110-100-6-50 (X) ( $Z = 0.06$ ) in the left panel and Models 110-100-2-50 (X) ( $Z = 0.02$ ) and 110-100-10-50 (X) ( $Z = 0.10$ ) in the right panel. All models assume  $M = 1.10 M_{\odot}$ ,  $M_{\text{He}} = 0.10 M_{\odot}$ , and a bubble-shape initial He detonation at 50 km above the CO-envelope interface.

different metallicities for the benchmark models based on Models 110-100-2-50 (X), 100-050-2-B50 (Y), and 110-050-2-S50 (S), respectively. By comparing models with the same configuration but different metallicities, it can be seen that when metallicity increases, IMEs with a high neutron ratio are boosted sharply. For example, we observe a clear increasing trend for  $^{29-30}\text{Si}$ ,  $^{34,36}\text{S}$ ,  $^{37}\text{Cl}$ ,  $^{38}\text{Ar}$ ,  $^{40}\text{K}$ , and so on. The jump can be as high as four orders of magnitude from zero metallicity to  $5 Z_{\odot}$ . For Fe-peak elements, we have  $^{46}\text{Ti}$ ,  $^{50}\text{V}$ ,  $^{50}\text{Cr}$ ,  $^{54}\text{Fe}$ , and  $^{58}\text{Ni}$  as the representative isotopes. The results here are very similar to those in Chandrasekhar-mass WDs.

### 6.3.2. One-ring Configuration

Figure 19 is similar to Figure 18, but for Models 110-050-0-B50 (Y), 110-050-2-B50 (Y), 110-050-6-B50 (Y), and 110-050-10-B50 (Y). These models focus on the effects of metallicity for the same progenitor mass  $M = 1.1 M_{\odot}$ , He mass at  $0.05 M_{\odot}$ , and the same He detonation trigger.

The general trends of isotopes on metallicity are similar to the one-bubble case. There is no significant change for the  $\alpha$ -chain isotopes such as  $^{28}\text{Si}$ ,  $^{32}\text{S}$ ,  $^{36}\text{Ar}$ , and  $^{44}\text{Ca}$ . But the slightly low- $Y_e$  isotopes, such as  $^{30}\text{Si}$  and  $^{34}\text{S}$ , are strongly enhanced at high metallicity. There are smaller changes for the Fe-peak elements except for  $^{52}\text{Cr}$ ,  $^{54}\text{Fe}$ ,  $^{55}\text{Mn}$ , and  $^{58}\text{Ni}$ . Minor increases can be observed for isotopes like  $^{48}\text{Ti}$  and  $^{51}\text{V}$ .

### 6.3.3. Spherical Configuration

Figure 20 is similar to Figure 18, but for Models 110-050-0-S50 (S), 110-050-2-S50 (S), 110-050-6-S50 (S), and 110-050-10-S50 (S). Again, the models here share the same initial progenitor mass at  $1.10 M_{\odot}$ , He mass at  $0.05 M_{\odot}$ , and an initial spherical He detonation. The overall pattern remains compatible with the single one-bubble case.

The metallicity plays an important role for the slightly low- $Y_e$  isotopes (defined by the neutron number  $N$  comparable to but not larger than atomic number  $Z$ ), including  $^{30}\text{Si}$ ,  $^{34}\text{S}$ ,  $^{38}\text{S}$ , and  $^{42}\text{Ca}$  for the IMEs and  $^{51}\text{V}$ ,  $^{52}\text{Cr}$ ,  $^{55}\text{Mn}$ ,  $^{54}\text{Fe}$ , and  $^{58}\text{Ni}$  for Fe-peak isotopes. The variations of isotopes against metallicity are similar to the previous two cases. This shows that the metallicity dependence is not sensitive to the explosion energetics.

### 6.4. Dependence on He Detonation Pattern

Here we analyze the final chemical abundance for different types of detonations. In Figure 21 we plot  $[X_i]/^{56}\text{Fe}$  for Models 110-100-2-50 (X), 110-100-2-B50 (Y), 110-100-2-2R50 (D), and 110-100-2-S50 (S). They represent the typical detonation of Type “D,” “X,” “Y,” and “S,” respectively. All four models have  $^{56}\text{Ni}$  closest to  $0.6 M_{\odot}$  among all models we have. We observe that in general “S” type is the strongest, as it has more isotopes with abundances closer to solar values. “X” and “Y” types are the intermediate ones, and “D” type is the weakest among the four models. The difference for IMEs can be as large as a factor of  $\sim O(1)$ . For Fe-peak elements, differences can be found from Ti to Cr. The “Y”-type model tends to produce less  $^{47-50}\text{Ti}$ ,  $^{50-51}\text{V}$ , and  $^{64-70}\text{Zn}$ . The major difference between “Y” type and other detonation types is that there is no shock-convergence-induced heating along the  $r$ -axis. This shows that  $^{48}\text{Ti}$  is a sensitive indicator of how the He detonation propagates along the surface of the WD. Similar to previous cases, Fe and Ni are less sensitive to the detonation mechanism owing to the difference in production site.

### 6.5. Differences from Spherical Detonation

One theoretical uncertainty in the He detonation is that it is unclear whether the pre-explosion fluid motion is strong enough to alter the first detonation site. In the case with a strong fluid motion background, heat generated can be distributed by the eddy motion or be further enhanced by the local turbulent motion. This breaks the initial symmetry and creates some detonation bubbles. On the other hand, in the quiescent star, the whole He layer can simultaneously burn and reach the explosive temperature together. Thus, the initial detonation can preserve the symmetry. To derive constraints on the initial detonation profile, we examine the scaled mass fraction again in Figure 22 for both the spherical and aspherical detonation models. Both models produce a very similar distribution for Fe and Ni since they are chosen to produce  $\sim 0.6 M_{\odot}$ . For lighter Fe-peak elements, differences appear. The aspherical model produces more Ti, V, and Cr than the spherical one for at least one order of magnitude. In particular, the  $^{48}\text{Ti}$ ,  $^{50-51}\text{V}$ , and  $^{52}\text{Cr}$  are  $\sim 2$ – $5$  times higher than solar values. This suggests that observations of the non-aspherical

**Table 6**  
Nucleosynthesis Yields for the Stable Isotopes of the Benchmark Model at Different Metallicities

Isotope	$Z = 0$	$Z = 0.1 Z_{\odot}$	$Z = 0.5 Z_{\odot}$	$Z = Z_{\odot}$	$Z = 2 Z_{\odot}$	$Z = 3 Z_{\odot}$	$Z = 5 Z_{\odot}$
$^{12}\text{C}$	$3.39 \times 10^{-3}$	$3.38 \times 10^{-3}$	$3.38 \times 10^{-3}$	$3.35 \times 10^{-3}$	$3.29 \times 10^{-3}$	$2.62 \times 10^{-3}$	$2.20 \times 10^{-3}$
$^{13}\text{C}$	$3.33 \times 10^{-10}$	$1.22 \times 10^{-10}$	$3.41 \times 10^{-10}$	$1.25 \times 10^{-9}$	$4.59 \times 10^{-9}$	$2.9 \times 10^{-8}$	$1.20 \times 10^{-8}$
$^{14}\text{N}$	$1.16 \times 10^{-8}$	$4.53 \times 10^{-9}$	$1.37 \times 10^{-8}$	$3.80 \times 10^{-8}$	$9.63 \times 10^{-8}$	$6.40 \times 10^{-7}$	$9.43 \times 10^{-8}$
$^{15}\text{N}$	$2.44 \times 10^{-6}$	$3.97 \times 10^{-8}$	$3.2 \times 10^{-9}$	$1.8 \times 10^{-9}$	$4.42 \times 10^{-10}$	$1.86 \times 10^{-9}$	$6.88 \times 10^{-10}$
$^{16}\text{O}$	$1.14 \times 10^{-1}$	$1.14 \times 10^{-1}$	$1.16 \times 10^{-1}$	$1.17 \times 10^{-1}$	$1.19 \times 10^{-1}$	$1.12 \times 10^{-1}$	$1.4 \times 10^{-1}$
$^{17}\text{O}$	$1.86 \times 10^{-10}$	$5.92 \times 10^{-10}$	$5.31 \times 10^{-9}$	$2.8 \times 10^{-8}$	$6.32 \times 10^{-8}$	$1.44 \times 10^{-7}$	$5.44 \times 10^{-8}$
$^{18}\text{O}$	$7.64 \times 10^{-12}$	$2.4 \times 10^{-11}$	$1.37 \times 10^{-10}$	$3.4 \times 10^{-10}$	$4.87 \times 10^{-10}$	$2.67 \times 10^{-9}$	$1.5 \times 10^{-9}$
$^{19}\text{F}$	$3.67 \times 10^{-10}$	$5.26 \times 10^{-11}$	$1.78 \times 10^{-11}$	$3.28 \times 10^{-11}$	$1.5 \times 10^{-10}$	$3.31 \times 10^{-10}$	$3.46 \times 10^{-10}$
$^{20}\text{Ne}$	$3.98 \times 10^{-3}$	$3.96 \times 10^{-3}$	$4.4 \times 10^{-3}$	$4.0 \times 10^{-3}$	$3.86 \times 10^{-3}$	$3.42 \times 10^{-3}$	$3.16 \times 10^{-3}$
$^{21}\text{Ne}$	$1.16 \times 10^{-8}$	$1.5 \times 10^{-8}$	$6.10 \times 10^{-8}$	$2.17 \times 10^{-7}$	$7.58 \times 10^{-7}$	$2.20 \times 10^{-6}$	$3.85 \times 10^{-6}$
$^{22}\text{Ne}$	$1.16 \times 10^{-8}$	$9.45 \times 10^{-6}$	$4.72 \times 10^{-5}$	$9.45 \times 10^{-5}$	$1.89 \times 10^{-4}$	$1.82 \times 10^{-4}$	$3.1 \times 10^{-4}$
$^{23}\text{Na}$	$7.18 \times 10^{-6}$	$7.71 \times 10^{-6}$	$1.1 \times 10^{-5}$	$1.47 \times 10^{-5}$	$2.46 \times 10^{-5}$	$4.4 \times 10^{-5}$	$6.5 \times 10^{-5}$
$^{24}\text{Mg}$	$1.70 \times 10^{-2}$	$1.60 \times 10^{-2}$	$1.11 \times 10^{-2}$	$8.26 \times 10^{-3}$	$5.46 \times 10^{-3}$	$3.77 \times 10^{-3}$	$2.66 \times 10^{-3}$
$^{25}\text{Mg}$	$2.15 \times 10^{-7}$	$3.49 \times 10^{-6}$	$1.53 \times 10^{-5}$	$3.89 \times 10^{-5}$	$9.28 \times 10^{-5}$	$1.50 \times 10^{-4}$	$2.61 \times 10^{-4}$
$^{26}\text{Mg}$	$2.36 \times 10^{-6}$	$7.52 \times 10^{-6}$	$2.80 \times 10^{-5}$	$5.60 \times 10^{-5}$	$1.27 \times 10^{-4}$	$2.47 \times 10^{-4}$	$5.85 \times 10^{-4}$
$^{26}\text{Al}$	$2.86 \times 10^{-29}$	$2.86 \times 10^{-29}$	$2.86 \times 10^{-29}$	$2.86 \times 10^{-29}$	$2.86 \times 10^{-29}$	$2.86 \times 10^{-29}$	$1.0 \times 10^{-10}$
$^{27}\text{Al}$	$7.37 \times 10^{-5}$	$2.6 \times 10^{-4}$	$5.27 \times 10^{-4}$	$6.50 \times 10^{-4}$	$6.97 \times 10^{-4}$	$6.39 \times 10^{-4}$	$6.56 \times 10^{-4}$
$^{28}\text{Si}$	$1.17 \times 10^{-1}$	$1.22 \times 10^{-1}$	$1.36 \times 10^{-1}$	$1.35 \times 10^{-1}$	$1.32 \times 10^{-1}$	$1.30 \times 10^{-1}$	$1.4 \times 10^{-1}$
$^{29}\text{Si}$	$6.15 \times 10^{-5}$	$3.20 \times 10^{-4}$	$5.66 \times 10^{-4}$	$8.76 \times 10^{-4}$	$1.57 \times 10^{-3}$	$2.13 \times 10^{-3}$	$3.64 \times 10^{-3}$
$^{30}\text{Si}$	$3.81 \times 10^{-5}$	$6.74 \times 10^{-5}$	$7.2 \times 10^{-4}$	$1.62 \times 10^{-3}$	$3.62 \times 10^{-3}$	$5.59 \times 10^{-3}$	$1.10 \times 10^{-2}$
$^{31}\text{P}$	$9.57 \times 10^{-5}$	$5.89 \times 10^{-5}$	$2.33 \times 10^{-4}$	$3.97 \times 10^{-4}$	$6.62 \times 10^{-4}$	$8.36 \times 10^{-4}$	$1.8 \times 10^{-3}$
$^{32}\text{S}$	$5.40 \times 10^{-2}$	$5.28 \times 10^{-2}$	$6.14 \times 10^{-2}$	$6.8 \times 10^{-2}$	$5.69 \times 10^{-2}$	$5.33 \times 10^{-2}$	$3.91 \times 10^{-2}$
$^{33}\text{S}$	$5.1 \times 10^{-5}$	$1.32 \times 10^{-4}$	$2.73 \times 10^{-4}$	$3.72 \times 10^{-4}$	$4.95 \times 10^{-4}$	$5.45 \times 10^{-4}$	$5.41 \times 10^{-4}$
$^{34}\text{S}$	$6.96 \times 10^{-6}$	$1.26 \times 10^{-4}$	$1.19 \times 10^{-3}$	$2.62 \times 10^{-3}$	$5.68 \times 10^{-3}$	$8.65 \times 10^{-3}$	$1.22 \times 10^{-2}$
$^{36}\text{S}$	$1.19 \times 10^{-9}$	$2.76 \times 10^{-9}$	$3.86 \times 10^{-8}$	$1.77 \times 10^{-7}$	$1.53 \times 10^{-6}$	$4.80 \times 10^{-6}$	$1.51 \times 10^{-5}$
$^{35}\text{Cl}$	$1.2 \times 10^{-5}$	$2.17 \times 10^{-5}$	$8.55 \times 10^{-5}$	$1.51 \times 10^{-4}$	$2.41 \times 10^{-4}$	$2.45 \times 10^{-4}$	$1.90 \times 10^{-4}$
$^{37}\text{Cl}$	$5.1 \times 10^{-6}$	$1.10 \times 10^{-5}$	$2.39 \times 10^{-5}$	$3.26 \times 10^{-5}$	$4.31 \times 10^{-5}$	$4.65 \times 10^{-5}$	$4.30 \times 10^{-5}$
$^{36}\text{Ar}$	$1.8 \times 10^{-2}$	$9.79 \times 10^{-3}$	$1.4 \times 10^{-2}$	$9.73 \times 10^{-3}$	$8.24 \times 10^{-3}$	$7.39 \times 10^{-3}$	$5.25 \times 10^{-3}$
$^{38}\text{Ar}$	$2.93 \times 10^{-6}$	$6.44 \times 10^{-5}$	$6.1 \times 10^{-4}$	$1.32 \times 10^{-3}$	$2.76 \times 10^{-3}$	$3.98 \times 10^{-3}$	$4.53 \times 10^{-3}$
$^{40}\text{Ar}$	$2.32 \times 10^{-10}$	$2.41 \times 10^{-10}$	$8.66 \times 10^{-10}$	$3.35 \times 10^{-9}$	$3.53 \times 10^{-8}$	$1.14 \times 10^{-7}$	$2.94 \times 10^{-7}$
$^{39}\text{K}$	$9.47 \times 10^{-6}$	$2.30 \times 10^{-5}$	$7.10 \times 10^{-5}$	$1.7 \times 10^{-4}$	$1.45 \times 10^{-4}$	$1.49 \times 10^{-4}$	$1.5 \times 10^{-4}$
$^{40}\text{K}$	$4.96 \times 10^{-8}$	$5.13 \times 10^{-8}$	$8.32 \times 10^{-8}$	$1.23 \times 10^{-7}$	$2.25 \times 10^{-7}$	$2.24 \times 10^{-7}$	$1.15 \times 10^{-7}$
$^{41}\text{K}$	$2.12 \times 10^{-6}$	$3.87 \times 10^{-6}$	$6.60 \times 10^{-6}$	$8.47 \times 10^{-6}$	$9.95 \times 10^{-6}$	$9.58 \times 10^{-6}$	$7.29 \times 10^{-6}$
$^{40}\text{Ca}$	$1.11 \times 10^{-2}$	$9.73 \times 10^{-3}$	$9.38 \times 10^{-3}$	$8.49 \times 10^{-3}$	$7.14 \times 10^{-3}$	$6.79 \times 10^{-3}$	$5.45 \times 10^{-3}$
$^{42}\text{Ca}$	$2.55 \times 10^{-6}$	$4.15 \times 10^{-6}$	$2.13 \times 10^{-5}$	$4.53 \times 10^{-5}$	$8.90 \times 10^{-5}$	$1.17 \times 10^{-4}$	$1.12 \times 10^{-4}$
$^{43}\text{Ca}$	$1.29 \times 10^{-5}$	$1.30 \times 10^{-5}$	$1.32 \times 10^{-5}$	$1.30 \times 10^{-5}$	$1.31 \times 10^{-5}$	$1.30 \times 10^{-5}$	$1.20 \times 10^{-5}$
$^{44}\text{Ca}$	$5.52 \times 10^{-4}$	$5.49 \times 10^{-4}$	$5.15 \times 10^{-4}$	$5.14 \times 10^{-4}$	$5.13 \times 10^{-4}$	$5.13 \times 10^{-4}$	$4.74 \times 10^{-4}$
$^{46}\text{Ca}$	$6.40 \times 10^{-12}$	$6.41 \times 10^{-12}$	$2.80 \times 10^{-11}$	$1.78 \times 10^{-10}$	$9.73 \times 10^{-10}$	$7.95 \times 10^{-9}$	$2.18 \times 10^{-9}$
$^{48}\text{Ca}$	$1.93 \times 10^{-15}$	$1.93 \times 10^{-15}$	$1.53 \times 10^{-14}$	$9.31 \times 10^{-12}$	$7.31 \times 10^{-14}$	$1.36 \times 10^{-10}$	$2.20 \times 10^{-12}$
$^{45}\text{Sc}$	$1.54 \times 10^{-6}$	$1.61 \times 10^{-6}$	$1.60 \times 10^{-6}$	$1.67 \times 10^{-6}$	$1.72 \times 10^{-6}$	$1.61 \times 10^{-6}$	$1.45 \times 10^{-6}$
$^{46}\text{Ti}$	$8.89 \times 10^{-6}$	$9.57 \times 10^{-6}$	$1.96 \times 10^{-5}$	$2.94 \times 10^{-5}$	$4.46 \times 10^{-5}$	$5.13 \times 10^{-5}$	$4.25 \times 10^{-5}$
$^{47}\text{Ti}$	$8.26 \times 10^{-5}$	$8.28 \times 10^{-5}$	$8.57 \times 10^{-5}$	$8.61 \times 10^{-5}$	$8.63 \times 10^{-5}$	$7.71 \times 10^{-5}$	$7.21 \times 10^{-5}$
$^{48}\text{Ti}$	$5.10 \times 10^{-3}$	$5.7 \times 10^{-3}$	$4.89 \times 10^{-3}$	$4.87 \times 10^{-3}$	$4.85 \times 10^{-3}$	$4.27 \times 10^{-3}$	$4.54 \times 10^{-3}$
$^{49}\text{Ti}$	$5.11 \times 10^{-5}$	$5.50 \times 10^{-5}$	$5.11 \times 10^{-5}$	$5.24 \times 10^{-5}$	$5.30 \times 10^{-5}$	$4.97 \times 10^{-5}$	$5.37 \times 10^{-5}$
$^{50}\text{Ti}$	$2.74 \times 10^{-9}$	$2.74 \times 10^{-9}$	$8.21 \times 10^{-9}$	$1.22 \times 10^{-5}$	$1.8 \times 10^{-8}$	$5.2 \times 10^{-7}$	$9.39 \times 10^{-9}$
$^{50}\text{V}$	$4.91 \times 10^{-7}$	$4.91 \times 10^{-7}$	$8.36 \times 10^{-7}$	$8.42 \times 10^{-7}$	$8.43 \times 10^{-7}$	$1.73 \times 10^{-6}$	$2.43 \times 10^{-7}$
$^{51}\text{V}$	$6.10 \times 10^{-4}$	$6.12 \times 10^{-4}$	$5.77 \times 10^{-4}$	$5.89 \times 10^{-4}$	$5.93 \times 10^{-4}$	$5.62 \times 10^{-4}$	$5.70 \times 10^{-4}$
$^{50}\text{Cr}$	$1.0 \times 10^{-4}$	$1.7 \times 10^{-4}$	$1.50 \times 10^{-4}$	$2.18 \times 10^{-4}$	$3.50 \times 10^{-4}$	$4.46 \times 10^{-4}$	$5.18 \times 10^{-4}$
$^{52}\text{Cr}$	$1.78 \times 10^{-2}$	$1.76 \times 10^{-2}$	$1.59 \times 10^{-2}$	$1.60 \times 10^{-2}$	$1.56 \times 10^{-2}$	$1.57 \times 10^{-2}$	$1.73 \times 10^{-2}$
$^{53}\text{Cr}$	$4.25 \times 10^{-4}$	$4.74 \times 10^{-4}$	$4.39 \times 10^{-4}$	$4.87 \times 10^{-4}$	$5.20 \times 10^{-4}$	$5.96 \times 10^{-4}$	$7.64 \times 10^{-4}$
$^{54}\text{Cr}$	$8.73 \times 10^{-6}$	$8.73 \times 10^{-6}$	$1.28 \times 10^{-5}$	$1.37 \times 10^{-4}$	$1.30 \times 10^{-5}$	$1.72 \times 10^{-5}$	$6.57 \times 10^{-6}$
$^{55}\text{Mn}$	$1.79 \times 10^{-3}$	$1.95 \times 10^{-3}$	$1.89 \times 10^{-3}$	$2.28 \times 10^{-3}$	$2.60 \times 10^{-3}$	$3.85 \times 10^{-3}$	$7.26 \times 10^{-3}$
$^{54}\text{Fe}$	$8.76 \times 10^{-4}$	$1.36 \times 10^{-3}$	$3.59 \times 10^{-3}$	$7.80 \times 10^{-3}$	$1.23 \times 10^{-2}$	$1.94 \times 10^{-2}$	$3.96 \times 10^{-2}$
$^{56}\text{Fe}$	$6.73 \times 10^{-1}$	$6.69 \times 10^{-1}$	$6.34 \times 10^{-1}$	$6.10 \times 10^{-1}$	$5.83 \times 10^{-1}$	$5.57 \times 10^{-1}$	$5.15 \times 10^{-1}$
$^{57}\text{Fe}$	$1.51 \times 10^{-2}$	$1.60 \times 10^{-2}$	$1.83 \times 10^{-2}$	$2.12 \times 10^{-2}$	$2.52 \times 10^{-2}$	$2.84 \times 10^{-2}$	$3.30 \times 10^{-2}$
$^{58}\text{Fe}$	$6.90 \times 10^{-6}$	$6.90 \times 10^{-6}$	$9.56 \times 10^{-6}$	$4.39 \times 10^{-4}$	$9.61 \times 10^{-6}$	$1.12 \times 10^{-5}$	$3.94 \times 10^{-6}$
$^{60}\text{Fe}$	$1.6 \times 10^{-13}$	$1.1 \times 10^{-13}$	$5.65 \times 10^{-13}$	$1.34 \times 10^{-9}$	$5.63 \times 10^{-13}$	$4.99 \times 10^{-10}$	$1.88 \times 10^{-14}$
$^{59}\text{Co}$	$2.25 \times 10^{-4}$	$2.87 \times 10^{-4}$	$5.38 \times 10^{-4}$	$7.19 \times 10^{-4}$	$7.79 \times 10^{-4}$	$7.42 \times 10^{-4}$	$6.80 \times 10^{-4}$
$^{58}\text{Ni}$	$4.35 \times 10^{-3}$	$5.59 \times 10^{-3}$	$1.56 \times 10^{-2}$	$3.26 \times 10^{-2}$	$5.80 \times 10^{-2}$	$8.56 \times 10^{-2}$	$1.40 \times 10^{-1}$
$^{60}\text{Ni}$	$1.0 \times 10^{-2}$	$1.2 \times 10^{-2}$	$9.8 \times 10^{-3}$	$8.28 \times 10^{-3}$	$6.37 \times 10^{-3}$	$5.34 \times 10^{-3}$	$3.57 \times 10^{-3}$
$^{61}\text{Ni}$	$5.14 \times 10^{-4}$	$5.26 \times 10^{-4}$	$5.85 \times 10^{-4}$	$5.99 \times 10^{-4}$	$5.98 \times 10^{-4}$	$5.47 \times 10^{-4}$	$4.63 \times 10^{-4}$
$^{62}\text{Ni}$	$4.81 \times 10^{-4}$	$6.51 \times 10^{-4}$	$1.33 \times 10^{-3}$	$2.20 \times 10^{-3}$	$2.92 \times 10^{-3}$	$3.30 \times 10^{-3}$	$3.63 \times 10^{-3}$
$^{64}\text{Ni}$	$1.43 \times 10^{-9}$	$1.44 \times 10^{-9}$	$3.64 \times 10^{-9}$	$6.96 \times 10^{-7}$	$3.55 \times 10^{-9}$	$4.69 \times 10^{-8}$	$3.77 \times 10^{-10}$
$^{63}\text{Cu}$	$5.19 \times 10^{-6}$	$6.28 \times 10^{-6}$	$4.98 \times 10^{-6}$	$5.59 \times 10^{-6}$	$6.16 \times 10^{-6}$	$6.44 \times 10^{-6}$	$7.66 \times 10^{-6}$

**Table 6**  
(Continued)

Isotope	$Z = 0$	$Z = 0.1 Z_{\odot}$	$Z = 0.5 Z_{\odot}$	$Z = Z_{\odot}$	$Z = 2 Z_{\odot}$	$Z = 3 Z_{\odot}$	$Z = 5 Z_{\odot}$
$^{65}\text{Cu}$	$1.73 \times 10^{-5}$	$1.74 \times 10^{-5}$	$1.73 \times 10^{-5}$	$1.76 \times 10^{-5}$	$1.74 \times 10^{-5}$	$1.62 \times 10^{-5}$	$1.39 \times 10^{-5}$
$^{64}\text{Zn}$	$2.13 \times 10^{-4}$	$1.88 \times 10^{-4}$	$1.20 \times 10^{-4}$	$1.16 \times 10^{-4}$	$1.12 \times 10^{-4}$	$1.0 \times 10^{-4}$	$8.22 \times 10^{-5}$
$^{66}\text{Zn}$	$3.87 \times 10^{-5}$	$4.6 \times 10^{-5}$	$4.33 \times 10^{-5}$	$5.2 \times 10^{-5}$	$5.65 \times 10^{-5}$	$5.75 \times 10^{-5}$	$6.31 \times 10^{-5}$
$^{67}\text{Zn}$	$4.83 \times 10^{-6}$	$4.83 \times 10^{-6}$	$4.18 \times 10^{-6}$	$4.36 \times 10^{-6}$	$4.20 \times 10^{-6}$	$3.70 \times 10^{-6}$	$3.97 \times 10^{-6}$
$^{68}\text{Zn}$	$6.64 \times 10^{-6}$	$6.37 \times 10^{-6}$	$7.52 \times 10^{-6}$	$7.56 \times 10^{-6}$	$7.51 \times 10^{-6}$	$6.36 \times 10^{-6}$	$4.42 \times 10^{-6}$
$^{70}\text{Zn}$	$1.99 \times 10^{-16}$	$2.38 \times 10^{-16}$	$2.40 \times 10^{-15}$	$1.10 \times 10^{-13}$	$1.16 \times 10^{-15}$	$6.22 \times 10^{-12}$	$4.92 \times 10^{-17}$

**Note.** The model at solar metallicity is Model 110-100-2-50. Masses are in units of solar mass.

**Table 7**  
Similar to Table 6, but for the Radioactive Isotopes of the Benchmark Model

$Z (Z_{\odot})$	$Z = 0$	$Z = 0.1$	$Z = 0.5$	$Z = 1$	$Z = 2$	$Z = 3$	$Z = 5$
$^{22}\text{Na}$	$7.32 \times 10^{-9}$	$6.59 \times 10^{-9}$	$1.12 \times 10^{-8}$	$1.25 \times 10^{-8}$	$1.1 \times 10^{-8}$	$7.67 \times 10^{-9}$	$5.26 \times 10^{-9}$
$^{26}\text{Al}$	$1.91 \times 10^{-6}$	$4.30 \times 10^{-6}$	$7.4 \times 10^{-6}$	$6.98 \times 10^{-6}$	$4.45 \times 10^{-6}$	$2.40 \times 10^{-6}$	$1.15 \times 10^{-6}$
$^{39}\text{Ar}$	$5.90 \times 10^{-9}$	$6.5 \times 10^{-9}$	$1.28 \times 10^{-8}$	$1.99 \times 10^{-8}$	$5.54 \times 10^{-8}$	$1.5 \times 10^{-7}$	$1.1 \times 10^{-7}$
$^{40}\text{K}$	$4.99 \times 10^{-8}$	$5.16 \times 10^{-8}$	$8.37 \times 10^{-8}$	$1.23 \times 10^{-7}$	$2.26 \times 10^{-7}$	$2.25 \times 10^{-7}$	$1.15 \times 10^{-7}$
$^{41}\text{Ca}$	$2.4 \times 10^{-6}$	$3.63 \times 10^{-6}$	$6.65 \times 10^{-6}$	$8.49 \times 10^{-6}$	$9.99 \times 10^{-6}$	$9.51 \times 10^{-6}$	$7.23 \times 10^{-6}$
$^{44}\text{Ti}$	$5.52 \times 10^{-4}$	$5.50 \times 10^{-4}$	$5.15 \times 10^{-4}$	$5.14 \times 10^{-4}$	$5.12 \times 10^{-4}$	$5.15 \times 10^{-4}$	$4.72 \times 10^{-4}$
$^{48}\text{V}$	$2.93 \times 10^{-6}$	$2.94 \times 10^{-6}$	$3.22 \times 10^{-6}$	$3.26 \times 10^{-6}$	$3.30 \times 10^{-6}$	$2.81 \times 10^{-6}$	$2.9 \times 10^{-6}$
$^{49}\text{V}$	$3.86 \times 10^{-6}$	$3.86 \times 10^{-6}$	$5.9 \times 10^{-6}$	$5.19 \times 10^{-6}$	$5.40 \times 10^{-6}$	$5.30 \times 10^{-6}$	$3.44 \times 10^{-6}$
$^{53}\text{Mn}$	$8.39 \times 10^{-5}$	$8.40 \times 10^{-5}$	$9.34 \times 10^{-5}$	$1.6 \times 10^{-4}$	$1.35 \times 10^{-4}$	$1.84 \times 10^{-4}$	$2.16 \times 10^{-4}$
$^{60}\text{Fe}$	$1.58 \times 10^{-12}$	$1.58 \times 10^{-12}$	$8.29 \times 10^{-12}$	$2.1 \times 10^{-8}$	$8.29 \times 10^{-12}$	$7.23 \times 10^{-9}$	$2.64 \times 10^{-13}$
$^{56}\text{Co}$	$1.14 \times 10^{-4}$	$1.15 \times 10^{-4}$	$8.58 \times 10^{-5}$	$8.95 \times 10^{-5}$	$9.2 \times 10^{-5}$	$8.92 \times 10^{-5}$	$1.51 \times 10^{-4}$
$^{57}\text{Co}$	$8.77 \times 10^{-5}$	$8.79 \times 10^{-5}$	$8.84 \times 10^{-5}$	$1.47 \times 10^{-4}$	$1.3 \times 10^{-4}$	$9.99 \times 10^{-5}$	$1.7 \times 10^{-4}$
$^{60}\text{Co}$	$1.21 \times 10^{-8}$	$1.21 \times 10^{-8}$	$3.6 \times 10^{-8}$	$8.90 \times 10^{-8}$	$3.6 \times 10^{-8}$	$4.63 \times 10^{-7}$	$3.44 \times 10^{-9}$
$^{56}\text{Ni}$	$6.73 \times 10^{-1}$	$6.69 \times 10^{-1}$	$6.33 \times 10^{-1}$	$6.8 \times 10^{-1}$	$5.82 \times 10^{-1}$	$5.55 \times 10^{-1}$	$5.13 \times 10^{-1}$
$^{57}\text{Ni}$	$1.50 \times 10^{-2}$	$1.59 \times 10^{-2}$	$1.82 \times 10^{-2}$	$2.10 \times 10^{-2}$	$2.51 \times 10^{-2}$	$2.83 \times 10^{-2}$	$3.29 \times 10^{-2}$
$^{59}\text{Ni}$	$4.11 \times 10^{-5}$	$4.11 \times 10^{-5}$	$4.9 \times 10^{-5}$	$7.33 \times 10^{-5}$	$4.65 \times 10^{-5}$	$4.82 \times 10^{-5}$	$8.84 \times 10^{-5}$
$^{63}\text{Ni}$	$4.74 \times 10^{-10}$	$4.75 \times 10^{-10}$	$1.55 \times 10^{-9}$	$9.31 \times 10^{-8}$	$1.54 \times 10^{-9}$	$9.77 \times 10^{-8}$	$1.11 \times 10^{-10}$

**Note.** Masses are in units of solar mass.

detonation model can be characterized by the excess of these light Fe-peak elements.

In Figure 23 we plot the  $\rho_{\text{max}}$  against  $T_{\text{max}}$  for the tracer particles of the two models. It can be seen that even for the same  $^4\text{He}$  mass and total mass, the spherical model, whose evolution contains no oblique shock and the detonation wave propagates radially outward only, provides a uniform element distribution. This can be contrasted with the aspherical model, where the scattering in density and temperature is very pronounced.

### 6.6. Constraints on Progenitor Model

The double-detonation model is one of the well-accepted physical models owing to the robustness of initiating the detonation and its variability in producing the dispersion in the observed SN Ia brightness. However, one major concern, in contrast to the near-Chandrasekhar-mass WD, is that the detonation nature can produce a considerable amount of  $^{56}\text{Ni}$  if the detonation is triggered too early, which produces over-luminous SNe Ia. This is incompatible with the majority of SNe Ia, where  $\sim 0.5\text{--}0.7 M_{\odot}$  of  $^{56}\text{Ni}$  is observed as induced by their light curves. In view of that, it becomes important to understand in which condition we could obtain realizations that can resemble the typical SNe. This may provide constraints on the progenitor model, including the typical mass, the He envelope mass, and the initial detonation seed. In particular, the

position of the initial detonation seed is not yet well constrained.

To do so, we plot the  $^{56}\text{Ni}$  mass against progenitor WD mass for different progenitor masses and different explosion mechanisms. In Figure 24 we plot that for the double-detonation models for both the spherical detonation and the aspherical one, which we choose the one-bubble pattern along the  $z$ -axis. For the near-Chandrasekhar-mass WD, we use the standard DDT model with turbulent deflagration as reported in Leung & Nomoto (2017) and Nomoto & Leung (2017).

The sub-Chandrasekhar-mass WD model corresponds to both SD and DD scenarios. We remind that for the violent merger model, due to the compactness of the CO core, the secondary WD is disintegrated when the He detonation starts. Thus, effectively it has a structure similar to the double-detonation model in the SD scenario. In the Chandrasekhar-mass model, it corresponds to the near-Chandrasekhar-mass models presented in Leung & Nomoto (2017) and Nomoto & Leung (2017). In particular, we choose a configuration identical to the benchmark model but for different central density from  $5 \times 10^8$  to  $5 \times 10^9 \text{ g cm}^{-3}$ .

In the sub-Chandrasekhar-mass models ( $0.9\text{--}1.2 M_{\odot}$ ),  $M_{\text{Ni}}$  increases with  $M$  for both spherical (Model 100-050-2-S50) and aspherical (Model 110-050-2-B50) models. This is because, in principle, the whole star is burnt. How complete the nuclear burning depends only on the density. For a lower-mass



Table 8

Nucleosynthesis Yields for the Stable Isotopes of the Benchmark Model with a Spherical He Detonation as a Trigger Based on Model 110-050-2-B50 at Solar Metallicity

$Z (Z_{\odot})$	0	0.1	0.5	1	2	3	5
$^{12}\text{C}$	$4.10 \times 10^{-3}$	$4.9 \times 10^{-3}$	$4.5 \times 10^{-3}$	$4.2 \times 10^{-3}$	$3.95 \times 10^{-3}$	$3.89 \times 10^{-3}$	$3.77 \times 10^{-3}$
$^{13}\text{C}$	$3.66 \times 10^{-10}$	$2.36 \times 10^{-10}$	$2.13 \times 10^{-9}$	$8.97 \times 10^{-9}$	$5.42 \times 10^{-8}$	$8.85 \times 10^{-8}$	$2.8 \times 10^{-7}$
$^{14}\text{N}$	$1.24 \times 10^{-8}$	$8.32 \times 10^{-9}$	$3.57 \times 10^{-8}$	$1.17 \times 10^{-7}$	$5.17 \times 10^{-7}$	$8.47 \times 10^{-7}$	$1.95 \times 10^{-6}$
$^{15}\text{N}$	$1.94 \times 10^{-6}$	$4.25 \times 10^{-8}$	$3.71 \times 10^{-9}$	$1.38 \times 10^{-9}$	$1.49 \times 10^{-9}$	$2.65 \times 10^{-9}$	$8.42 \times 10^{-9}$
$^{16}\text{O}$	$9.80 \times 10^{-2}$	$9.93 \times 10^{-2}$	$1.1 \times 10^{-1}$	$1.2 \times 10^{-1}$	$1.4 \times 10^{-1}$	$1.4 \times 10^{-1}$	$1.2 \times 10^{-1}$
$^{17}\text{O}$	$2.98 \times 10^{-10}$	$1.50 \times 10^{-9}$	$1.52 \times 10^{-8}$	$4.32 \times 10^{-8}$	$8.5 \times 10^{-8}$	$1.6 \times 10^{-7}$	$1.52 \times 10^{-7}$
$^{18}\text{O}$	$1.13 \times 10^{-11}$	$4.34 \times 10^{-11}$	$1.94 \times 10^{-10}$	$5.10 \times 10^{-10}$	$1.96 \times 10^{-9}$	$4.5 \times 10^{-9}$	$1.31 \times 10^{-8}$
$^{19}\text{F}$	$3.96 \times 10^{-10}$	$6.70 \times 10^{-11}$	$2.65 \times 10^{-11}$	$6.80 \times 10^{-11}$	$2.17 \times 10^{-10}$	$3.97 \times 10^{-10}$	$8.63 \times 10^{-10}$
$^{20}\text{Ne}$	$4.90 \times 10^{-3}$	$4.87 \times 10^{-3}$	$4.80 \times 10^{-3}$	$4.72 \times 10^{-3}$	$4.53 \times 10^{-3}$	$4.34 \times 10^{-3}$	$4.3 \times 10^{-3}$
$^{21}\text{Ne}$	$1.39 \times 10^{-8}$	$1.62 \times 10^{-8}$	$1.13 \times 10^{-7}$	$4.33 \times 10^{-7}$	$1.49 \times 10^{-6}$	$3.5 \times 10^{-6}$	$8.24 \times 10^{-6}$
$^{22}\text{Ne}$	$1.43 \times 10^{-8}$	$9.46 \times 10^{-6}$	$4.72 \times 10^{-5}$	$9.46 \times 10^{-5}$	$1.92 \times 10^{-4}$	$2.97 \times 10^{-4}$	$5.24 \times 10^{-4}$
$^{23}\text{Na}$	$9.57 \times 10^{-6}$	$1.2 \times 10^{-5}$	$1.38 \times 10^{-5}$	$2.10 \times 10^{-5}$	$3.61 \times 10^{-5}$	$5.49 \times 10^{-5}$	$1.9 \times 10^{-4}$
$^{24}\text{Mg}$	$1.66 \times 10^{-2}$	$1.55 \times 10^{-2}$	$1.14 \times 10^{-2}$	$8.62 \times 10^{-3}$	$5.74 \times 10^{-3}$	$4.33 \times 10^{-3}$	$3.8 \times 10^{-3}$
$^{25}\text{Mg}$	$2.89 \times 10^{-7}$	$3.66 \times 10^{-6}$	$1.94 \times 10^{-5}$	$4.99 \times 10^{-5}$	$1.18 \times 10^{-4}$	$1.88 \times 10^{-4}$	$3.64 \times 10^{-4}$
$^{26}\text{Mg}$	$3.16 \times 10^{-6}$	$9.62 \times 10^{-6}$	$3.71 \times 10^{-5}$	$7.47 \times 10^{-5}$	$1.61 \times 10^{-4}$	$2.94 \times 10^{-4}$	$8.17 \times 10^{-4}$
$^{26}\text{Al}$	$2.86 \times 10^{-29}$	$2.86 \times 10^{-29}$	$2.86 \times 10^{-29}$	$2.86 \times 10^{-29}$	$2.86 \times 10^{-29}$	$3.61 \times 10^{-28}$	$4.8 \times 10^{-28}$
$^{27}\text{Al}$	$8.57 \times 10^{-5}$	$2.30 \times 10^{-4}$	$5.81 \times 10^{-4}$	$7.17 \times 10^{-4}$	$7.70 \times 10^{-4}$	$7.78 \times 10^{-4}$	$8.34 \times 10^{-4}$
$^{28}\text{Si}$	$1.5 \times 10^{-1}$	$1.10 \times 10^{-1}$	$1.11 \times 10^{-1}$	$1.10 \times 10^{-1}$	$1.8 \times 10^{-1}$	$1.6 \times 10^{-1}$	$1.0 \times 10^{-1}$
$^{29}\text{Si}$	$5.9 \times 10^{-5}$	$2.26 \times 10^{-4}$	$4.78 \times 10^{-4}$	$8.24 \times 10^{-4}$	$1.61 \times 10^{-3}$	$2.46 \times 10^{-3}$	$4.53 \times 10^{-3}$
$^{30}\text{Si}$	$3.23 \times 10^{-5}$	$7.15 \times 10^{-5}$	$6.93 \times 10^{-4}$	$1.58 \times 10^{-3}$	$3.44 \times 10^{-3}$	$5.58 \times 10^{-3}$	$1.9 \times 10^{-2}$
$^{31}\text{P}$	$8.39 \times 10^{-5}$	$5.42 \times 10^{-5}$	$2.6 \times 10^{-4}$	$3.54 \times 10^{-4}$	$5.97 \times 10^{-4}$	$8.3 \times 10^{-4}$	$1.11 \times 10^{-3}$
$^{32}\text{S}$	$5.10 \times 10^{-2}$	$4.92 \times 10^{-2}$	$4.96 \times 10^{-2}$	$4.90 \times 10^{-2}$	$4.56 \times 10^{-2}$	$4.16 \times 10^{-2}$	$3.41 \times 10^{-2}$
$^{33}\text{S}$	$4.7 \times 10^{-5}$	$1.6 \times 10^{-4}$	$2.24 \times 10^{-4}$	$3.8 \times 10^{-4}$	$4.10 \times 10^{-4}$	$4.67 \times 10^{-4}$	$4.98 \times 10^{-4}$
$^{34}\text{S}$	$3.93 \times 10^{-6}$	$1.4 \times 10^{-4}$	$8.85 \times 10^{-4}$	$1.97 \times 10^{-3}$	$4.35 \times 10^{-3}$	$6.78 \times 10^{-3}$	$1.9 \times 10^{-2}$
$^{36}\text{S}$	$2.78 \times 10^{-11}$	$1.31 \times 10^{-9}$	$3.34 \times 10^{-8}$	$1.82 \times 10^{-7}$	$1.73 \times 10^{-6}$	$6.42 \times 10^{-6}$	$2.23 \times 10^{-5}$
$^{35}\text{Cl}$	$7.90 \times 10^{-6}$	$1.78 \times 10^{-5}$	$7.8 \times 10^{-5}$	$1.30 \times 10^{-4}$	$2.12 \times 10^{-4}$	$2.35 \times 10^{-4}$	$1.91 \times 10^{-4}$
$^{37}\text{Cl}$	$3.6 \times 10^{-6}$	$8.88 \times 10^{-6}$	$1.73 \times 10^{-5}$	$2.37 \times 10^{-5}$	$3.21 \times 10^{-5}$	$3.67 \times 10^{-5}$	$3.95 \times 10^{-5}$
$^{36}\text{Ar}$	$1.2 \times 10^{-2}$	$8.94 \times 10^{-3}$	$8.21 \times 10^{-3}$	$7.52 \times 10^{-3}$	$6.22 \times 10^{-3}$	$5.18 \times 10^{-3}$	$3.69 \times 10^{-3}$
$^{38}\text{Ar}$	$1.6 \times 10^{-6}$	$6.0 \times 10^{-5}$	$4.77 \times 10^{-4}$	$1.4 \times 10^{-3}$	$2.19 \times 10^{-3}$	$3.21 \times 10^{-3}$	$4.63 \times 10^{-3}$
$^{40}\text{Ar}$	$4.66 \times 10^{-12}$	$1.12 \times 10^{-11}$	$3.25 \times 10^{-10}$	$3.4 \times 10^{-9}$	$3.91 \times 10^{-8}$	$1.46 \times 10^{-7}$	$4.31 \times 10^{-7}$
$^{39}\text{K}$	$7.10 \times 10^{-6}$	$2.5 \times 10^{-5}$	$5.70 \times 10^{-5}$	$8.52 \times 10^{-5}$	$1.15 \times 10^{-4}$	$1.21 \times 10^{-4}$	$1.3 \times 10^{-4}$
$^{40}\text{K}$	$5.89 \times 10^{-10}$	$1.90 \times 10^{-9}$	$1.41 \times 10^{-8}$	$5.41 \times 10^{-8}$	$1.58 \times 10^{-7}$	$1.83 \times 10^{-7}$	$9.4 \times 10^{-8}$
$^{41}\text{K}$	$1.20 \times 10^{-6}$	$2.76 \times 10^{-6}$	$4.41 \times 10^{-6}$	$5.66 \times 10^{-6}$	$6.76 \times 10^{-6}$	$6.64 \times 10^{-6}$	$5.36 \times 10^{-6}$
$^{40}\text{Ca}$	$1.6 \times 10^{-2}$	$8.91 \times 10^{-3}$	$7.69 \times 10^{-3}$	$6.87 \times 10^{-3}$	$5.71 \times 10^{-3}$	$4.96 \times 10^{-3}$	$3.97 \times 10^{-3}$
$^{42}\text{Ca}$	$2.10 \times 10^{-6}$	$3.60 \times 10^{-6}$	$1.63 \times 10^{-5}$	$3.39 \times 10^{-5}$	$6.60 \times 10^{-5}$	$8.89 \times 10^{-5}$	$1.5 \times 10^{-4}$
$^{43}\text{Ca}$	$1.36 \times 10^{-5}$	$1.37 \times 10^{-5}$	$1.39 \times 10^{-5}$	$1.39 \times 10^{-5}$	$1.38 \times 10^{-5}$	$1.38 \times 10^{-5}$	$1.39 \times 10^{-5}$
$^{44}\text{Ca}$	$6.2 \times 10^{-4}$	$6.1 \times 10^{-4}$	$6.0 \times 10^{-4}$	$5.99 \times 10^{-4}$	$6.0 \times 10^{-4}$	$5.97 \times 10^{-4}$	$5.97 \times 10^{-4}$
$^{46}\text{Ca}$	$1.84 \times 10^{-16}$	$4.41 \times 10^{-15}$	$2.86 \times 10^{-12}$	$6.92 \times 10^{-11}$	$9.5 \times 10^{-10}$	$2.14 \times 10^{-9}$	$2.49 \times 10^{-9}$
$^{48}\text{Ca}$	$4.80 \times 10^{-23}$	$3.60 \times 10^{-21}$	$5.54 \times 10^{-18}$	$5.8 \times 10^{-16}$	$6.53 \times 10^{-14}$	$5.43 \times 10^{-13}$	$3.19 \times 10^{-12}$
$^{45}\text{Sc}$	$6.14 \times 10^{-7}$	$6.72 \times 10^{-7}$	$7.34 \times 10^{-7}$	$7.81 \times 10^{-7}$	$8.9 \times 10^{-7}$	$7.97 \times 10^{-7}$	$7.65 \times 10^{-7}$
$^{46}\text{Ti}$	$9.74 \times 10^{-7}$	$1.64 \times 10^{-6}$	$7.69 \times 10^{-6}$	$1.53 \times 10^{-5}$	$2.72 \times 10^{-5}$	$3.35 \times 10^{-5}$	$3.33 \times 10^{-5}$
$^{47}\text{Ti}$	$6.53 \times 10^{-5}$	$6.54 \times 10^{-5}$	$6.57 \times 10^{-5}$	$6.58 \times 10^{-5}$	$6.61 \times 10^{-5}$	$6.64 \times 10^{-5}$	$6.67 \times 10^{-5}$
$^{48}\text{Ti}$	$2.68 \times 10^{-3}$	$2.65 \times 10^{-3}$	$2.63 \times 10^{-3}$	$2.61 \times 10^{-3}$	$2.59 \times 10^{-3}$	$2.59 \times 10^{-3}$	$2.58 \times 10^{-3}$
$^{49}\text{Ti}$	$2.38 \times 10^{-5}$	$2.64 \times 10^{-5}$	$2.76 \times 10^{-5}$	$2.83 \times 10^{-5}$	$2.87 \times 10^{-5}$	$2.93 \times 10^{-5}$	$3.3 \times 10^{-5}$
$^{50}\text{Ti}$	$1.3 \times 10^{-13}$	$2.70 \times 10^{-13}$	$9.62 \times 10^{-11}$	$7.12 \times 10^{-10}$	$1.93 \times 10^{-9}$	$2.48 \times 10^{-9}$	$6.33 \times 10^{-9}$
$^{50}\text{V}$	$4.85 \times 10^{-10}$	$4.94 \times 10^{-10}$	$1.39 \times 10^{-9}$	$3.86 \times 10^{-9}$	$6.34 \times 10^{-9}$	$1.9 \times 10^{-8}$	$3.20 \times 10^{-8}$
$^{51}\text{V}$	$2.67 \times 10^{-4}$	$2.69 \times 10^{-4}$	$2.76 \times 10^{-4}$	$2.81 \times 10^{-4}$	$2.86 \times 10^{-4}$	$2.95 \times 10^{-4}$	$3.12 \times 10^{-4}$
$^{50}\text{Cr}$	$1.69 \times 10^{-5}$	$2.32 \times 10^{-5}$	$5.98 \times 10^{-5}$	$1.9 \times 10^{-4}$	$2.10 \times 10^{-4}$	$2.80 \times 10^{-4}$	$3.48 \times 10^{-4}$
$^{52}\text{Cr}$	$3.34 \times 10^{-3}$	$3.19 \times 10^{-3}$	$2.95 \times 10^{-3}$	$2.80 \times 10^{-3}$	$2.73 \times 10^{-3}$	$2.93 \times 10^{-3}$	$3.83 \times 10^{-3}$
$^{53}\text{Cr}$	$7.22 \times 10^{-5}$	$1.6 \times 10^{-4}$	$1.34 \times 10^{-4}$	$1.56 \times 10^{-4}$	$2.3 \times 10^{-4}$	$2.78 \times 10^{-4}$	$4.48 \times 10^{-4}$
$^{54}\text{Cr}$	$2.68 \times 10^{-8}$	$2.70 \times 10^{-8}$	$3.58 \times 10^{-8}$	$6.70 \times 10^{-8}$	$2.54 \times 10^{-7}$	$7.23 \times 10^{-7}$	$2.23 \times 10^{-6}$
$^{55}\text{Mn}$	$3.56 \times 10^{-4}$	$4.89 \times 10^{-4}$	$7.29 \times 10^{-4}$	$9.15 \times 10^{-4}$	$1.39 \times 10^{-3}$	$2.41 \times 10^{-3}$	$6.72 \times 10^{-3}$
$^{54}\text{Fe}$	$1.97 \times 10^{-4}$	$6.46 \times 10^{-4}$	$2.70 \times 10^{-3}$	$5.20 \times 10^{-3}$	$9.87 \times 10^{-3}$	$1.49 \times 10^{-2}$	$3.68 \times 10^{-2}$
$^{56}\text{Fe}$	$7.25 \times 10^{-1}$	$7.21 \times 10^{-1}$	$7.4 \times 10^{-1}$	$6.84 \times 10^{-1}$	$6.45 \times 10^{-1}$	$6.8 \times 10^{-1}$	$5.32 \times 10^{-1}$
$^{57}\text{Fe}$	$1.16 \times 10^{-2}$	$1.26 \times 10^{-2}$	$1.57 \times 10^{-2}$	$1.90 \times 10^{-2}$	$2.41 \times 10^{-2}$	$2.77 \times 10^{-2}$	$3.12 \times 10^{-2}$
$^{58}\text{Fe}$	$3.70 \times 10^{-8}$	$3.72 \times 10^{-8}$	$3.99 \times 10^{-8}$	$4.83 \times 10^{-8}$	$8.49 \times 10^{-8}$	$1.46 \times 10^{-7}$	$2.97 \times 10^{-7}$
$^{60}\text{Fe}$	$1.45 \times 10^{-19}$	$1.52 \times 10^{-19}$	$4.18 \times 10^{-19}$	$1.11 \times 10^{-18}$	$2.0 \times 10^{-18}$	$1.94 \times 10^{-18}$	$1.24 \times 10^{-17}$
$^{59}\text{Co}$	$6.73 \times 10^{-5}$	$1.25 \times 10^{-4}$	$4.59 \times 10^{-4}$	$6.17 \times 10^{-4}$	$7.33 \times 10^{-4}$	$6.72 \times 10^{-4}$	$4.46 \times 10^{-4}$
$^{58}\text{Ni}$	$9.17 \times 10^{-4}$	$1.82 \times 10^{-3}$	$1.41 \times 10^{-2}$	$3.6 \times 10^{-2}$	$6.46 \times 10^{-2}$	$9.80 \times 10^{-2}$	$1.51 \times 10^{-1}$
$^{60}\text{Ni}$	$8.66 \times 10^{-3}$	$8.96 \times 10^{-3}$	$7.64 \times 10^{-3}$	$6.41 \times 10^{-3}$	$4.44 \times 10^{-3}$	$2.89 \times 10^{-3}$	$1.22 \times 10^{-3}$
$^{61}\text{Ni}$	$1.90 \times 10^{-4}$	$2.5 \times 10^{-4}$	$2.32 \times 10^{-4}$	$2.48 \times 10^{-4}$	$2.37 \times 10^{-4}$	$1.98 \times 10^{-4}$	$1.22 \times 10^{-4}$
$^{62}\text{Ni}$	$1.7 \times 10^{-4}$	$2.96 \times 10^{-4}$	$1.7 \times 10^{-3}$	$1.83 \times 10^{-3}$	$2.70 \times 10^{-3}$	$2.83 \times 10^{-3}$	$2.20 \times 10^{-3}$
$^{64}\text{Ni}$	$7.90 \times 10^{-13}$	$9.44 \times 10^{-13}$	$9.52 \times 10^{-13}$	$8.3 \times 10^{-13}$	$7.94 \times 10^{-13}$	$8.17 \times 10^{-13}$	$8.46 \times 10^{-13}$
$^{63}\text{Cu}$	$1.90 \times 10^{-6}$	$3.14 \times 10^{-6}$	$1.85 \times 10^{-6}$	$2.24 \times 10^{-6}$	$2.89 \times 10^{-6}$	$3.20 \times 10^{-6}$	$3.9 \times 10^{-6}$

**Table 8**  
(Continued)

$Z (Z_{\odot})$	0	0.1	0.5	1	2	3	5
$^{65}\text{Cu}$	$3.34 \times 10^{-6}$	$3.42 \times 10^{-6}$	$3.47 \times 10^{-6}$	$3.49 \times 10^{-6}$	$3.35 \times 10^{-6}$	$3.22 \times 10^{-6}$	$2.89 \times 10^{-6}$
$^{64}\text{Zn}$	$1.30 \times 10^{-4}$	$8.61 \times 10^{-5}$	$1.68 \times 10^{-5}$	$1.30 \times 10^{-5}$	$9.70 \times 10^{-6}$	$7.81 \times 10^{-6}$	$6.14 \times 10^{-6}$
$^{66}\text{Zn}$	$7.96 \times 10^{-6}$	$9.62 \times 10^{-6}$	$1.58 \times 10^{-5}$	$2.15 \times 10^{-5}$	$2.67 \times 10^{-5}$	$2.71 \times 10^{-5}$	$2.33 \times 10^{-5}$
$^{67}\text{Zn}$	$1.21 \times 10^{-6}$	$1.20 \times 10^{-6}$	$1.20 \times 10^{-6}$	$1.21 \times 10^{-6}$	$1.21 \times 10^{-6}$	$1.24 \times 10^{-6}$	$1.24 \times 10^{-6}$
$^{68}\text{Zn}$	$8.43 \times 10^{-7}$	$5.39 \times 10^{-7}$	$4.9 \times 10^{-7}$	$4.7 \times 10^{-7}$	$4.7 \times 10^{-7}$	$4.17 \times 10^{-7}$	$4.22 \times 10^{-7}$
$^{70}\text{Zn}$	$5.14 \times 10^{-17}$	$5.52 \times 10^{-17}$	$4.40 \times 10^{-15}$	$5.22 \times 10^{-17}$	$5.14 \times 10^{-17}$	$5.7 \times 10^{-17}$	$5.6 \times 10^{-17}$

**Note.** Masses are in units of solar mass.

**Table 9**  
Similar to Table 8, but for the Nucleosynthesis Yields for Radioactive Isotopes of the Benchmark Models

$Z (Z_{\odot})$	0	0.1	0.5	1	2	3	5
$^{22}\text{Na}$	$9.63 \times 10^{-9}$	$8.92 \times 10^{-9}$	$1.40 \times 10^{-8}$	$1.56 \times 10^{-8}$	$1.24 \times 10^{-8}$	$9.89 \times 10^{-9}$	$7.6 \times 10^{-9}$
$^{26}\text{Al}$	$2.54 \times 10^{-6}$	$5.47 \times 10^{-6}$	$8.71 \times 10^{-6}$	$8.12 \times 10^{-6}$	$5.7 \times 10^{-6}$	$3.16 \times 10^{-6}$	$1.44 \times 10^{-6}$
$^{39}\text{Ar}$	$9.85 \times 10^{-12}$	$1.14 \times 10^{-10}$	$1.75 \times 10^{-9}$	$8.69 \times 10^{-9}$	$4.57 \times 10^{-8}$	$9.15 \times 10^{-8}$	$1.3 \times 10^{-7}$
$^{40}\text{K}$	$5.92 \times 10^{-10}$	$1.91 \times 10^{-9}$	$1.42 \times 10^{-8}$	$5.44 \times 10^{-8}$	$1.59 \times 10^{-7}$	$1.84 \times 10^{-7}$	$9.9 \times 10^{-8}$
$^{41}\text{Ca}$	$1.5 \times 10^{-6}$	$2.59 \times 10^{-6}$	$4.44 \times 10^{-6}$	$5.71 \times 10^{-6}$	$6.75 \times 10^{-6}$	$6.65 \times 10^{-6}$	$5.31 \times 10^{-6}$
$^{44}\text{Ti}$	$6.3 \times 10^{-4}$	$6.1 \times 10^{-4}$	$6.0 \times 10^{-4}$	$5.99 \times 10^{-4}$	$5.97 \times 10^{-4}$	$5.97 \times 10^{-4}$	$5.95 \times 10^{-4}$
$^{48}\text{V}$	$1.11 \times 10^{-6}$	$1.12 \times 10^{-6}$	$1.13 \times 10^{-6}$	$1.15 \times 10^{-6}$	$1.19 \times 10^{-6}$	$1.21 \times 10^{-6}$	$1.20 \times 10^{-6}$
$^{49}\text{V}$	$8.16 \times 10^{-8}$	$8.42 \times 10^{-8}$	$1.21 \times 10^{-7}$	$1.85 \times 10^{-7}$	$3.38 \times 10^{-7}$	$5.81 \times 10^{-7}$	$1.12 \times 10^{-6}$
$^{53}\text{Mn}$	$2.72 \times 10^{-6}$	$2.84 \times 10^{-6}$	$5.18 \times 10^{-6}$	$1.15 \times 10^{-5}$	$4.51 \times 10^{-5}$	$9.98 \times 10^{-5}$	$1.83 \times 10^{-4}$
$^{60}\text{Fe}$	$2.14 \times 10^{-18}$	$2.26 \times 10^{-18}$	$5.98 \times 10^{-18}$	$1.62 \times 10^{-17}$	$3.0 \times 10^{-17}$	$2.78 \times 10^{-17}$	$1.78 \times 10^{-16}$
$^{56}\text{Co}$	$1.56 \times 10^{-5}$	$1.59 \times 10^{-5}$	$1.67 \times 10^{-5}$	$1.79 \times 10^{-5}$	$2.4 \times 10^{-5}$	$2.57 \times 10^{-5}$	$5.77 \times 10^{-5}$
$^{57}\text{Co}$	$5.43 \times 10^{-6}$	$5.56 \times 10^{-6}$	$6.93 \times 10^{-6}$	$9.87 \times 10^{-6}$	$2.4 \times 10^{-5}$	$3.2 \times 10^{-5}$	$4.37 \times 10^{-5}$
$^{60}\text{Co}$	$5.85 \times 10^{-13}$	$5.93 \times 10^{-13}$	$6.10 \times 10^{-13}$	$6.59 \times 10^{-13}$	$1.7 \times 10^{-12}$	$2.25 \times 10^{-12}$	$8.29 \times 10^{-12}$
$^{56}\text{Ni}$	$7.25 \times 10^{-1}$	$7.21 \times 10^{-1}$	$7.4 \times 10^{-1}$	$6.84 \times 10^{-1}$	$6.45 \times 10^{-1}$	$6.6 \times 10^{-1}$	$5.29 \times 10^{-1}$
$^{57}\text{Ni}$	$1.16 \times 10^{-2}$	$1.26 \times 10^{-2}$	$1.57 \times 10^{-2}$	$1.90 \times 10^{-2}$	$2.41 \times 10^{-2}$	$2.76 \times 10^{-2}$	$3.11 \times 10^{-2}$
$^{59}\text{Ni}$	$3.31 \times 10^{-6}$	$3.36 \times 10^{-6}$	$3.80 \times 10^{-6}$	$4.77 \times 10^{-6}$	$8.56 \times 10^{-6}$	$1.96 \times 10^{-5}$	$6.77 \times 10^{-5}$
$^{63}\text{Ni}$	$2.55 \times 10^{-14}$	$5.3 \times 10^{-14}$	$2.88 \times 10^{-14}$	$2.62 \times 10^{-14}$	$2.95 \times 10^{-14}$	$4.33 \times 10^{-14}$	$1.26 \times 10^{-13}$

**Note.** Masses are in units of solar mass.

WD, there is less matter with sufficient density to reach complete burning (typically  $5 \times 10^7 \text{ g cm}^{-3}$ ). Therefore, the  $^{56}\text{Ni}$  scales almost linearly with  $M$ . On the other hand, in the Chandrasekhar-mass models,  $M_{\text{Ni}}$  decreases with  $M$ . This is related to the more efficient electron capture in the matter burnt by deflagration, which lowers the matter electron fraction. As  $^{56}\text{Ni}$  is produced in NSE while  $^{56}\text{Ni}$  has an electron fraction of 0.5, any electron capture in the matter will only suppress the production of  $^{56}\text{Ni}$ .

We note that we compute both Chandrasekhar and sub-Chandrasekhar mass models for a mass of 1.2–1.3  $M_{\odot}$ . This is because in this intermediate regime it is unclear whether the thermonuclear runaway occurs in the form of deflagration or detonation, because the pressure jump becomes close to the initial pressure (Nomoto et al. 1976; Nomoto 1982b; Nomoto et al. 1984). Therefore, both models cannot be ruled out. By examining the overlapping mass range for all three curves, it can be seen that the sub-Chandrasekhar-mass branch has an  $M_{\text{Ni}}$  lower than the Chandrasekhar-mass branch. Future statistics of observed SNe Ia for this pair of quantities will resolve the uncertainty here.

Finally, we explain the difference of  $M_{^{56}\text{Ni}}$  between the spherical and aspherical models. The spherical model in general produces more  $^{56}\text{Ni}$  than the aspherical model for the same  $M$ . This is because the C detonation starts in the center for the spherical model and off-center for the aspherical one. However, most the  $^{56}\text{Ni}$  is produced near the center, where the density is the highest. This means that for aspherical detonation

to produce  $^{56}\text{Ni}$ , it needs to overcome the density gradient and the outward motion of the WD during expansion. This requires more time for the detonation to reach the center to burn the matter for synthesizing  $^{56}\text{Ni}$ , while the WD has started its expansion. As a result, the matter density burnt by aspherical detonation in general is lower, which suppresses the production of  $^{56}\text{Ni}$ . Future observations of SN Ia mass and  $^{56}\text{Ni}$  mass can provide further constraints on this degeneracy and hence the asphericity of the initial He detonation.

### 6.7. Contribution to Galactic Chemical Evolution

The SD (Chandrasekhar-mass model) versus DD (sub-Chandrasekhar-mass model) scenario is a long-lasting theoretical tension that has remained unsolved. The Chandrasekhar-mass model has been favored because of its correspondence to an invariant model that can explain the similarity among observed SNe Ia. However, the shock-companion star interaction is shown to provide strong X-ray signal before the bolometric maximum of the light curves (Kasen 2010). The absence or nondiscovery of such a feature leads to the consideration of using the sub-Chandrasekhar-mass model as an alternative to explain the origin of SNe Ia.

To compare how the sub-Chandrasekhar-mass model influences the metal enrichment process, we first compare the chemical yield directly. In Figure 25 we compare the chemical yield of the benchmark models of this work, namely, Model 110-100-2-50 (top panel) and Model 100-050-2-S50 (lower

Table 10

Nucleosynthesis Yields for the Stable Isotopes of the Benchmark Model with a Spherical He Detonation as a Trigger Based on Model 100-050-2-S50 at Different Metallicities

$Z (Z_{\odot})$	0	0.1	0.5	1	2	3	5
$^{12}\text{C}$	$1.18 \times 10^{-3}$	$1.17 \times 10^{-3}$	$1.16 \times 10^{-3}$	$1.15 \times 10^{-3}$	$1.13 \times 10^{-3}$	$1.13 \times 10^{-3}$	$1.11 \times 10^{-3}$
$^{13}\text{C}$	$1.4 \times 10^{-10}$	$8.4 \times 10^{-11}$	$8.87 \times 10^{-10}$	$3.2 \times 10^{-9}$	$1.21 \times 10^{-8}$	$3.70 \times 10^{-8}$	$1.9 \times 10^{-7}$
$^{14}\text{N}$	$3.94 \times 10^{-9}$	$1.76 \times 10^{-9}$	$9.2 \times 10^{-9}$	$1.81 \times 10^{-8}$	$7.5 \times 10^{-8}$	$2.52 \times 10^{-7}$	$6.87 \times 10^{-7}$
$^{15}\text{N}$	$1.0 \times 10^{-6}$	$4.93 \times 10^{-9}$	$5.68 \times 10^{-10}$	$2.13 \times 10^{-10}$	$3.20 \times 10^{-10}$	$1.42 \times 10^{-9}$	$5.54 \times 10^{-9}$
$^{16}\text{O}$	$5.90 \times 10^{-2}$	$6.34 \times 10^{-2}$	$6.55 \times 10^{-2}$	$6.64 \times 10^{-2}$	$6.68 \times 10^{-2}$	$6.64 \times 10^{-2}$	$6.48 \times 10^{-2}$
$^{17}\text{O}$	$9.61 \times 10^{-11}$	$2.70 \times 10^{-10}$	$4.18 \times 10^{-9}$	$1.8 \times 10^{-8}$	$2.3 \times 10^{-8}$	$2.43 \times 10^{-8}$	$2.52 \times 10^{-8}$
$^{18}\text{O}$	$3.29 \times 10^{-12}$	$8.33 \times 10^{-12}$	$6.40 \times 10^{-11}$	$9.43 \times 10^{-11}$	$4.35 \times 10^{-10}$	$2.21 \times 10^{-9}$	$8.97 \times 10^{-9}$
$^{19}\text{F}$	$5.92 \times 10^{-11}$	$7.31 \times 10^{-12}$	$7.99 \times 10^{-12}$	$2.39 \times 10^{-11}$	$7.87 \times 10^{-11}$	$1.70 \times 10^{-10}$	$2.95 \times 10^{-10}$
$^{20}\text{Ne}$	$1.30 \times 10^{-3}$	$1.27 \times 10^{-3}$	$1.21 \times 10^{-3}$	$1.15 \times 10^{-3}$	$1.8 \times 10^{-3}$	$1.4 \times 10^{-3}$	$9.83 \times 10^{-4}$
$^{21}\text{Ne}$	$2.97 \times 10^{-9}$	$5.41 \times 10^{-9}$	$5.8 \times 10^{-8}$	$1.57 \times 10^{-7}$	$5.91 \times 10^{-7}$	$1.56 \times 10^{-6}$	$4.5 \times 10^{-6}$
$^{22}\text{Ne}$	$5.70 \times 10^{-9}$	$3.38 \times 10^{-9}$	$5.77 \times 10^{-9}$	$9.25 \times 10^{-9}$	$6.35 \times 10^{-7}$	$6.45 \times 10^{-6}$	$4.12 \times 10^{-5}$
$^{23}\text{Na}$	$3.59 \times 10^{-6}$	$3.86 \times 10^{-6}$	$5.77 \times 10^{-6}$	$8.39 \times 10^{-6}$	$1.58 \times 10^{-5}$	$2.80 \times 10^{-5}$	$5.31 \times 10^{-5}$
$^{24}\text{Mg}$	$3.69 \times 10^{-3}$	$3.10 \times 10^{-3}$	$1.84 \times 10^{-3}$	$1.28 \times 10^{-3}$	$8.70 \times 10^{-4}$	$7.14 \times 10^{-4}$	$6.29 \times 10^{-4}$
$^{25}\text{Mg}$	$1.9 \times 10^{-7}$	$8.53 \times 10^{-7}$	$6.20 \times 10^{-6}$	$1.45 \times 10^{-5}$	$3.43 \times 10^{-5}$	$5.87 \times 10^{-5}$	$1.11 \times 10^{-4}$
$^{26}\text{Mg}$	$1.26 \times 10^{-6}$	$3.45 \times 10^{-6}$	$1.35 \times 10^{-5}$	$2.89 \times 10^{-5}$	$6.82 \times 10^{-5}$	$1.13 \times 10^{-4}$	$2.74 \times 10^{-4}$
$^{26}\text{Al}$	$2.60 \times 10^{-29}$	$2.60 \times 10^{-29}$	$2.60 \times 10^{-29}$	$2.60 \times 10^{-29}$	$2.60 \times 10^{-29}$	$2.60 \times 10^{-29}$	$3.57 \times 10^{-11}$
$^{27}\text{Al}$	$2.45 \times 10^{-5}$	$4.76 \times 10^{-5}$	$9.84 \times 10^{-5}$	$1.14 \times 10^{-4}$	$1.23 \times 10^{-4}$	$1.33 \times 10^{-4}$	$1.72 \times 10^{-4}$
$^{28}\text{Si}$	$1.14 \times 10^{-1}$	$1.18 \times 10^{-1}$	$1.22 \times 10^{-1}$	$1.25 \times 10^{-1}$	$1.26 \times 10^{-1}$	$1.26 \times 10^{-1}$	$1.22 \times 10^{-1}$
$^{29}\text{Si}$	$2.22 \times 10^{-5}$	$9.34 \times 10^{-5}$	$1.71 \times 10^{-4}$	$2.67 \times 10^{-4}$	$4.74 \times 10^{-4}$	$7.4 \times 10^{-4}$	$1.24 \times 10^{-3}$
$^{30}\text{Si}$	$1.66 \times 10^{-5}$	$2.23 \times 10^{-5}$	$1.69 \times 10^{-4}$	$3.79 \times 10^{-4}$	$9.29 \times 10^{-4}$	$1.73 \times 10^{-3}$	$4.50 \times 10^{-3}$
$^{31}\text{P}$	$4.4 \times 10^{-5}$	$2.88 \times 10^{-5}$	$9.33 \times 10^{-5}$	$1.53 \times 10^{-4}$	$2.64 \times 10^{-4}$	$3.74 \times 10^{-4}$	$5.61 \times 10^{-4}$
$^{32}\text{S}$	$7.11 \times 10^{-2}$	$6.89 \times 10^{-2}$	$6.81 \times 10^{-2}$	$6.56 \times 10^{-2}$	$5.89 \times 10^{-2}$	$5.28 \times 10^{-2}$	$4.28 \times 10^{-2}$
$^{33}\text{S}$	$1.64 \times 10^{-5}$	$7.31 \times 10^{-5}$	$1.39 \times 10^{-4}$	$1.89 \times 10^{-4}$	$2.65 \times 10^{-4}$	$3.19 \times 10^{-4}$	$3.71 \times 10^{-4}$
$^{34}\text{S}$	$4.3 \times 10^{-6}$	$1.15 \times 10^{-4}$	$8.82 \times 10^{-4}$	$1.91 \times 10^{-3}$	$4.13 \times 10^{-3}$	$6.58 \times 10^{-3}$	$1.14 \times 10^{-2}$
$^{36}\text{S}$	$4.11 \times 10^{-12}$	$5.80 \times 10^{-10}$	$9.34 \times 10^{-9}$	$6.35 \times 10^{-8}$	$6.23 \times 10^{-7}$	$1.81 \times 10^{-6}$	$4.76 \times 10^{-6}$
$^{35}\text{Cl}$	$8.25 \times 10^{-6}$	$1.80 \times 10^{-5}$	$6.35 \times 10^{-5}$	$1.4 \times 10^{-4}$	$1.57 \times 10^{-4}$	$1.75 \times 10^{-4}$	$1.59 \times 10^{-4}$
$^{37}\text{Cl}$	$2.23 \times 10^{-6}$	$9.59 \times 10^{-6}$	$1.85 \times 10^{-5}$	$2.51 \times 10^{-5}$	$3.32 \times 10^{-5}$	$3.58 \times 10^{-5}$	$3.39 \times 10^{-5}$
$^{36}\text{Ar}$	$1.55 \times 10^{-2}$	$1.41 \times 10^{-2}$	$1.28 \times 10^{-2}$	$1.15 \times 10^{-2}$	$9.49 \times 10^{-3}$	$8.2 \times 10^{-3}$	$6.1 \times 10^{-3}$
$^{38}\text{Ar}$	$6.21 \times 10^{-7}$	$8.62 \times 10^{-5}$	$6.28 \times 10^{-4}$	$1.34 \times 10^{-3}$	$2.70 \times 10^{-3}$	$3.87 \times 10^{-3}$	$5.30 \times 10^{-3}$
$^{40}\text{Ar}$	$7.66 \times 10^{-14}$	$4.26 \times 10^{-12}$	$1.64 \times 10^{-10}$	$1.71 \times 10^{-9}$	$1.62 \times 10^{-8}$	$4.42 \times 10^{-8}$	$1.14 \times 10^{-7}$
$^{39}\text{K}$	$5.8 \times 10^{-6}$	$2.17 \times 10^{-5}$	$6.27 \times 10^{-5}$	$9.25 \times 10^{-5}$	$1.22 \times 10^{-4}$	$1.24 \times 10^{-4}$	$1.2 \times 10^{-4}$
$^{40}\text{K}$	$4.81 \times 10^{-11}$	$1.58 \times 10^{-9}$	$1.21 \times 10^{-8}$	$3.84 \times 10^{-8}$	$8.59 \times 10^{-8}$	$9.1 \times 10^{-8}$	$5.60 \times 10^{-8}$
$^{41}\text{K}$	$7.4 \times 10^{-7}$	$2.71 \times 10^{-6}$	$4.54 \times 10^{-6}$	$5.64 \times 10^{-6}$	$6.64 \times 10^{-6}$	$6.37 \times 10^{-6}$	$4.80 \times 10^{-6}$
$^{40}\text{Ca}$	$1.61 \times 10^{-2}$	$1.40 \times 10^{-2}$	$1.19 \times 10^{-2}$	$1.4 \times 10^{-2}$	$8.49 \times 10^{-3}$	$7.33 \times 10^{-3}$	$5.81 \times 10^{-3}$
$^{42}\text{Ca}$	$3.55 \times 10^{-7}$	$2.58 \times 10^{-6}$	$1.97 \times 10^{-5}$	$4.24 \times 10^{-5}$	$7.93 \times 10^{-5}$	$1.1 \times 10^{-4}$	$1.10 \times 10^{-4}$
$^{43}\text{Ca}$	$1.31 \times 10^{-5}$	$1.36 \times 10^{-5}$	$1.39 \times 10^{-5}$	$1.38 \times 10^{-5}$	$1.36 \times 10^{-5}$	$1.36 \times 10^{-5}$	$1.37 \times 10^{-5}$
$^{44}\text{Ca}$	$2.78 \times 10^{-4}$	$2.76 \times 10^{-4}$	$2.65 \times 10^{-4}$	$2.63 \times 10^{-4}$	$2.61 \times 10^{-4}$	$2.60 \times 10^{-4}$	$2.59 \times 10^{-4}$
$^{46}\text{Ca}$	$3.99 \times 10^{-20}$	$8.14 \times 10^{-16}$	$1.79 \times 10^{-12}$	$4.90 \times 10^{-11}$	$5.11 \times 10^{-10}$	$1.13 \times 10^{-9}$	$1.43 \times 10^{-9}$
$^{48}\text{Ca}$	$2.1 \times 10^{-25}$	$1.61 \times 10^{-22}$	$9.58 \times 10^{-18}$	$9.28 \times 10^{-16}$	$6.1 \times 10^{-14}$	$3.6 \times 10^{-13}$	$1.10 \times 10^{-12}$
$^{45}\text{Sc}$	$2.8 \times 10^{-7}$	$2.72 \times 10^{-7}$	$3.35 \times 10^{-7}$	$3.77 \times 10^{-7}$	$4.21 \times 10^{-7}$	$4.18 \times 10^{-7}$	$3.91 \times 10^{-7}$
$^{46}\text{Ti}$	$8.53 \times 10^{-7}$	$1.70 \times 10^{-6}$	$9.45 \times 10^{-6}$	$1.85 \times 10^{-5}$	$3.9 \times 10^{-5}$	$3.61 \times 10^{-5}$	$3.42 \times 10^{-5}$
$^{47}\text{Ti}$	$2.13 \times 10^{-5}$	$2.18 \times 10^{-5}$	$2.24 \times 10^{-5}$	$2.27 \times 10^{-5}$	$2.31 \times 10^{-5}$	$2.33 \times 10^{-5}$	$2.35 \times 10^{-5}$
$^{48}\text{Ti}$	$8.12 \times 10^{-4}$	$7.82 \times 10^{-4}$	$7.37 \times 10^{-4}$	$7.8 \times 10^{-4}$	$6.76 \times 10^{-4}$	$6.58 \times 10^{-4}$	$6.33 \times 10^{-4}$
$^{49}\text{Ti}$	$4.75 \times 10^{-6}$	$1.2 \times 10^{-5}$	$1.30 \times 10^{-5}$	$1.47 \times 10^{-5}$	$1.56 \times 10^{-5}$	$1.66 \times 10^{-5}$	$1.77 \times 10^{-5}$
$^{50}\text{Ti}$	$5.52 \times 10^{-16}$	$1.58 \times 10^{-13}$	$5.96 \times 10^{-11}$	$6.7 \times 10^{-10}$	$2.35 \times 10^{-9}$	$3.70 \times 10^{-9}$	$1.7 \times 10^{-8}$
$^{50}\text{V}$	$1.8 \times 10^{-11}$	$2.22 \times 10^{-11}$	$8.63 \times 10^{-10}$	$3.68 \times 10^{-9}$	$8.7 \times 10^{-9}$	$1.46 \times 10^{-8}$	$4.14 \times 10^{-8}$
$^{51}\text{V}$	$5.15 \times 10^{-5}$	$5.47 \times 10^{-5}$	$6.79 \times 10^{-5}$	$7.62 \times 10^{-5}$	$8.55 \times 10^{-5}$	$9.87 \times 10^{-5}$	$1.21 \times 10^{-4}$
$^{50}\text{Cr}$	$5.56 \times 10^{-6}$	$1.34 \times 10^{-5}$	$6.64 \times 10^{-5}$	$1.41 \times 10^{-4}$	$3.5 \times 10^{-4}$	$4.30 \times 10^{-4}$	$5.91 \times 10^{-4}$
$^{52}\text{Cr}$	$4.11 \times 10^{-3}$	$3.86 \times 10^{-3}$	$3.30 \times 10^{-3}$	$2.94 \times 10^{-3}$	$2.65 \times 10^{-3}$	$2.77 \times 10^{-3}$	$3.68 \times 10^{-3}$
$^{53}\text{Cr}$	$4.72 \times 10^{-5}$	$1.21 \times 10^{-4}$	$1.78 \times 10^{-4}$	$2.14 \times 10^{-4}$	$2.77 \times 10^{-4}$	$3.74 \times 10^{-4}$	$5.67 \times 10^{-4}$
$^{54}\text{Cr}$	$9.21 \times 10^{-10}$	$1.18 \times 10^{-9}$	$1.14 \times 10^{-8}$	$4.40 \times 10^{-8}$	$2.43 \times 10^{-7}$	$8.6 \times 10^{-7}$	$2.68 \times 10^{-6}$
$^{55}\text{Mn}$	$3.9 \times 10^{-4}$	$5.59 \times 10^{-4}$	$1.3 \times 10^{-3}$	$1.32 \times 10^{-3}$	$1.87 \times 10^{-3}$	$3.6 \times 10^{-3}$	$6.30 \times 10^{-3}$
$^{54}\text{Fe}$	$1.10 \times 10^{-4}$	$8.14 \times 10^{-4}$	$4.37 \times 10^{-3}$	$8.69 \times 10^{-3}$	$1.66 \times 10^{-2}$	$2.48 \times 10^{-2}$	$4.79 \times 10^{-2}$
$^{56}\text{Fe}$	$6.43 \times 10^{-1}$	$6.38 \times 10^{-1}$	$6.20 \times 10^{-1}$	$6.0 \times 10^{-1}$	$5.65 \times 10^{-1}$	$5.32 \times 10^{-1}$	$4.67 \times 10^{-1}$
$^{57}\text{Fe}$	$9.74 \times 10^{-3}$	$1.6 \times 10^{-2}$	$1.32 \times 10^{-2}$	$1.60 \times 10^{-2}$	$2.2 \times 10^{-2}$	$2.32 \times 10^{-2}$	$2.62 \times 10^{-2}$
$^{58}\text{Fe}$	$1.70 \times 10^{-9}$	$1.86 \times 10^{-9}$	$5.14 \times 10^{-9}$	$1.36 \times 10^{-8}$	$5.25 \times 10^{-8}$	$1.23 \times 10^{-7}$	$3.1 \times 10^{-7}$
$^{60}\text{Fe}$	$1.39 \times 10^{-23}$	$1.81 \times 10^{-21}$	$7.0 \times 10^{-19}$	$3.4 \times 10^{-18}$	$4.58 \times 10^{-18}$	$2.90 \times 10^{-18}$	$1.5 \times 10^{-17}$
$^{59}\text{Co}$	$6.56 \times 10^{-5}$	$9.1 \times 10^{-5}$	$4.9 \times 10^{-4}$	$5.27 \times 10^{-4}$	$6.33 \times 10^{-4}$	$6.12 \times 10^{-4}$	$5.29 \times 10^{-4}$
$^{58}\text{Ni}$	$9.62 \times 10^{-4}$	$1.18 \times 10^{-3}$	$1.11 \times 10^{-2}$	$2.50 \times 10^{-2}$	$5.35 \times 10^{-2}$	$8.7 \times 10^{-2}$	$1.27 \times 10^{-1}$
$^{60}\text{Ni}$	$7.71 \times 10^{-3}$	$8.14 \times 10^{-3}$	$7.14 \times 10^{-3}$	$6.13 \times 10^{-3}$	$4.50 \times 10^{-3}$	$3.27 \times 10^{-3}$	$1.81 \times 10^{-3}$
$^{61}\text{Ni}$	$2.18 \times 10^{-4}$	$2.33 \times 10^{-4}$	$2.62 \times 10^{-4}$	$2.78 \times 10^{-4}$	$2.79 \times 10^{-4}$	$2.61 \times 10^{-4}$	$2.11 \times 10^{-4}$
$^{62}\text{Ni}$	$8.49 \times 10^{-5}$	$2.15 \times 10^{-4}$	$9.81 \times 10^{-4}$	$1.72 \times 10^{-3}$	$2.72 \times 10^{-3}$	$3.17 \times 10^{-3}$	$3.24 \times 10^{-3}$
$^{64}\text{Ni}$	$4.14 \times 10^{-14}$	$3.79 \times 10^{-14}$	$4.71 \times 10^{-14}$	$4.59 \times 10^{-14}$	$1.80 \times 10^{-11}$	$5.11 \times 10^{-14}$	$7.60 \times 10^{-14}$
$^{63}\text{Cu}$	$1.72 \times 10^{-6}$	$3.69 \times 10^{-6}$	$2.13 \times 10^{-6}$	$2.50 \times 10^{-6}$	$3.23 \times 10^{-6}$	$3.76 \times 10^{-6}$	$4.34 \times 10^{-6}$

**Table 10**  
(Continued)

$Z (Z_{\odot})$	0	0.1	0.5	1	2	3	5
$^{65}\text{Cu}$	$7.54 \times 10^{-6}$	$7.68 \times 10^{-6}$	$7.54 \times 10^{-6}$	$7.61 \times 10^{-6}$	$7.60 \times 10^{-6}$	$7.55 \times 10^{-6}$	$7.25 \times 10^{-6}$
$^{64}\text{Zn}$	$1.44 \times 10^{-4}$	$1.31 \times 10^{-4}$	$3.10 \times 10^{-5}$	$2.70 \times 10^{-5}$	$2.38 \times 10^{-5}$	$2.20 \times 10^{-5}$	$2.0 \times 10^{-5}$
$^{66}\text{Zn}$	$8.34 \times 10^{-6}$	$1.1 \times 10^{-5}$	$1.70 \times 10^{-5}$	$2.41 \times 10^{-5}$	$3.35 \times 10^{-5}$	$3.76 \times 10^{-5}$	$3.80 \times 10^{-5}$
$^{67}\text{Zn}$	$3.40 \times 10^{-7}$	$3.33 \times 10^{-7}$	$3.34 \times 10^{-7}$	$3.41 \times 10^{-7}$	$3.53 \times 10^{-7}$	$3.62 \times 10^{-7}$	$3.71 \times 10^{-7}$
$^{68}\text{Zn}$	$1.4 \times 10^{-6}$	$6.8 \times 10^{-7}$	$3.75 \times 10^{-7}$	$3.71 \times 10^{-7}$	$3.71 \times 10^{-7}$	$3.72 \times 10^{-7}$	$3.87 \times 10^{-7}$
$^{70}\text{Zn}$	$1.62 \times 10^{-18}$	$1.48 \times 10^{-18}$	$1.99 \times 10^{-18}$	$1.97 \times 10^{-18}$	$1.12 \times 10^{-16}$	$1.64 \times 10^{-18}$	$1.62 \times 10^{-18}$

**Note.** Masses are in units of solar mass.

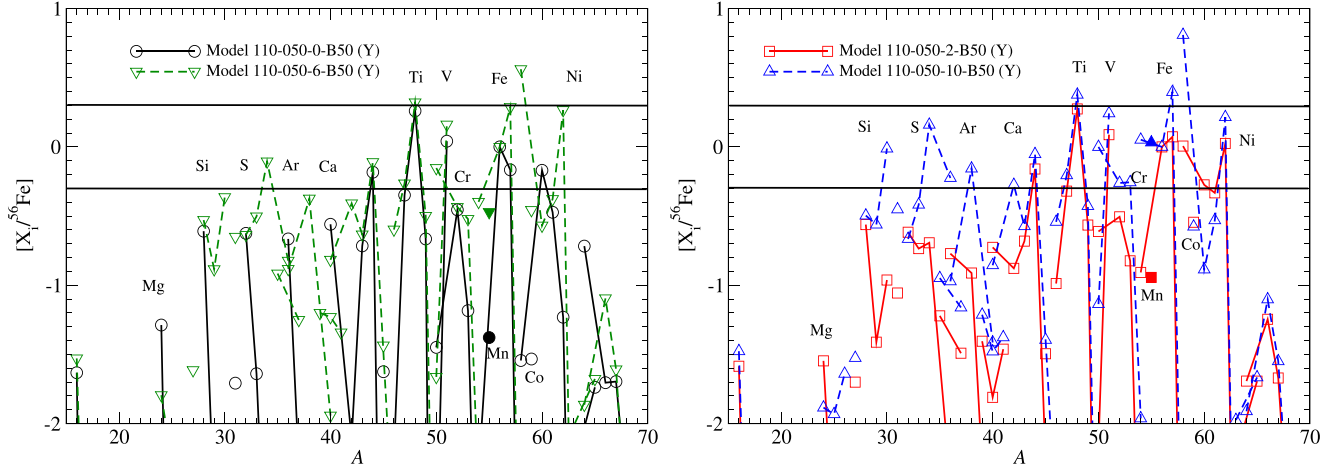


**Figure 19.** Similar to Figure 18, but for Models 110-050-0-B50 (Y) ( $Z = 0$ ) and 110-050-6-B50 (Y) ( $Z = 0.06$ ) in the left panel and Models 110-050-2-B50 (Y) ( $Z = 0.02$ ) and 110-050-10-B50 (Y) ( $Z = 0.10$ ) in the right panel. All models assume  $M = 1.10 M_{\odot}$ ,  $M_{\text{He}} = 0.05 M_{\odot}$ , and a belt-shape initial He detonation at 50 km above the CO-envelope interface.

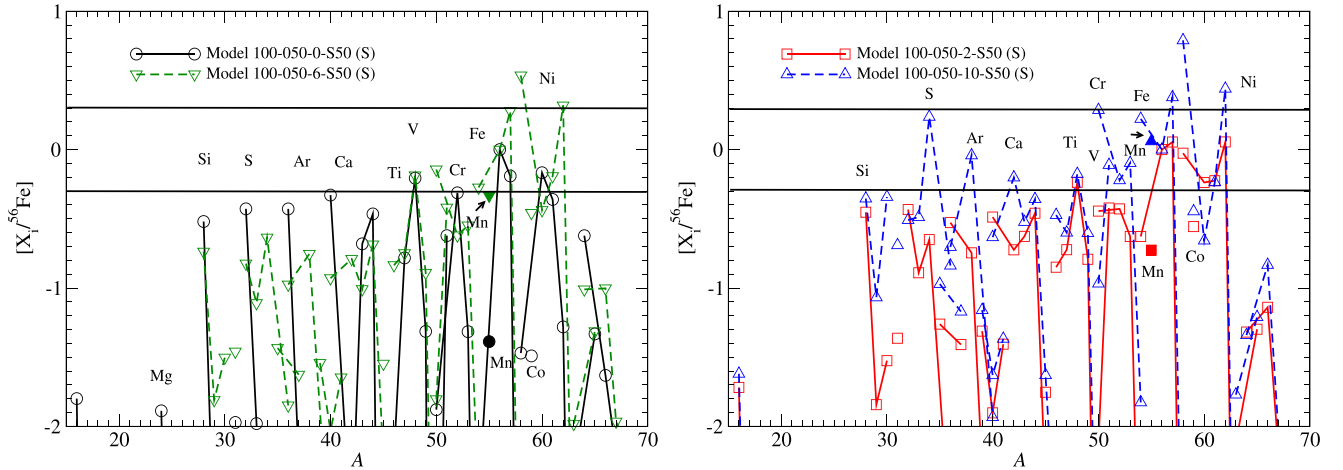


**Figure 20.** Similar to Figure 18, but for Models 110-050-0-S50 (S) ( $Z = 0$ ) and 110-050-6-S50 (S) ( $Z = 0.06$ ) in the left panel and Models 110-050-2-S50 (S) ( $Z = 0.02$ ) and 110-050-10-S50 (S) ( $Z = 0.10$ ) in the right panel. All models assume  $M = 1.10 M_{\odot}$ ,  $M_{\text{He}} = 0.05 M_{\odot}$ , and a spherical initial He detonation at 50 km above the CO-envelope interface.

panel), with the benchmark Chandrasekhar-mass model. We can see that the Chandrasekhar-mass model has its IME closer to the solar value. The Ti and V productions are suppressed compared to the sub-Chandrasekhar-mass model. The Fe and Ni patterns are similar for the two classes of model, except that the  $^{54}\text{Fe}$  and  $^{58}\text{Ni}$  are more enhanced in the Chandrasekhar-mass model. As remarked, the amount of Mn in the sub-Chandrasekhar-mass model is very small to explain the solar

value owing to the differences in electron capture rates. In Model 100-050-2-S50, a similar difference can be observed, except that the overproductions in Ti, V, and Cr become regulated owing to its less massive He envelope.

In Figure 26 we plot the evolution of  $X(^{55}\text{Mn})/X(^{56}\text{Fe})$ , scaled with the solar value, as a function of metallicity  $Z$ . To contrast with the results of the sub-Chandrasekhar-mass model, we also include the benchmark Chandrasekhar-mass model



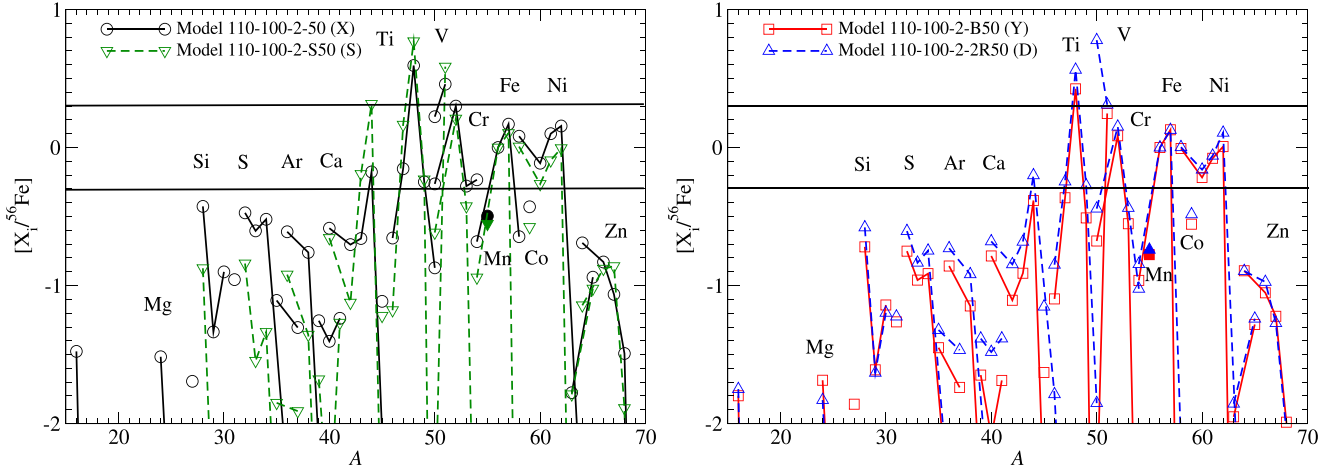


**Figure 21.**  $[X_i/^{56}\text{Fe}]$  for the series of models studying the effects of initial He detonation structure. Similar to Figure 12, but for Models 110-100-2-50 (X) (bubble shape) and 110-100-2-B50 (Y) (belt shape) in the left panel and Models 110-100-2-2R50 (D) (bubble+belt shapes) and 110-100-2-S50 (S) (spherical) in the right panel. All models assume  $M = 1.10 M_\odot$ ,  $M_{\text{He}} = 0.10 M_\odot$ , and  $Z = 0.02$ .

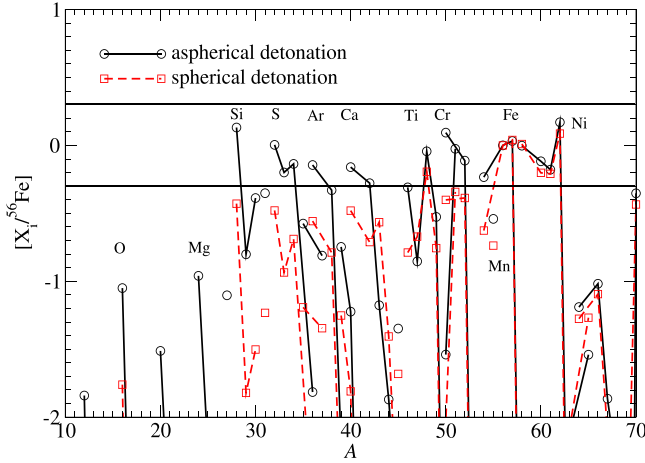


**Figure 22.**  $[X_i/^{56}\text{Fe}]$  for Models 105-050-2-S50 (S) and 110-100-2-50 (X).

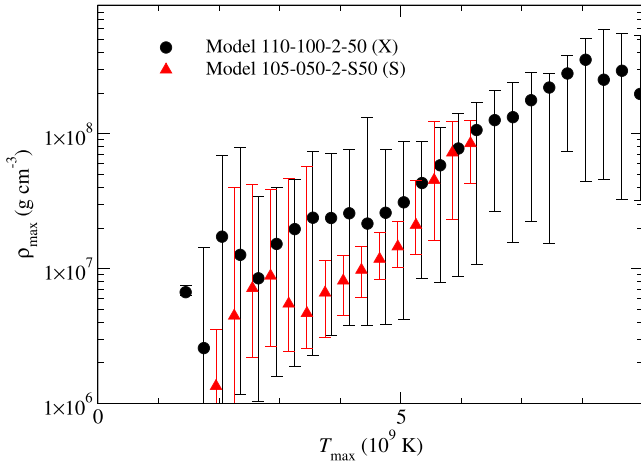


**Figure 23.** Similar to Figure 22, but for  $\rho_{\text{max}}$  against  $T_{\text{max}}$ .

from Leung & Nomoto (2017) and Nomoto & Leung (2017). The stellar abundance from galactic disk F and G dwarfs (Reddy et al. 2003), cluster and field stars (Sobeck et al. 2006),

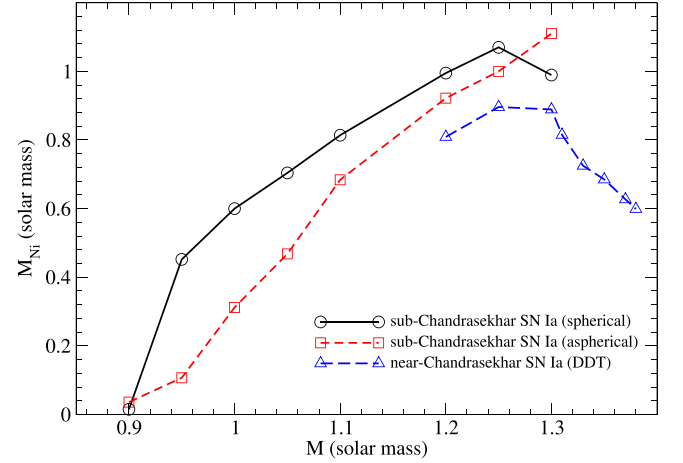


**Figure 24.** Synthesized  $^{56}\text{Ni}$  mass at the end of the simulations against the initial WD mass. Both Chandrasekhar and sub-Chandrasekhar-mass models are included. For sub-Chandrasekhar-mass models, we use Model C-050-2-50 for the aspherical model and Model C-050-2-B50 for the spherical model, where C is the initial mass shown in the figure. The results for sub-Chandrasekhar-mass and Chandrasekhar-mass WDs are selected from this work and from Leung & Nomoto (2017) and Nomoto & Leung (2017).

and stars from thin disks (Feltzing et al. 2007) are included. As expected, at  $Z < -1$  both models do not alter the results since the time delay of SNe Ia mutes the contribution of SNe Ia. After that, the two models deviate. The Chandrasekhar-mass model, which shows a healthy electron capture, provides sufficient  $^{55}\text{Mn}$  to raise the ratio close to the solar value. On the other hand, the sub-Chandrasekhar-mass model produces only 30% of the solar ratio. The prolonged underproduction of  $^{55}\text{Mn}$  makes the ratio even decrease from  $[\text{Fe}/\text{H}] = -0.2$  to 0 to  $\approx 30\%$  of the solar value.

This suggests that even a sub-Chandrasekhar-mass model can provide a variety of models, with ranges of  $^{56}\text{Ni}$  to match observational results of different peak luminosity and with ranges of progenitor mass for different light-curve widths. The Chandrasekhar-mass model contribution to the stellar evolution remains important. The nucleosynthesis suggests that  $^{55}\text{Mn}$  can be partially produced owing to the strong compression heating

**Table 11**  
Similar to Table 10, but for the Radioactive Isotopes

$Z (Z_{\odot})$	0	0.1	0.5	1	2	3	5
$^{22}\text{Na}$	$2.93 \times 10^{-9}$	$3.22 \times 10^{-9}$	$4.6 \times 10^{-9}$	$3.74 \times 10^{-9}$	$2.87 \times 10^{-9}$	$2.42 \times 10^{-9}$	$2.0 \times 10^{-9}$
$^{26}\text{Al}$	$8.57 \times 10^{-7}$	$1.74 \times 10^{-6}$	$2.12 \times 10^{-6}$	$1.70 \times 10^{-6}$	$1.4 \times 10^{-6}$	$7.15 \times 10^{-7}$	$4.1 \times 10^{-7}$
$^{39}\text{Ar}$	$4.11 \times 10^{-13}$	$1.11 \times 10^{-10}$	$1.66 \times 10^{-9}$	$7.27 \times 10^{-9}$	$3.3 \times 10^{-8}$	$5.13 \times 10^{-8}$	$5.39 \times 10^{-8}$
$^{40}\text{K}$	$4.83 \times 10^{-11}$	$1.59 \times 10^{-9}$	$1.22 \times 10^{-8}$	$3.86 \times 10^{-8}$	$8.64 \times 10^{-8}$	$9.6 \times 10^{-8}$	$5.63 \times 10^{-8}$
$^{41}\text{Ca}$	$6.17 \times 10^{-7}$	$2.38 \times 10^{-6}$	$4.36 \times 10^{-6}$	$5.66 \times 10^{-6}$	$6.62 \times 10^{-6}$	$6.34 \times 10^{-6}$	$4.76 \times 10^{-6}$
$^{44}\text{Ti}$	$2.70 \times 10^{-4}$	$2.68 \times 10^{-4}$	$2.66 \times 10^{-4}$	$2.64 \times 10^{-4}$	$2.62 \times 10^{-4}$	$2.61 \times 10^{-4}$	$2.59 \times 10^{-4}$
$^{48}\text{V}$	$1.45 \times 10^{-7}$	$1.47 \times 10^{-7}$	$1.70 \times 10^{-7}$	$1.96 \times 10^{-7}$	$2.34 \times 10^{-7}$	$2.49 \times 10^{-7}$	$2.36 \times 10^{-7}$
$^{49}\text{V}$	$8.72 \times 10^{-9}$	$1.18 \times 10^{-8}$	$6.3 \times 10^{-8}$	$1.54 \times 10^{-7}$	$3.54 \times 10^{-7}$	$6.54 \times 10^{-7}$	$1.31 \times 10^{-6}$
$^{53}\text{Mn}$	$3.8 \times 10^{-7}$	$4.27 \times 10^{-7}$	$2.73 \times 10^{-6}$	$9.5 \times 10^{-6}$	$4.91 \times 10^{-5}$	$1.22 \times 10^{-4}$	$2.50 \times 10^{-4}$
$^{60}\text{Fe}$	$2.23 \times 10^{-22}$	$2.90 \times 10^{-20}$	$1.14 \times 10^{-17}$	$4.59 \times 10^{-17}$	$6.65 \times 10^{-17}$	$4.22 \times 10^{-17}$	$1.48 \times 10^{-16}$
$^{56}\text{Co}$	$5.62 \times 10^{-6}$	$5.89 \times 10^{-6}$	$7.25 \times 10^{-6}$	$8.93 \times 10^{-6}$	$1.21 \times 10^{-5}$	$1.85 \times 10^{-5}$	$4.20 \times 10^{-5}$
$^{57}\text{Co}$	$1.10 \times 10^{-6}$	$1.23 \times 10^{-6}$	$2.61 \times 10^{-6}$	$5.62 \times 10^{-6}$	$1.86 \times 10^{-5}$	$3.17 \times 10^{-5}$	$5.16 \times 10^{-5}$
$^{60}\text{Co}$	$2.31 \times 10^{-15}$	$7.99 \times 10^{-15}$	$6.58 \times 10^{-14}$	$1.17 \times 10^{-13}$	$5.39 \times 10^{-13}$	$1.67 \times 10^{-12}$	$7.29 \times 10^{-12}$
$^{56}\text{Ni}$	$6.42 \times 10^{-1}$	$6.38 \times 10^{-1}$	$6.20 \times 10^{-1}$	$6.0 \times 10^{-1}$	$5.64 \times 10^{-1}$	$5.31 \times 10^{-1}$	$4.64 \times 10^{-1}$
$^{57}\text{Ni}$	$9.74 \times 10^{-3}$	$1.6 \times 10^{-2}$	$1.32 \times 10^{-2}$	$1.60 \times 10^{-2}$	$2.2 \times 10^{-2}$	$2.31 \times 10^{-2}$	$2.62 \times 10^{-2}$
$^{59}\text{Ni}$	$1.59 \times 10^{-6}$	$1.61 \times 10^{-6}$	$2.5 \times 10^{-6}$	$2.89 \times 10^{-6}$	$6.89 \times 10^{-6}$	$1.61 \times 10^{-5}$	$4.48 \times 10^{-5}$
$^{63}\text{Ni}$	$5.94 \times 10^{-16}$	$9.34 \times 10^{-16}$	$3.30 \times 10^{-15}$	$2.12 \times 10^{-15}$	$4.10 \times 10^{-13}$	$1.92 \times 10^{-14}$	$9.76 \times 10^{-14}$

**Note.** Masses are in units of solar mass.

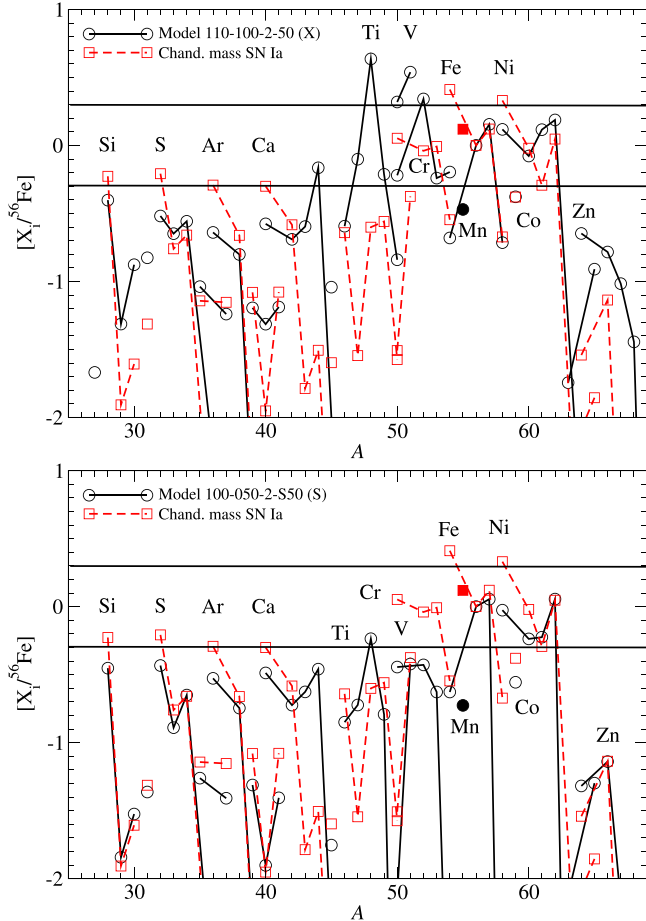


**Figure 25.**  $[X_i/^{56}\text{Fe}]$  for the benchmark Model 110-100-2-50 (X) (top panel) and Model 100-050-2-S50 (S) (lower panel).

of the matter inside the star. The related mass is far from enough to explain the growth of  $^{55}\text{Mn}$  especially from  $\log_{10}Z = -0.2$  to 0.

For further application of our sub-Chandrasekhar SN Ia yield in the context of GCE, we also present in Tables 12–17, the mass

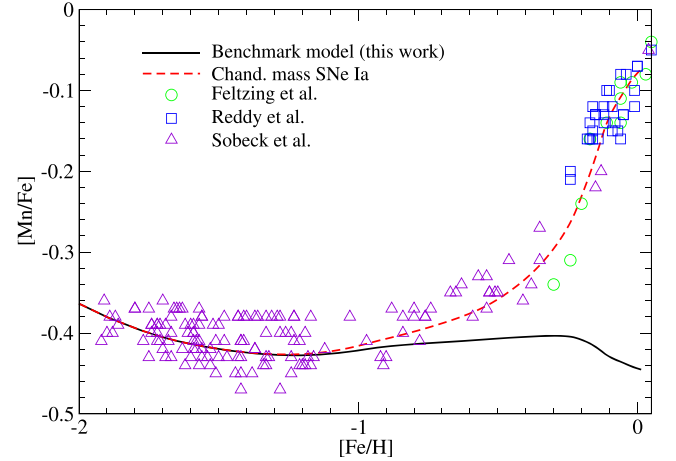


**Figure 26.**  $[^{55}\text{Mn}/X(^{56}\text{Fe})]$  against  $[\text{Fe}/\text{H}]$  for the benchmark model 110-100-2-50 (X) and the typical Chandrasekhar-mass SNe Ia (Leung & Nomoto 2018).

abundance of our representative SN Ia models with the minimum  $M_{\text{He}}$  necessary for triggering the second detonation based on Models 110-100-2-50 (X), 110-050-2-50 (Y), and 100-050-2-S50 (S), respectively. Metallicity is obviously an important factor that contributes to  $^{56}\text{Ni}$  production and also the production of high neutron ratio isotopes.  $M_{\text{He}}$  determines the minimum mass above which the C detonation can be triggered in our aspherical detonation models.  $M_{\text{Ni}}$  is the primary indicator of the explosion strength as derived from the light curves.

It can be seen that, from the observational point of view, the sub-Chandrasekhar-mass SNe Ia produce radioactive isotopes qualitatively different from the conventional Chandrasekhar-mass SNe Ia. Due to the He envelope burning,  $\alpha$ -chain elements are more pronounced. Among those,  $^{44}\text{Ti}$  is produced, which has a half-life of  $\approx 60$  yr by electron capture to form  $^{44}\text{Sc}$ .

A typical amount of  $\sim 10^{-3} M_{\odot}$  is found. Their abundance decreases when the  $^{56}\text{Ni}$  production increases. The detection of the decay of  $^{44}\text{Ti}$  as a long-term energy of an SN Ia remnant may give very stringent constraints on the progenitor type of SNe Ia.

**Table 12**  
Nucleosynthesis Yields for Stable Isotopes from the Models Using One He Detonation Bubble as the Initial Configuration

$M$	0.90	0.95	1.00	1.05	1.10	1.15	1.20
$M_{\text{He}}$	0.15	0.15	0.10	0.10	0.10	0.10	0.05
$^{12}\text{C}$	$1.78 \times 10^{-2}$	$7.5 \times 10^{-3}$	$8.85 \times 10^{-3}$	$1.26 \times 10^{-2}$	$3.35 \times 10^{-3}$	$1.6 \times 10^{-4}$	$2.10 \times 10^{-3}$
$^{13}\text{C}$	$6.99 \times 10^{-8}$	$2.73 \times 10^{-9}$	$3.87 \times 10^{-9}$	$1.84 \times 10^{-8}$	$1.25 \times 10^{-9}$	$4.83 \times 10^{-11}$	$5.8 \times 10^{-10}$
$^{14}\text{N}$	$1.50 \times 10^{-6}$	$7.88 \times 10^{-8}$	$9.0 \times 10^{-8}$	$4.92 \times 10^{-7}$	$3.80 \times 10^{-8}$	$8.42 \times 10^{-10}$	$1.41 \times 10^{-8}$
$^{15}\text{N}$	$8.65 \times 10^{-9}$	$1.83 \times 10^{-9}$	$2.69 \times 10^{-9}$	$3.45 \times 10^{-9}$	$1.8 \times 10^{-9}$	$1.13 \times 10^{-10}$	$7.37 \times 10^{-10}$
$^{16}\text{O}$	$2.63 \times 10^{-1}$	$2.19 \times 10^{-1}$	$2.35 \times 10^{-1}$	$1.85 \times 10^{-1}$	$1.17 \times 10^{-1}$	$5.23 \times 10^{-2}$	$6.54 \times 10^{-2}$
$^{17}\text{O}$	$3.23 \times 10^{-7}$	$4.35 \times 10^{-8}$	$4.80 \times 10^{-8}$	$1.68 \times 10^{-7}$	$2.8 \times 10^{-8}$	$2.95 \times 10^{-10}$	$7.14 \times 10^{-9}$
$^{18}\text{O}$	$4.35 \times 10^{-9}$	$5.86 \times 10^{-10}$	$6.10 \times 10^{-10}$	$1.89 \times 10^{-9}$	$3.4 \times 10^{-10}$	$6.56 \times 10^{-12}$	$1.29 \times 10^{-10}$
$^{19}\text{F}$	$4.10 \times 10^{-10}$	$6.42 \times 10^{-11}$	$8.49 \times 10^{-11}$	$1.79 \times 10^{-10}$	$3.28 \times 10^{-11}$	$1.94 \times 10^{-12}$	$1.80 \times 10^{-11}$
$^{20}\text{Ne}$	$2.65 \times 10^{-2}$	$8.46 \times 10^{-3}$	$1.4 \times 10^{-2}$	$9.19 \times 10^{-3}$	$4.0 \times 10^{-3}$	$6.90 \times 10^{-4}$	$2.91 \times 10^{-3}$
$^{21}\text{Ne}$	$2.48 \times 10^{-6}$	$4.54 \times 10^{-7}$	$5.79 \times 10^{-7}$	$1.3 \times 10^{-6}$	$2.17 \times 10^{-7}$	$2.1 \times 10^{-8}$	$1.32 \times 10^{-7}$
$^{22}\text{Ne}$	$3.40 \times 10^{-4}$	$2.0 \times 10^{-4}$	$2.42 \times 10^{-4}$	$3.53 \times 10^{-4}$	$9.45 \times 10^{-5}$	$2.66 \times 10^{-9}$	$5.62 \times 10^{-5}$
$^{23}\text{Na}$	$1.18 \times 10^{-4}$	$3.13 \times 10^{-5}$	$4.7 \times 10^{-5}$	$4.36 \times 10^{-5}$	$1.47 \times 10^{-5}$	$2.20 \times 10^{-6}$	$1.8 \times 10^{-5}$
$^{24}\text{Mg}$	$3.7 \times 10^{-2}$	$2.15 \times 10^{-2}$	$2.38 \times 10^{-2}$	$1.62 \times 10^{-2}$	$8.26 \times 10^{-3}$	$3.32 \times 10^{-3}$	$4.97 \times 10^{-3}$
$^{25}\text{Mg}$	$2.63 \times 10^{-4}$	$7.96 \times 10^{-5}$	$1.2 \times 10^{-4}$	$1.1 \times 10^{-4}$	$3.89 \times 10^{-5}$	$7.71 \times 10^{-6}$	$2.51 \times 10^{-5}$
$^{26}\text{Mg}$	$3.97 \times 10^{-4}$	$1.20 \times 10^{-4}$	$1.47 \times 10^{-4}$	$1.59 \times 10^{-4}$	$5.60 \times 10^{-5}$	$9.35 \times 10^{-6}$	$3.69 \times 10^{-5}$
$^{26}\text{Al}$	$7.61 \times 10^{-9}$	$2.47 \times 10^{-29}$	$3.75 \times 10^{-28}$	$2.73 \times 10^{-29}$	$2.86 \times 10^{-29}$	$2.99 \times 10^{-29}$	$4.48 \times 10^{-28}$
$^{27}\text{Al}$	$2.67 \times 10^{-3}$	$1.68 \times 10^{-3}$	$1.95 \times 10^{-3}$	$1.30 \times 10^{-3}$	$6.50 \times 10^{-4}$	$2.53 \times 10^{-4}$	$3.93 \times 10^{-4}$
$^{28}\text{Si}$	$1.90 \times 10^{-1}$	$1.43 \times 10^{-1}$	$1.53 \times 10^{-1}$	$1.27 \times 10^{-1}$	$1.35 \times 10^{-1}$	$9.51 \times 10^{-2}$	$9.20 \times 10^{-2}$
$^{29}\text{Si}$	$2.83 \times 10^{-3}$	$1.87 \times 10^{-3}$	$2.9 \times 10^{-3}$	$1.61 \times 10^{-3}$	$8.76 \times 10^{-4}$	$3.44 \times 10^{-4}$	$5.18 \times 10^{-4}$
$^{30}\text{Si}$	$4.62 \times 10^{-3}$	$4.1 \times 10^{-3}$	$4.36 \times 10^{-3}$	$3.0 \times 10^{-3}$	$1.62 \times 10^{-3}$	$6.99 \times 10^{-4}$	$9.30 \times 10^{-4}$
$^{31}\text{P}$	$9.82 \times 10^{-4}$	$7.65 \times 10^{-4}$	$8.70 \times 10^{-4}$	$6.18 \times 10^{-4}$	$3.97 \times 10^{-4}$	$1.78 \times 10^{-4}$	$2.23 \times 10^{-4}$
$^{32}\text{S}$	$7.66 \times 10^{-2}$	$5.15 \times 10^{-2}$	$5.63 \times 10^{-2}$	$4.93 \times 10^{-2}$	$6.8 \times 10^{-2}$	$4.57 \times 10^{-2}$	$4.25 \times 10^{-2}$
$^{33}\text{S}$	$7.26 \times 10^{-4}$	$6.22 \times 10^{-4}$	$6.84 \times 10^{-4}$	$5.4 \times 10^{-4}$	$3.72 \times 10^{-4}$	$1.82 \times 10^{-4}$	$2.15 \times 10^{-4}$
$^{34}\text{S}$	$3.49 \times 10^{-3}$	$3.43 \times 10^{-3}$	$3.42 \times 10^{-3}$	$3.7 \times 10^{-3}$	$2.62 \times 10^{-3}$	$1.34 \times 10^{-3}$	$1.43 \times 10^{-3}$
$^{36}\text{S}$	$5.53 \times 10^{-7}$	$4.52 \times 10^{-7}$	$5.1 \times 10^{-7}$	$3.46 \times 10^{-7}$	$1.77 \times 10^{-7}$	$6.99 \times 10^{-8}$	$1.5 \times 10^{-7}$
$^{35}\text{Cl}$	$3.69 \times 10^{-4}$	$1.64 \times 10^{-4}$	$1.92 \times 10^{-4}$	$1.42 \times 10^{-4}$	$1.51 \times 10^{-4}$	$7.4 \times 10^{-5}$	$8.76 \times 10^{-5}$
$^{37}\text{Cl}$	$4.17 \times 10^{-5}$	$2.85 \times 10^{-5}$	$3.16 \times 10^{-5}$	$2.41 \times 10^{-5}$	$3.26 \times 10^{-5}$	$1.95 \times 10^{-5}$	$1.98 \times 10^{-5}$
$^{36}\text{Ar}$	$1.7 \times 10^{-2}$	$6.82 \times 10^{-3}$	$7.39 \times 10^{-3}$	$7.10 \times 10^{-3}$	$9.73 \times 10^{-3}$	$7.81 \times 10^{-3}$	$6.95 \times 10^{-3}$
$^{38}\text{Ar}$	$1.70 \times 10^{-3}$	$1.6 \times 10^{-3}$	$1.13 \times 10^{-3}$	$9.58 \times 10^{-4}$	$1.32 \times 10^{-3}$	$7.79 \times 10^{-4}$	$7.89 \times 10^{-4}$
$^{40}\text{Ar}$	$9.42 \times 10^{-9}$	$6.9 \times 10^{-9}$	$7.36 \times 10^{-9}$	$4.63 \times 10^{-9}$	$3.35 \times 10^{-9}$	$1.3 \times 10^{-9}$	$1.60 \times 10^{-9}$
$^{39}\text{K}$	$1.46 \times 10^{-4}$	$8.23 \times 10^{-5}$	$9.61 \times 10^{-5}$	$6.56 \times 10^{-5}$	$1.7 \times 10^{-4}$	$7.4 \times 10^{-5}$	$6.75 \times 10^{-5}$
$^{40}\text{K}$	$1.72 \times 10^{-7}$	$6.69 \times 10^{-8}$	$9.10 \times 10^{-8}$	$5.43 \times 10^{-8}$	$1.23 \times 10^{-7}$	$2.30 \times 10^{-8}$	$2.92 \times 10^{-8}$
$^{41}\text{K}$	$1.0 \times 10^{-5}$	$6.10 \times 10^{-6}$	$6.97 \times 10^{-6}$	$5.23 \times 10^{-6}$	$8.47 \times 10^{-6}$	$5.44 \times 10^{-6}$	$5.4 \times 10^{-6}$
$^{40}\text{Ca}$	$9.56 \times 10^{-3}$	$6.91 \times 10^{-3}$	$7.39 \times 10^{-3}$	$6.71 \times 10^{-3}$	$8.49 \times 10^{-3}$	$7.38 \times 10^{-3}$	$6.36 \times 10^{-3}$
$^{42}\text{Ca}$	$5.98 \times 10^{-5}$	$3.53 \times 10^{-5}$	$3.97 \times 10^{-5}$	$3.7 \times 10^{-5}$	$4.53 \times 10^{-5}$	$2.70 \times 10^{-5}$	$2.76 \times 10^{-5}$
$^{43}\text{Ca}$	$2.32 \times 10^{-5}$	$2.29 \times 10^{-5}$	$2.66 \times 10^{-5}$	$1.55 \times 10^{-5}$	$1.30 \times 10^{-5}$	$1.18 \times 10^{-5}$	$1.22 \times 10^{-5}$
$^{44}\text{Ca}$	$1.0 \times 10^{-3}$	$1.4 \times 10^{-3}$	$1.15 \times 10^{-3}$	$6.58 \times 10^{-4}$	$5.14 \times 10^{-4}$	$3.69 \times 10^{-4}$	$5.11 \times 10^{-4}$
$^{46}\text{Ca}$	$1.75 \times 10^{-10}$	$1.59 \times 10^{-10}$	$1.75 \times 10^{-10}$	$1.15 \times 10^{-10}$	$1.78 \times 10^{-10}$	$2.52 \times 10^{-11}$	$3.70 \times 10^{-11}$
$^{48}\text{Ca}$	$1.46 \times 10^{-15}$	$7.77 \times 10^{-16}$	$9.33 \times 10^{-16}$	$5.85 \times 10^{-16}$	$9.31 \times 10^{-12}$	$1.11 \times 10^{-16}$	$2.31 \times 10^{-16}$
$^{45}\text{Sc}$	$1.57 \times 10^{-6}$	$1.33 \times 10^{-6}$	$1.45 \times 10^{-6}$	$1.2 \times 10^{-6}$	$1.67 \times 10^{-6}$	$1.59 \times 10^{-6}$	$5.84 \times 10^{-7}$
$^{46}\text{Ti}$	$3.44 \times 10^{-5}$	$1.68 \times 10^{-5}$	$1.95 \times 10^{-5}$	$1.62 \times 10^{-5}$	$2.94 \times 10^{-5}$	$1.87 \times 10^{-5}$	$1.43 \times 10^{-5}$
$^{47}\text{Ti}$	$1.71 \times 10^{-4}$	$1.77 \times 10^{-4}$	$1.79 \times 10^{-4}$	$1.19 \times 10^{-4}$	$8.61 \times 10^{-5}$	$5.44 \times 10^{-5}$	$7.61 \times 10^{-5}$
$^{48}\text{Ti}$	$9.25 \times 10^{-3}$	$9.96 \times 10^{-3}$	$8.99 \times 10^{-3}$	$7.46 \times 10^{-3}$	$4.87 \times 10^{-3}$	$5.11 \times 10^{-3}$	$3.34 \times 10^{-3}$
$^{49}\text{Ti}$	$6.71 \times 10^{-5}$	$6.60 \times 10^{-5}$	$6.67 \times 10^{-5}$	$5.42 \times 10^{-5}$	$5.24 \times 10^{-5}$	$6.48 \times 10^{-5}$	$2.46 \times 10^{-5}$
$^{50}\text{Ti}$	$1.16 \times 10^{-9}$	$1.53 \times 10^{-9}$	$1.55 \times 10^{-9}$	$1.46 \times 10^{-9}$	$1.22 \times 10^{-5}$	$4.28 \times 10^{-10}$	$4.71 \times 10^{-10}$
$^{50}\text{V}$	$6.12 \times 10^{-9}$	$7.11 \times 10^{-9}$	$6.77 \times 10^{-9}$	$6.7 \times 10^{-9}$	$8.42 \times 10^{-7}$	$1.62 \times 10^{-8}$	$2.39 \times 10^{-9}$
$^{51}\text{V}$	$1.5 \times 10^{-3}$	$1.1 \times 10^{-3}$	$9.89 \times 10^{-4}$	$7.96 \times 10^{-4}$	$5.89 \times 10^{-4}$	$3.84 \times 10^{-4}$	$3.74 \times 10^{-4}$
$^{50}\text{Cr}$	$2.8 \times 10^{-4}$	$1.29 \times 10^{-4}$	$1.35 \times 10^{-4}$	$1.25 \times 10^{-4}$	$2.18 \times 10^{-4}$	$1.83 \times 10^{-4}$	$1.20 \times 10^{-4}$
$^{52}\text{Cr}$	$1.36 \times 10^{-2}$	$1.74 \times 10^{-2}$	$1.6 \times 10^{-2}$	$1.67 \times 10^{-2}$	$1.60 \times 10^{-2}$	$1.24 \times 10^{-2}$	$8.18 \times 10^{-3}$
$^{53}\text{Cr}$	$4.36 \times 10^{-4}$	$3.84 \times 10^{-4}$	$3.40 \times 10^{-4}$	$3.76 \times 10^{-4}$	$4.87 \times 10^{-4}$	$4.52 \times 10^{-4}$	$2.42 \times 10^{-4}$
$^{54}\text{Cr}$	$5.24 \times 10^{-8}$	$9.91 \times 10^{-8}$	$4.6 \times 10^{-8}$	$2.79 \times 10^{-8}$	$1.37 \times 10^{-4}$	$5.88 \times 10^{-7}$	$3.12 \times 10^{-8}$
$^{55}\text{Mn}$	$1.96 \times 10^{-3}$	$1.78 \times 10^{-3}$	$1.59 \times 10^{-3}$	$2.11 \times 10^{-3}$	$2.28 \times 10^{-3}$	$2.16 \times 10^{-3}$	$2.85 \times 10^{-3}$
$^{54}\text{Fe}$	$6.59 \times 10^{-3}$	$4.18 \times 10^{-3}$	$4.55 \times 10^{-3}$	$4.65 \times 10^{-3}$	$7.80 \times 10^{-3}$	$6.52 \times 10^{-3}$	$1.17 \times 10^{-2}$
$^{56}\text{Fe}$	$1.39 \times 10^{-1}$	$3.17 \times 10^{-1}$	$3.52 \times 10^{-1}$	$4.93 \times 10^{-1}$	$6.10 \times 10^{-1}$	$7.97 \times 10^{-1}$	$8.26 \times 10^{-1}$
$^{57}\text{Fe}$	$6.32 \times 10^{-3}$	$1.11 \times 10^{-2}$	$1.13 \times 10^{-2}$	$1.64 \times 10^{-2}$	$2.12 \times 10^{-2}$	$2.65 \times 10^{-2}$	$2.72 \times 10^{-2}$
$^{58}\text{Fe}$	$1.71 \times 10^{-8}$	$6.75 \times 10^{-8}$	$1.9 \times 10^{-8}$	$7.29 \times 10^{-9}$	$4.39 \times 10^{-4}$	$5.86 \times 10^{-7}$	$9.43 \times 10^{-9}$
$^{60}\text{Fe}$	$1.45 \times 10^{-18}$	$9.5 \times 10^{-19}$	$6.46 \times 10^{-19}$	$4.59 \times 10^{-19}$	$1.34 \times 10^{-9}$	$2.17 \times 10^{-17}$	$3.13 \times 10^{-19}$
$^{59}\text{Co}$	$2.47 \times 10^{-4}$	$3.44 \times 10^{-4}$	$3.94 \times 10^{-4}$	$5.34 \times 10^{-4}$	$7.19 \times 10^{-4}$	$8.1 \times 10^{-4}$	$6.90 \times 10^{-4}$
$^{58}\text{Ni}$	$5.8 \times 10^{-3}$	$1.27 \times 10^{-2}$	$1.49 \times 10^{-2}$	$2.21 \times 10^{-2}$	$3.26 \times 10^{-2}$	$3.87 \times 10^{-2}$	$5.43 \times 10^{-2}$
$^{60}\text{Ni}$	$3.63 \times 10^{-3}$	$6.2 \times 10^{-3}$	$5.57 \times 10^{-3}$	$8.12 \times 10^{-3}$	$8.28 \times 10^{-3}$	$9.20 \times 10^{-3}$	$6.92 \times 10^{-3}$
$^{61}\text{Ni}$	$4.35 \times 10^{-4}$	$4.71 \times 10^{-4}$	$3.71 \times 10^{-4}$	$6.39 \times 10^{-4}$	$5.99 \times 10^{-4}$	$5.77 \times 10^{-4}$	$4.46 \times 10^{-4}$
$^{62}\text{Ni}$	$6.55 \times 10^{-4}$	$1.46 \times 10^{-3}$	$1.42 \times 10^{-3}$	$2.6 \times 10^{-3}$	$2.20 \times 10^{-3}$	$2.40 \times 10^{-3}$	$1.96 \times 10^{-3}$
$^{64}\text{Ni}$	$9.49 \times 10^{-11}$	$2.80 \times 10^{-12}$	$4.49 \times 10^{-11}$	$1.50 \times 10^{-12}$	$6.96 \times 10^{-7}$	$1.22 \times 10^{-10}$	$3.1 \times 10^{-11}$

**Table 12**  
(Continued)

$M$	0.90	0.95	1.00	1.05	1.10	1.15	1.20
$^{63}\text{Cu}$	$7.58 \times 10^{-6}$	$6.93 \times 10^{-6}$	$6.10 \times 10^{-6}$	$6.60 \times 10^{-6}$	$5.59 \times 10^{-6}$	$3.84 \times 10^{-6}$	$3.75 \times 10^{-6}$
$^{65}\text{Cu}$	$2.21 \times 10^{-5}$	$2.6 \times 10^{-5}$	$1.68 \times 10^{-5}$	$2.59 \times 10^{-5}$	$1.76 \times 10^{-5}$	$1.27 \times 10^{-5}$	$1.39 \times 10^{-5}$
$^{64}\text{Zn}$	$1.6 \times 10^{-4}$	$1.3 \times 10^{-4}$	$7.2 \times 10^{-5}$	$1.46 \times 10^{-4}$	$1.16 \times 10^{-4}$	$8.74 \times 10^{-5}$	$7.18 \times 10^{-5}$
$^{66}\text{Zn}$	$4.63 \times 10^{-5}$	$6.76 \times 10^{-5}$	$5.21 \times 10^{-5}$	$7.15 \times 10^{-5}$	$5.2 \times 10^{-5}$	$4.32 \times 10^{-5}$	$4.23 \times 10^{-5}$
$^{67}\text{Zn}$	$7.95 \times 10^{-6}$	$7.76 \times 10^{-6}$	$6.11 \times 10^{-6}$	$6.29 \times 10^{-6}$	$4.36 \times 10^{-6}$	$2.63 \times 10^{-6}$	$3.7 \times 10^{-6}$
$^{68}\text{Zn}$	$4.15 \times 10^{-6}$	$4.56 \times 10^{-6}$	$3.34 \times 10^{-6}$	$1.5 \times 10^{-5}$	$7.56 \times 10^{-6}$	$3.93 \times 10^{-6}$	$3.27 \times 10^{-6}$
$^{70}\text{Zn}$	$4.40 \times 10^{-15}$	$6.16 \times 10^{-17}$	$3.36 \times 10^{-11}$	$5.53 \times 10^{-17}$	$1.10 \times 10^{-13}$	$2.26 \times 10^{-14}$	$2.28 \times 10^{-16}$

**Note.** The minimum He envelope mass is used for each choice of progenitor mass. All models are of solar metallicity, and masses are in units of solar mass.

**Table 13**  
Similar to Table 12, but for the Radioactive Isotopes of the Selected Models after Explosion

$M$	0.90	0.95	1.00	1.05	1.10	1.15	1.20
$M_{\text{He}}$	0.15	0.15	0.10	0.10	0.10	0.10	0.05
$^{22}\text{Na}$	$8.72 \times 10^{-8}$	$2.71 \times 10^{-8}$	$3.50 \times 10^{-8}$	$3.2 \times 10^{-8}$	$1.25 \times 10^{-8}$	$2.0 \times 10^{-9}$	$9.56 \times 10^{-9}$
$^{26}\text{Al}$	$4.50 \times 10^{-5}$	$1.46 \times 10^{-5}$	$1.72 \times 10^{-5}$	$1.49 \times 10^{-5}$	$6.98 \times 10^{-6}$	$1.50 \times 10^{-6}$	$4.78 \times 10^{-6}$
$^{39}\text{Ar}$	$2.90 \times 10^{-8}$	$1.20 \times 10^{-8}$	$1.35 \times 10^{-8}$	$9.97 \times 10^{-9}$	$1.99 \times 10^{-8}$	$2.96 \times 10^{-9}$	$4.99 \times 10^{-9}$
$^{40}\text{K}$	$1.73 \times 10^{-7}$	$6.72 \times 10^{-8}$	$9.15 \times 10^{-8}$	$5.46 \times 10^{-8}$	$1.23 \times 10^{-7}$	$2.31 \times 10^{-8}$	$2.94 \times 10^{-8}$
$^{41}\text{Ca}$	$9.96 \times 10^{-6}$	$6.19 \times 10^{-6}$	$7.5 \times 10^{-6}$	$5.27 \times 10^{-6}$	$8.49 \times 10^{-6}$	$5.46 \times 10^{-6}$	$5.8 \times 10^{-6}$
$^{44}\text{Ti}$	$1.0 \times 10^{-3}$	$1.4 \times 10^{-3}$	$1.14 \times 10^{-3}$	$6.58 \times 10^{-4}$	$5.14 \times 10^{-4}$	$3.69 \times 10^{-4}$	$5.11 \times 10^{-4}$
$^{48}\text{V}$	$2.50 \times 10^{-6}$	$2.21 \times 10^{-6}$	$2.59 \times 10^{-6}$	$1.16 \times 10^{-6}$	$3.26 \times 10^{-6}$	$1.7 \times 10^{-6}$	$7.73 \times 10^{-7}$
$^{49}\text{V}$	$2.43 \times 10^{-7}$	$2.7 \times 10^{-7}$	$2.6 \times 10^{-7}$	$1.58 \times 10^{-7}$	$5.19 \times 10^{-6}$	$5.53 \times 10^{-7}$	$1.7 \times 10^{-7}$
$^{53}\text{Mn}$	$1.28 \times 10^{-5}$	$1.30 \times 10^{-5}$	$9.54 \times 10^{-6}$	$5.48 \times 10^{-6}$	$1.6 \times 10^{-4}$	$3.34 \times 10^{-5}$	$7.11 \times 10^{-6}$
$^{60}\text{Fe}$	$2.4 \times 10^{-17}$	$1.32 \times 10^{-17}$	$9.26 \times 10^{-18}$	$6.74 \times 10^{-18}$	$2.1 \times 10^{-8}$	$3.25 \times 10^{-16}$	$4.49 \times 10^{-18}$
$^{56}\text{Co}$	$1.10 \times 10^{-5}$	$1.4 \times 10^{-5}$	$5.8 \times 10^{-6}$	$4.41 \times 10^{-6}$	$8.95 \times 10^{-5}$	$9.86 \times 10^{-5}$	$1.45 \times 10^{-5}$
$^{57}\text{Co}$	$8.35 \times 10^{-6}$	$1.4 \times 10^{-5}$	$4.83 \times 10^{-6}$	$2.85 \times 10^{-6}$	$1.47 \times 10^{-4}$	$4.7 \times 10^{-5}$	$6.10 \times 10^{-6}$
$^{60}\text{Co}$	$1.19 \times 10^{-13}$	$1.71 \times 10^{-12}$	$9.14 \times 10^{-14}$	$8.67 \times 10^{-14}$	$8.90 \times 10^{-8}$	$4.87 \times 10^{-11}$	$7.92 \times 10^{-14}$
$^{56}\text{Ni}$	$1.38 \times 10^{-1}$	$3.17 \times 10^{-1}$	$3.52 \times 10^{-1}$	$4.93 \times 10^{-1}$	$6.8 \times 10^{-1}$	$7.96 \times 10^{-1}$	$8.26 \times 10^{-1}$
$^{57}\text{Ni}$	$6.31 \times 10^{-3}$	$1.11 \times 10^{-2}$	$1.13 \times 10^{-2}$	$1.64 \times 10^{-2}$	$2.10 \times 10^{-2}$	$2.64 \times 10^{-2}$	$2.72 \times 10^{-2}$
$^{59}\text{Ni}$	$6.5 \times 10^{-6}$	$3.50 \times 10^{-6}$	$1.70 \times 10^{-6}$	$1.37 \times 10^{-6}$	$7.33 \times 10^{-5}$	$1.88 \times 10^{-5}$	$1.21 \times 10^{-5}$
$^{63}\text{Ni}$	$1.51 \times 10^{-12}$	$1.19 \times 10^{-13}$	$1.29 \times 10^{-13}$	$4.23 \times 10^{-14}$	$9.31 \times 10^{-8}$	$1.25 \times 10^{-12}$	$4.94 \times 10^{-13}$

**Note.** Masses are in units of solar mass.

## 7. Comparisons with Observed Supernovae and Supernova Remnants

We have shown in Leung & Nomoto (2017, 2018) and Nomoto & Leung (2017) that the Chandrasekhar-mass turbulent deflagration model with delayed detonation transition can be constrained through the observational data, including the late-time light curves and the spectra. The late-time light curves can give indications of the amount of minor isotopes that have a longer lifetime compared to  $^{56}\text{Ni}$  with a half-life of 7.8 days. They include, for example,  $^{56}\text{Co}$  and  $^{57}\text{Co}$ , which have decay lifetimes of 77.2 and 272 days, respectively. The energy deposition during the decay supports the light curve being observed. Another way to study SN chemical abundance is by the spectra of SNRs. Through a comparison of the X-ray line strengths of the radioactive elements, such as Cr, Mn, Fe, and Ni, one can obtain the ratio among these elements and thus cast constraints on the explosion mechanism (see, e.g., Yamaguchi et al. 2014).

### 7.1. Supernova Remnant 3C 397

The first example we study is the SNR 3C 397 (Yamaguchi et al. 2015). This SNR has a remarkable X-ray spectrum in terms of its rich neutronized material compared to other SNRs such as Tycho and Kepler. This remnant also shows that the

Chandrasekhar-mass model is one of the feasible realizations of SN Ia explosions constrained by direct observational data. In the measurement, this remnant is found to have  $0.027 \pm^{+0.007}_{-0.006} M_{\odot}$  Cr,  $0.025 \pm^{+0.008}_{-0.007} M_{\odot}$  Mn, and  $0.17 \pm^{+0.07}_{-0.05} M_{\odot}$  Ni. This corresponds to the Mn/Fe and Ni/Fe ratios being 0.018–0.033 and 0.11–0.24, respectively. In Yamaguchi et al. (2015) it is shown that by using one-dimensional models, the Chandrasekhar-mass model ( $M \approx 1.37 M_{\odot}$ ) with a metallicity five times the solar metallicity is shown to produce the closest abundance ratio. In Nomoto & Leung (2017) and Leung & Nomoto (2018) we reported a similar discovery based on a series of two-dimensional models of the turbulent deflagration model with delayed detonation transition. Here we shall examine our models to see in the sub-Chandrasekhar-mass domain what kind of model is needed to explain this SNR.

In Figure 27 we plot Mn/Fe against Ni/Fe for our sub-Chandrasekhar-mass models with the observational data from the SNR. The SN Ia models of  $M = 0.9\text{--}1.2 M_{\odot}$  are included with an He envelope of  $M_{\text{He}} = 0.1\text{--}0.2 M_{\odot}$ . We pick  $Z = 0\text{--}5 Z_{\odot}$  as done in Leung & Nomoto (2018). It can be seen that in general when metallicity increases, Mn/Fe increases with Ni/Fe. However, when the total mass  $M$  increases, the whole shifted downward, showing that the Mn/Fe ratio drops but no significant change in Ni/Fe was observed. This is because

**Table 14**  
Nucleosynthesis Yields for Stable Isotopes from the Selected Models Using an He Detonation Ring as the Initial Configuration

$M (M_{\odot})$	0.90	0.95	1.00	1.05	1.10	1.20
$^{12}\text{C}$	$6.40 \times 10^{-2}$	$6.0 \times 10^{-2}$	$1.15 \times 10^{-3}$	$6.86 \times 10^{-3}$	$4.2 \times 10^{-3}$	$7.84 \times 10^{-6}$
$^{13}\text{C}$	$2.2 \times 10^{-8}$	$1.60 \times 10^{-8}$	$3.2 \times 10^{-9}$	$7.8 \times 10^{-9}$	$8.97 \times 10^{-9}$	$1.6 \times 10^{-11}$
$^{14}\text{N}$	$5.8 \times 10^{-7}$	$4.40 \times 10^{-7}$	$1.63 \times 10^{-8}$	$1.14 \times 10^{-7}$	$7.62 \times 10^{-8}$	$6.96 \times 10^{-12}$
$^{15}\text{N}$	$1.2 \times 10^{-8}$	$1.14 \times 10^{-8}$	$2.13 \times 10^{-10}$	$1.71 \times 10^{-9}$	$1.38 \times 10^{-9}$	$9.11 \times 10^{-12}$
$^{16}\text{O}$	$4.28 \times 10^{-1}$	$3.86 \times 10^{-1}$	$6.64 \times 10^{-2}$	$1.35 \times 10^{-1}$	$1.2 \times 10^{-1}$	$6.89 \times 10^{-3}$
$^{17}\text{O}$	$2.96 \times 10^{-7}$	$2.56 \times 10^{-7}$	$1.8 \times 10^{-8}$	$6.97 \times 10^{-8}$	$4.32 \times 10^{-8}$	$1.23 \times 10^{-13}$
$^{18}\text{O}$	$3.82 \times 10^{-9}$	$3.52 \times 10^{-9}$	$9.43 \times 10^{-11}$	$6.91 \times 10^{-10}$	$5.10 \times 10^{-10}$	$4.95 \times 10^{-16}$
$^{19}\text{F}$	$3.79 \times 10^{-10}$	$3.64 \times 10^{-10}$	$2.39 \times 10^{-11}$	$8.36 \times 10^{-11}$	$6.80 \times 10^{-11}$	$5.48 \times 10^{-16}$
$^{20}\text{Ne}$	$3.77 \times 10^{-2}$	$2.98 \times 10^{-2}$	$1.15 \times 10^{-3}$	$7.69 \times 10^{-3}$	$4.72 \times 10^{-3}$	$1.50 \times 10^{-6}$
$^{21}\text{Ne}$	$2.36 \times 10^{-6}$	$2.15 \times 10^{-6}$	$1.57 \times 10^{-7}$	$5.52 \times 10^{-7}$	$4.33 \times 10^{-7}$	$8.30 \times 10^{-11}$
$^{22}\text{Ne}$	$2.14 \times 10^{-3}$	$1.98 \times 10^{-3}$	$8.99 \times 10^{-9}$	$1.88 \times 10^{-4}$	$9.46 \times 10^{-5}$	$6.27 \times 10^{-11}$
$^{23}\text{Na}$	$1.51 \times 10^{-4}$	$1.31 \times 10^{-4}$	$8.39 \times 10^{-6}$	$2.97 \times 10^{-5}$	$2.10 \times 10^{-5}$	$8.5 \times 10^{-8}$
$^{24}\text{Mg}$	$5.56 \times 10^{-2}$	$4.28 \times 10^{-2}$	$1.28 \times 10^{-3}$	$1.15 \times 10^{-2}$	$8.62 \times 10^{-3}$	$3.2 \times 10^{-5}$
$^{25}\text{Mg}$	$4.1 \times 10^{-4}$	$3.13 \times 10^{-4}$	$1.45 \times 10^{-5}$	$7.25 \times 10^{-5}$	$4.99 \times 10^{-5}$	$2.42 \times 10^{-8}$
$^{26}\text{Mg}$	$4.88 \times 10^{-4}$	$4.22 \times 10^{-4}$	$2.72 \times 10^{-5}$	$9.78 \times 10^{-5}$	$6.65 \times 10^{-5}$	$9.82 \times 10^{-8}$
$^{26}\text{Al}$	$7.39 \times 10^{-5}$	$5.12 \times 10^{-5}$	$1.70 \times 10^{-6}$	$1.29 \times 10^{-5}$	$8.12 \times 10^{-6}$	$4.23 \times 10^{-9}$
$^{27}\text{Al}$	$5.4 \times 10^{-3}$	$3.75 \times 10^{-3}$	$1.14 \times 10^{-4}$	$9.34 \times 10^{-4}$	$7.17 \times 10^{-4}$	$2.68 \times 10^{-6}$
$^{28}\text{Si}$	$1.47 \times 10^{-1}$	$1.70 \times 10^{-1}$	$1.25 \times 10^{-1}$	$1.95 \times 10^{-1}$	$1.10 \times 10^{-1}$	$2.58 \times 10^{-2}$
$^{29}\text{Si}$	$4.31 \times 10^{-3}$	$3.75 \times 10^{-3}$	$2.67 \times 10^{-4}$	$1.11 \times 10^{-3}$	$8.24 \times 10^{-4}$	$1.33 \times 10^{-5}$
$^{30}\text{Si}$	$7.86 \times 10^{-3}$	$6.77 \times 10^{-3}$	$3.79 \times 10^{-4}$	$1.99 \times 10^{-3}$	$1.58 \times 10^{-3}$	$1.70 \times 10^{-5}$
$^{31}\text{P}$	$1.65 \times 10^{-3}$	$1.36 \times 10^{-3}$	$1.53 \times 10^{-4}$	$4.58 \times 10^{-4}$	$3.54 \times 10^{-4}$	$1.38 \times 10^{-5}$
$^{32}\text{S}$	$4.27 \times 10^{-2}$	$5.68 \times 10^{-2}$	$6.56 \times 10^{-2}$	$8.62 \times 10^{-2}$	$4.90 \times 10^{-2}$	$1.54 \times 10^{-2}$
$^{33}\text{S}$	$9.91 \times 10^{-4}$	$9.46 \times 10^{-4}$	$1.89 \times 10^{-4}$	$3.97 \times 10^{-4}$	$3.8 \times 10^{-4}$	$2.10 \times 10^{-5}$
$^{34}\text{S}$	$2.98 \times 10^{-3}$	$3.66 \times 10^{-3}$	$1.91 \times 10^{-3}$	$2.73 \times 10^{-3}$	$1.97 \times 10^{-3}$	$1.83 \times 10^{-4}$
$^{36}\text{S}$	$7.68 \times 10^{-7}$	$7.22 \times 10^{-7}$	$5.59 \times 10^{-8}$	$1.97 \times 10^{-7}$	$1.63 \times 10^{-7}$	$1.24 \times 10^{-9}$
$^{35}\text{Cl}$	$4.81 \times 10^{-4}$	$3.20 \times 10^{-4}$	$1.4 \times 10^{-4}$	$1.65 \times 10^{-4}$	$1.30 \times 10^{-4}$	$1.33 \times 10^{-5}$
$^{37}\text{Cl}$	$2.54 \times 10^{-5}$	$3.13 \times 10^{-5}$	$2.51 \times 10^{-5}$	$3.14 \times 10^{-5}$	$2.37 \times 10^{-5}$	$3.72 \times 10^{-6}$
$^{36}\text{Ar}$	$4.1 \times 10^{-3}$	$6.94 \times 10^{-3}$	$1.15 \times 10^{-2}$	$1.32 \times 10^{-2}$	$7.52 \times 10^{-3}$	$3.19 \times 10^{-3}$
$^{38}\text{Ar}$	$6.34 \times 10^{-4}$	$9.8 \times 10^{-4}$	$1.34 \times 10^{-3}$	$1.39 \times 10^{-3}$	$1.4 \times 10^{-3}$	$1.43 \times 10^{-4}$
$^{40}\text{Ar}$	$1.51 \times 10^{-8}$	$1.21 \times 10^{-8}$	$1.69 \times 10^{-9}$	$3.35 \times 10^{-9}$	$3.1 \times 10^{-9}$	$6.50 \times 10^{-11}$
$^{39}\text{K}$	$6.37 \times 10^{-5}$	$6.25 \times 10^{-5}$	$9.25 \times 10^{-5}$	$1.3 \times 10^{-4}$	$8.52 \times 10^{-5}$	$1.65 \times 10^{-5}$
$^{40}\text{K}$	$2.77 \times 10^{-7}$	$1.69 \times 10^{-7}$	$3.86 \times 10^{-8}$	$5.74 \times 10^{-8}$	$5.44 \times 10^{-8}$	$3.13 \times 10^{-9}$
$^{41}\text{K}$	$1.43 \times 10^{-8}$	$1.31 \times 10^{-8}$	$3.14 \times 10^{-9}$	$5.6 \times 10^{-9}$	$4.25 \times 10^{-9}$	$3.56 \times 10^{-10}$
$^{40}\text{Ca}$	$2.55 \times 10^{-3}$	$4.83 \times 10^{-3}$	$1.4 \times 10^{-2}$	$1.2 \times 10^{-2}$	$6.87 \times 10^{-3}$	$4.7 \times 10^{-3}$
$^{42}\text{Ca}$	$1.78 \times 10^{-5}$	$2.49 \times 10^{-5}$	$4.24 \times 10^{-5}$	$4.9 \times 10^{-5}$	$3.39 \times 10^{-5}$	$6.97 \times 10^{-6}$
$^{43}\text{Ca}$	$6.12 \times 10^{-6}$	$1.55 \times 10^{-6}$	$1.38 \times 10^{-5}$	$3.98 \times 10^{-6}$	$1.39 \times 10^{-5}$	$1.22 \times 10^{-5}$
$^{44}\text{Ca}$	$2.56 \times 10^{-5}$	$5.0 \times 10^{-6}$	$2.89 \times 10^{-5}$	$1.13 \times 10^{-5}$	$6.55 \times 10^{-5}$	$6.17 \times 10^{-5}$
$^{46}\text{Ca}$	$2.58 \times 10^{-10}$	$2.53 \times 10^{-10}$	$4.90 \times 10^{-11}$	$7.11 \times 10^{-11}$	$6.92 \times 10^{-11}$	$2.26 \times 10^{-12}$
$^{48}\text{Ca}$	$1.72 \times 10^{-15}$	$1.43 \times 10^{-15}$	$9.28 \times 10^{-16}$	$5.10 \times 10^{-16}$	$5.8 \times 10^{-16}$	$4.93 \times 10^{-18}$
$^{45}\text{Sc}$	$3.45 \times 10^{-7}$	$3.35 \times 10^{-7}$	$3.77 \times 10^{-7}$	$3.70 \times 10^{-7}$	$7.81 \times 10^{-7}$	$5.19 \times 10^{-7}$
$^{46}\text{Ti}$	$6.57 \times 10^{-6}$	$1.1 \times 10^{-5}$	$1.85 \times 10^{-5}$	$1.91 \times 10^{-5}$	$1.53 \times 10^{-5}$	$5.39 \times 10^{-6}$
$^{47}\text{Ti}$	$2.24 \times 10^{-5}$	$5.19 \times 10^{-6}$	$2.27 \times 10^{-5}$	$7.83 \times 10^{-6}$	$6.58 \times 10^{-5}$	$6.59 \times 10^{-5}$
$^{48}\text{Ti}$	$9.64 \times 10^{-4}$	$2.84 \times 10^{-4}$	$7.8 \times 10^{-4}$	$3.60 \times 10^{-4}$	$2.61 \times 10^{-3}$	$3.70 \times 10^{-3}$
$^{49}\text{Ti}$	$8.56 \times 10^{-6}$	$8.99 \times 10^{-6}$	$1.47 \times 10^{-5}$	$1.26 \times 10^{-5}$	$2.83 \times 10^{-5}$	$2.94 \times 10^{-5}$
$^{50}\text{Ti}$	$1.8 \times 10^{-9}$	$1.66 \times 10^{-9}$	$6.7 \times 10^{-10}$	$7.99 \times 10^{-10}$	$7.12 \times 10^{-10}$	$7.54 \times 10^{-11}$
$^{50}\text{V}$	$5.37 \times 10^{-9}$	$8.68 \times 10^{-9}$	$3.68 \times 10^{-9}$	$4.9 \times 10^{-9}$	$3.86 \times 10^{-9}$	$5.91 \times 10^{-10}$
$^{51}\text{V}$	$8.33 \times 10^{-5}$	$5.3 \times 10^{-5}$	$7.62 \times 10^{-5}$	$5.93 \times 10^{-5}$	$2.81 \times 10^{-4}$	$3.20 \times 10^{-4}$
$^{50}\text{Cr}$	$4.32 \times 10^{-5}$	$8.96 \times 10^{-5}$	$2.29 \times 10^{-4}$	$2.1 \times 10^{-4}$	$1.9 \times 10^{-4}$	$7.79 \times 10^{-5}$
$^{52}\text{Cr}$	$1.27 \times 10^{-3}$	$1.72 \times 10^{-3}$	$2.87 \times 10^{-3}$	$2.96 \times 10^{-3}$	$2.80 \times 10^{-3}$	$9.80 \times 10^{-3}$
$^{53}\text{Cr}$	$4.95 \times 10^{-5}$	$1.28 \times 10^{-4}$	$2.2 \times 10^{-4}$	$2.1 \times 10^{-4}$	$1.56 \times 10^{-4}$	$2.71 \times 10^{-4}$
$^{54}\text{Cr}$	$1.79 \times 10^{-8}$	$8.10 \times 10^{-8}$	$8.83 \times 10^{-8}$	$5.64 \times 10^{-8}$	$6.70 \times 10^{-8}$	$1.59 \times 10^{-8}$
$^{55}\text{Mn}$	$3.18 \times 10^{-4}$	$7.12 \times 10^{-4}$	$1.8 \times 10^{-3}$	$1.16 \times 10^{-3}$	$9.15 \times 10^{-4}$	$1.99 \times 10^{-3}$
$^{54}\text{Fe}$	$1.71 \times 10^{-3}$	$4.12 \times 10^{-3}$	$1.11 \times 10^{-2}$	$1.7 \times 10^{-2}$	$5.20 \times 10^{-3}$	$5.59 \times 10^{-3}$
$^{56}\text{Fe}$	$3.58 \times 10^{-2}$	$1.7 \times 10^{-1}$	$3.12 \times 10^{-1}$	$4.68 \times 10^{-1}$	$6.84 \times 10^{-1}$	$9.21 \times 10^{-1}$
$^{57}\text{Fe}$	$1.5 \times 10^{-3}$	$3.5 \times 10^{-3}$	$8.17 \times 10^{-3}$	$1.24 \times 10^{-2}$	$1.90 \times 10^{-2}$	$2.71 \times 10^{-2}$
$^{58}\text{Fe}$	$4.54 \times 10^{-9}$	$5.66 \times 10^{-8}$	$2.43 \times 10^{-8}$	$1.56 \times 10^{-8}$	$4.83 \times 10^{-8}$	$4.68 \times 10^{-9}$
$^{60}\text{Fe}$	$7.82 \times 10^{-19}$	$1.26 \times 10^{-18}$	$2.67 \times 10^{-18}$	$9.49 \times 10^{-19}$	$1.11 \times 10^{-18}$	$4.29 \times 10^{-19}$
$^{59}\text{Co}$	$3.75 \times 10^{-5}$	$9.83 \times 10^{-5}$	$3.17 \times 10^{-4}$	$4.28 \times 10^{-4}$	$6.17 \times 10^{-4}$	$6.63 \times 10^{-4}$
$^{58}\text{Ni}$	$1.17 \times 10^{-3}$	$3.62 \times 10^{-3}$	$1.26 \times 10^{-2}$	$1.95 \times 10^{-2}$	$3.6 \times 10^{-2}$	$4.53 \times 10^{-2}$
$^{60}\text{Ni}$	$6.86 \times 10^{-4}$	$1.60 \times 10^{-3}$	$3.87 \times 10^{-3}$	$5.7 \times 10^{-3}$	$6.41 \times 10^{-3}$	$6.13 \times 10^{-3}$
$^{61}\text{Ni}$	$6.4 \times 10^{-5}$	$9.30 \times 10^{-5}$	$1.55 \times 10^{-4}$	$1.97 \times 10^{-4}$	$2.48 \times 10^{-4}$	$3.21 \times 10^{-4}$
$^{62}\text{Ni}$	$1.61 \times 10^{-4}$	$3.91 \times 10^{-4}$	$1.8 \times 10^{-3}$	$1.43 \times 10^{-3}$	$1.83 \times 10^{-3}$	$1.69 \times 10^{-3}$
$^{64}\text{Ni}$	$3.0 \times 10^{-14}$	$7.77 \times 10^{-10}$	$1.49 \times 10^{-12}$	$3.69 \times 10^{-13}$	$8.3 \times 10^{-13}$	$1.13 \times 10^{-13}$
$^{63}\text{Cu}$	$4.77 \times 10^{-7}$	$5.25 \times 10^{-7}$	$1.19 \times 10^{-6}$	$1.35 \times 10^{-6}$	$2.24 \times 10^{-6}$	$2.83 \times 10^{-6}$



**Table 14**  
(Continued)

$M (M_{\odot})$	0.90	0.95	1.00	1.05	1.10	1.20
$^{65}\text{Cu}$	$3.10 \times 10^{-6}$	$1.82 \times 10^{-6}$	$2.11 \times 10^{-6}$	$2.17 \times 10^{-6}$	$3.49 \times 10^{-6}$	$6.87 \times 10^{-6}$
$^{64}\text{Zn}$	$1.16 \times 10^{-5}$	$1.19 \times 10^{-5}$	$1.71 \times 10^{-5}$	$1.32 \times 10^{-5}$	$1.30 \times 10^{-5}$	$4.32 \times 10^{-5}$
$^{66}\text{Zn}$	$7.85 \times 10^{-6}$	$9.57 \times 10^{-6}$	$1.49 \times 10^{-5}$	$1.73 \times 10^{-5}$	$2.15 \times 10^{-5}$	$2.83 \times 10^{-5}$
$^{67}\text{Zn}$	$3.36 \times 10^{-7}$	$3.35 \times 10^{-7}$	$3.16 \times 10^{-7}$	$3.61 \times 10^{-7}$	$1.21 \times 10^{-6}$	$2.25 \times 10^{-6}$
$^{68}\text{Zn}$	$4.42 \times 10^{-7}$	$4.83 \times 10^{-7}$	$4.55 \times 10^{-7}$	$2.69 \times 10^{-7}$	$4.7 \times 10^{-7}$	$2.25 \times 10^{-6}$
$^{70}\text{Zn}$	$4.23 \times 10^{-15}$	$4.3 \times 10^{-14}$	$1.96 \times 10^{-17}$	$1.29 \times 10^{-15}$	$5.22 \times 10^{-17}$	$9.12 \times 10^{-19}$

**Note.** Based on the benchmark model 110-050-2-B50.  $M_{\text{He}} = 0.05 M_{\odot}$  for all models in this table. Masses are in units of solar mass.

**Table 15**  
Similar to Table 14, but for the Radioactive Isotopes

$M (M_{\odot})$	0.90	0.95	1.00	1.05	1.10	1.20
$^{22}\text{Na}$	$1.12 \times 10^{-7}$	$9.86 \times 10^{-8}$	$3.74 \times 10^{-9}$	$2.49 \times 10^{-8}$	$1.56 \times 10^{-8}$	$4.95 \times 10^{-11}$
$^{26}\text{Al}$	$7.39 \times 10^{-5}$	$5.12 \times 10^{-5}$	$1.70 \times 10^{-6}$	$1.29 \times 10^{-5}$	$8.12 \times 10^{-6}$	$4.10 \times 10^{-9}$
$^{39}\text{Ar}$	$3.52 \times 10^{-8}$	$2.39 \times 10^{-8}$	$7.27 \times 10^{-9}$	$9.79 \times 10^{-9}$	$8.69 \times 10^{-9}$	$5.15 \times 10^{-10}$
$^{40}\text{K}$	$2.77 \times 10^{-7}$	$1.69 \times 10^{-7}$	$3.86 \times 10^{-8}$	$5.74 \times 10^{-8}$	$5.44 \times 10^{-8}$	$3.13 \times 10^{-9}$
$^{41}\text{Ca}$	$2.77 \times 10^{-6}$	$4.13 \times 10^{-6}$	$5.66 \times 10^{-6}$	$6.52 \times 10^{-6}$	$5.71 \times 10^{-6}$	$1.22 \times 10^{-6}$
$^{44}\text{Ti}$	$2.33 \times 10^{-4}$	$4.37 \times 10^{-5}$	$2.64 \times 10^{-4}$	$1.2 \times 10^{-4}$	$5.99 \times 10^{-4}$	$5.65 \times 10^{-4}$
$^{48}\text{V}$	$2.67 \times 10^{-7}$	$1.43 \times 10^{-7}$	$1.96 \times 10^{-7}$	$1.59 \times 10^{-7}$	$1.15 \times 10^{-6}$	$6.95 \times 10^{-7}$
$^{49}\text{V}$	$9.7 \times 10^{-8}$	$1.73 \times 10^{-7}$	$1.54 \times 10^{-7}$	$1.52 \times 10^{-7}$	$1.85 \times 10^{-7}$	$4.78 \times 10^{-8}$
$^{53}\text{Mn}$	$3.45 \times 10^{-6}$	$9.83 \times 10^{-6}$	$9.5 \times 10^{-6}$	$1.40 \times 10^{-5}$	$1.15 \times 10^{-5}$	$1.85 \times 10^{-6}$
$^{60}\text{Fe}$	$1.16 \times 10^{-17}$	$1.81 \times 10^{-17}$	$4.59 \times 10^{-17}$	$1.36 \times 10^{-17}$	$1.62 \times 10^{-17}$	$5.72 \times 10^{-18}$
$^{56}\text{Co}$	$9.18 \times 10^{-7}$	$1.37 \times 10^{-5}$	$8.93 \times 10^{-6}$	$4.75 \times 10^{-6}$	$1.79 \times 10^{-5}$	$9.50 \times 10^{-6}$
$^{57}\text{Co}$	$1.57 \times 10^{-6}$	$7.14 \times 10^{-6}$	$5.62 \times 10^{-6}$	$7.38 \times 10^{-6}$	$9.87 \times 10^{-6}$	$1.41 \times 10^{-6}$
$^{60}\text{Co}$	$3.98 \times 10^{-14}$	$1.83 \times 10^{-12}$	$1.17 \times 10^{-13}$	$1.4 \times 10^{-13}$	$6.59 \times 10^{-13}$	$3.60 \times 10^{-14}$
$^{56}\text{Ni}$	$3.58 \times 10^{-2}$	$1.7 \times 10^{-1}$	$6.0 \times 10^{-1}$	$4.68 \times 10^{-1}$	$6.84 \times 10^{-1}$	$9.95 \times 10^{-1}$
$^{57}\text{Ni}$	$1.5 \times 10^{-3}$	$3.4 \times 10^{-3}$	$1.60 \times 10^{-2}$	$1.24 \times 10^{-2}$	$1.90 \times 10^{-2}$	$2.82 \times 10^{-2}$
$^{59}\text{Ni}$	$3.98 \times 10^{-7}$	$2.88 \times 10^{-6}$	$2.89 \times 10^{-6}$	$1.92 \times 10^{-6}$	$4.77 \times 10^{-6}$	$4.30 \times 10^{-6}$
$^{63}\text{Ni}$	$5.77 \times 10^{-16}$	$7.35 \times 10^{-12}$	$2.12 \times 10^{-15}$	$9.42 \times 10^{-15}$	$2.62 \times 10^{-14}$	$2.97 \times 10^{-15}$

**Note.** Masses are in units of solar mass.

when the mass increases, the central density of the initial model increases; therefore, the C detonation becomes more energetic, which can unbind the star more quickly. As a result, more  $^{56}\text{Ni}$  is produced, which suppresses the ratio.

The model with a more massive He envelope has a lower [Mn/Fe] in general because of the higher  $^{56}\text{Ni}$ , as part of it can be produced in the envelope. This relation is uniform for almost all models except for  $Z = 5 Z_{\odot}$  at  $M = 1.2 M_{\odot}$ . The two models show a rapid jump in the [Mn/Fe] ratio. This is because at high density, electron density becomes important. The C detonation, which can release adequate energy to burn the core matter into NSE, is followed by electron capture before the matter cooling down by adiabatic expansion. Certainly, the typical electron capture rate in the sub-Chandrasekhar-mass model is considerably lower than those in typical Chandrasekhar-mass models. The lowered electron fraction in the core matter, when in NSE, will be more favorable to produce  $^{55}\text{Mn}$ , which has a proton ratio of 0.454. The data point of 3C 397 is included. It can be seen that the data point lies very far from the other lines. This is consistent with the conclusion in Yamaguchi et al. (2015) that the SD Chandrasekhar-mass SN Ia channel is more likely to explain this peculiar SN Ia.

Our models show that the  $^{55}\text{Mn}$  production is in general so low that even with a rather small  $^{56}\text{Ni}$  production at the end of simulation, the resultant [Mn/Fe] ratio remains insufficient to explain. The closest model is the  $M = 0.9 M_{\odot}$  at  $Z = 5 Z_{\odot}$ . Our result is comparable to theirs.

One may note that this object has raised interest in the literature owing to its predicted high metallicity, and different proposals are raised in order to recover the high [Mn/Fe] ratio without invoking the high metallicity. For example, in Shen et al. (2018) the sub-Chandrasekhar-mass SN Ia in the spherical approximation is revisited. The high [Mn/Fe] is shown to be viable if one considers a subset of ejecta, namely, by taking the effects of reverse shock heating into account. Another attempt is done in Dave et al. (2017). The gravitational confined detonation model is explored with extension to pure turbulent deflagration with or without delayed detonation transition for the Chandrasekhar-mass model. It is shown that a combination of high central density, low [C/O] ratio, and high offset of initial deflagration can provide an alternative to this observation. These trends are consistent with our previous finding as reported in Leung & Nomoto (2018).

## 7.2. SN 2012cg

The next application is on SN 2012cg. This SN exploded at 2012 May 17 (UT) in the nearby spiral galaxy NGC 4424, which is measured in the Lick Observatory Supernova Search (Kandrashoff et al. 2012). The SN Ia nature is revealed in the spectral study found in Cenko et al. (2012) and Marion et al. (2012). This SN Ia is close enough that the late-time light curve after  $\sim 1000$  days can still be measured. The low-density ejecta becomes transparent to most  $\gamma$ -rays so that the  $\gamma$ -rays emitted during decay can escape freely from the ejecta without

**Table 16**  
Nucleosynthesis Yields for Stable Isotopes from the Selected Models Using a Spherical He Detonation as the Initial Configuration

$M (M_{\odot})$	0.90	0.95	1.00	1.05	1.10	1.20
$^{12}\text{C}$	$5.27 \times 10^{-3}$	$4.1 \times 10^{-3}$	$1.15 \times 10^{-3}$	$2.97 \times 10^{-4}$	$7.65 \times 10^{-4}$	$7.84 \times 10^{-6}$
$^{13}\text{C}$	$1.15 \times 10^{-7}$	$3.32 \times 10^{-7}$	$3.2 \times 10^{-9}$	$4.6 \times 10^{-11}$	$3.70 \times 10^{-10}$	$1.6 \times 10^{-11}$
$^{14}\text{N}$	$4.51 \times 10^{-7}$	$4.93 \times 10^{-7}$	$1.63 \times 10^{-8}$	$2.22 \times 10^{-10}$	$1.54 \times 10^{-9}$	$6.96 \times 10^{-12}$
$^{15}\text{N}$	$3.24 \times 10^{-9}$	$2.61 \times 10^{-9}$	$2.13 \times 10^{-10}$	$6.54 \times 10^{-11}$	$1.27 \times 10^{-10}$	$9.11 \times 10^{-12}$
$^{16}\text{O}$	$2.67 \times 10^{-1}$	$1.14 \times 10^{-1}$	$6.64 \times 10^{-2}$	$3.90 \times 10^{-2}$	$2.30 \times 10^{-2}$	$6.89 \times 10^{-3}$
$^{17}\text{O}$	$1.88 \times 10^{-7}$	$1.62 \times 10^{-7}$	$1.8 \times 10^{-8}$	$8.12 \times 10^{-11}$	$8.10 \times 10^{-10}$	$1.23 \times 10^{-13}$
$^{18}\text{O}$	$3.51 \times 10^{-9}$	$3.29 \times 10^{-9}$	$9.43 \times 10^{-11}$	$1.99 \times 10^{-12}$	$1.46 \times 10^{-11}$	$4.95 \times 10^{-16}$
$^{19}\text{F}$	$2.71 \times 10^{-10}$	$2.20 \times 10^{-10}$	$2.39 \times 10^{-11}$	$9.14 \times 10^{-13}$	$6.1 \times 10^{-12}$	$5.48 \times 10^{-16}$
$^{20}\text{Ne}$	$6.53 \times 10^{-3}$	$1.46 \times 10^{-3}$	$1.15 \times 10^{-3}$	$4.63 \times 10^{-4}$	$7.54 \times 10^{-4}$	$1.50 \times 10^{-6}$
$^{21}\text{Ne}$	$1.62 \times 10^{-6}$	$1.34 \times 10^{-6}$	$1.57 \times 10^{-7}$	$1.40 \times 10^{-8}$	$5.1 \times 10^{-8}$	$8.30 \times 10^{-11}$
$^{22}\text{Ne}$	$7.66 \times 10^{-5}$	$8.61 \times 10^{-5}$	$8.99 \times 10^{-9}$	$1.53 \times 10^{-9}$	$3.64 \times 10^{-9}$	$6.27 \times 10^{-11}$
$^{23}\text{Na}$	$4.32 \times 10^{-5}$	$2.30 \times 10^{-5}$	$8.39 \times 10^{-6}$	$3.35 \times 10^{-6}$	$4.66 \times 10^{-6}$	$8.5 \times 10^{-8}$
$^{24}\text{Mg}$	$2.29 \times 10^{-2}$	$2.53 \times 10^{-3}$	$1.28 \times 10^{-3}$	$5.46 \times 10^{-4}$	$4.43 \times 10^{-4}$	$3.2 \times 10^{-5}$
$^{25}\text{Mg}$	$1.0 \times 10^{-4}$	$3.6 \times 10^{-5}$	$1.45 \times 10^{-5}$	$3.84 \times 10^{-6}$	$7.30 \times 10^{-6}$	$2.42 \times 10^{-8}$
$^{26}\text{Mg}$	$1.26 \times 10^{-4}$	$4.20 \times 10^{-5}$	$2.72 \times 10^{-5}$	$7.3 \times 10^{-6}$	$1.21 \times 10^{-5}$	$9.82 \times 10^{-8}$
$^{26}\text{Al}$	$1.39 \times 10^{-5}$	$2.16 \times 10^{-6}$	$1.70 \times 10^{-6}$	$8.41 \times 10^{-7}$	$1.3 \times 10^{-6}$	$4.23 \times 10^{-9}$
$^{27}\text{Al}$	$1.98 \times 10^{-3}$	$2.16 \times 10^{-4}$	$1.14 \times 10^{-4}$	$5.41 \times 10^{-5}$	$4.32 \times 10^{-5}$	$2.68 \times 10^{-6}$
$^{28}\text{Si}$	$3.32 \times 10^{-1}$	$1.60 \times 10^{-1}$	$1.25 \times 10^{-1}$	$1.3 \times 10^{-1}$	$7.51 \times 10^{-2}$	$2.58 \times 10^{-2}$
$^{29}\text{Si}$	$2.3 \times 10^{-3}$	$4.80 \times 10^{-4}$	$2.67 \times 10^{-4}$	$1.31 \times 10^{-4}$	$1.10 \times 10^{-4}$	$1.33 \times 10^{-5}$
$^{30}\text{Si}$	$4.47 \times 10^{-3}$	$8.4 \times 10^{-4}$	$3.79 \times 10^{-4}$	$1.76 \times 10^{-4}$	$1.13 \times 10^{-4}$	$1.70 \times 10^{-5}$
$^{31}\text{P}$	$9.78 \times 10^{-4}$	$2.75 \times 10^{-4}$	$1.53 \times 10^{-4}$	$9.56 \times 10^{-5}$	$5.26 \times 10^{-5}$	$1.38 \times 10^{-5}$
$^{32}\text{S}$	$1.41 \times 10^{-1}$	$8.0 \times 10^{-2}$	$6.56 \times 10^{-2}$	$5.45 \times 10^{-2}$	$4.7 \times 10^{-2}$	$1.54 \times 10^{-2}$
$^{33}\text{S}$	$8.94 \times 10^{-4}$	$3.18 \times 10^{-4}$	$1.89 \times 10^{-4}$	$1.27 \times 10^{-4}$	$6.98 \times 10^{-5}$	$2.10 \times 10^{-5}$
$^{34}\text{S}$	$5.22 \times 10^{-3}$	$3.17 \times 10^{-3}$	$1.91 \times 10^{-3}$	$1.12 \times 10^{-3}$	$5.83 \times 10^{-4}$	$1.83 \times 10^{-4}$
$^{36}\text{S}$	$4.80 \times 10^{-7}$	$1.2 \times 10^{-7}$	$5.59 \times 10^{-8}$	$2.86 \times 10^{-8}$	$3.59 \times 10^{-8}$	$1.24 \times 10^{-9}$
$^{35}\text{Cl}$	$3.58 \times 10^{-4}$	$1.43 \times 10^{-4}$	$1.4 \times 10^{-4}$	$8.11 \times 10^{-5}$	$4.65 \times 10^{-5}$	$1.33 \times 10^{-5}$
$^{37}\text{Cl}$	$7.9 \times 10^{-5}$	$3.32 \times 10^{-5}$	$2.51 \times 10^{-5}$	$2.1 \times 10^{-5}$	$1.17 \times 10^{-5}$	$3.72 \times 10^{-6}$
$^{36}\text{Ar}$	$1.88 \times 10^{-2}$	$1.34 \times 10^{-2}$	$1.15 \times 10^{-2}$	$9.40 \times 10^{-3}$	$7.42 \times 10^{-3}$	$3.19 \times 10^{-3}$
$^{38}\text{Ar}$	$3.40 \times 10^{-3}$	$1.88 \times 10^{-3}$	$1.34 \times 10^{-3}$	$9.84 \times 10^{-4}$	$5.11 \times 10^{-4}$	$1.43 \times 10^{-4}$
$^{40}\text{Ar}$	$9.41 \times 10^{-9}$	$2.57 \times 10^{-9}$	$1.69 \times 10^{-9}$	$1.25 \times 10^{-9}$	$8.67 \times 10^{-10}$	$6.50 \times 10^{-11}$
$^{39}\text{K}$	$2.56 \times 10^{-4}$	$1.13 \times 10^{-4}$	$9.25 \times 10^{-5}$	$7.56 \times 10^{-5}$	$4.69 \times 10^{-5}$	$1.65 \times 10^{-5}$
$^{40}\text{K}$	$1.59 \times 10^{-7}$	$5.28 \times 10^{-8}$	$3.86 \times 10^{-8}$	$3.31 \times 10^{-8}$	$1.73 \times 10^{-8}$	$3.13 \times 10^{-9}$
$^{41}\text{K}$	$1.23 \times 10^{-8}$	$4.90 \times 10^{-9}$	$3.14 \times 10^{-9}$	$2.38 \times 10^{-9}$	$1.45 \times 10^{-9}$	$3.56 \times 10^{-10}$
$^{40}\text{Ca}$	$1.17 \times 10^{-2}$	$1.12 \times 10^{-2}$	$1.4 \times 10^{-2}$	$7.54 \times 10^{-3}$	$6.70 \times 10^{-3}$	$4.7 \times 10^{-3}$
$^{42}\text{Ca}$	$1.3 \times 10^{-4}$	$5.63 \times 10^{-5}$	$4.24 \times 10^{-5}$	$3.24 \times 10^{-5}$	$1.85 \times 10^{-5}$	$6.97 \times 10^{-6}$
$^{43}\text{Ca}$	$1.22 \times 10^{-6}$	$4.26 \times 10^{-6}$	$1.38 \times 10^{-5}$	$5.89 \times 10^{-6}$	$7.6 \times 10^{-6}$	$1.22 \times 10^{-5}$
$^{44}\text{Ca}$	$3.81 \times 10^{-6}$	$6.72 \times 10^{-6}$	$2.89 \times 10^{-5}$	$6.32 \times 10^{-6}$	$2.11 \times 10^{-5}$	$6.17 \times 10^{-5}$
$^{46}\text{Ca}$	$2.42 \times 10^{-10}$	$7.92 \times 10^{-11}$	$4.90 \times 10^{-11}$	$4.55 \times 10^{-11}$	$1.93 \times 10^{-11}$	$2.26 \times 10^{-12}$
$^{48}\text{Ca}$	$1.85 \times 10^{-15}$	$9.88 \times 10^{-16}$	$9.28 \times 10^{-16}$	$7.92 \times 10^{-16}$	$7.98 \times 10^{-16}$	$4.93 \times 10^{-18}$
$^{45}\text{Sc}$	$6.22 \times 10^{-7}$	$3.73 \times 10^{-7}$	$3.77 \times 10^{-7}$	$2.18 \times 10^{-7}$	$7.16 \times 10^{-7}$	$5.19 \times 10^{-7}$
$^{46}\text{Ti}$	$5.46 \times 10^{-5}$	$2.20 \times 10^{-5}$	$1.85 \times 10^{-5}$	$1.50 \times 10^{-5}$	$1.41 \times 10^{-5}$	$5.39 \times 10^{-6}$
$^{47}\text{Ti}$	$5.34 \times 10^{-6}$	$4.63 \times 10^{-6}$	$2.27 \times 10^{-5}$	$8.32 \times 10^{-6}$	$2.61 \times 10^{-5}$	$6.59 \times 10^{-5}$
$^{48}\text{Ti}$	$1.51 \times 10^{-4}$	$2.92 \times 10^{-4}$	$7.8 \times 10^{-4}$	$2.58 \times 10^{-4}$	$9.96 \times 10^{-4}$	$3.70 \times 10^{-3}$
$^{49}\text{Ti}$	$8.47 \times 10^{-6}$	$1.58 \times 10^{-5}$	$1.47 \times 10^{-5}$	$8.40 \times 10^{-6}$	$1.33 \times 10^{-5}$	$2.94 \times 10^{-5}$
$^{50}\text{Ti}$	$2.16 \times 10^{-9}$	$1.42 \times 10^{-9}$	$6.7 \times 10^{-10}$	$4.45 \times 10^{-10}$	$1.13 \times 10^{-10}$	$7.54 \times 10^{-11}$
$^{50}\text{V}$	$9.96 \times 10^{-9}$	$7.6 \times 10^{-9}$	$3.68 \times 10^{-9}$	$2.87 \times 10^{-9}$	$1.23 \times 10^{-9}$	$5.91 \times 10^{-10}$
$^{51}\text{V}$	$3.31 \times 10^{-5}$	$5.99 \times 10^{-5}$	$7.62 \times 10^{-5}$	$3.46 \times 10^{-5}$	$7.64 \times 10^{-5}$	$3.20 \times 10^{-4}$
$^{50}\text{Cr}$	$3.1 \times 10^{-4}$	$1.63 \times 10^{-4}$	$1.41 \times 10^{-4}$	$1.22 \times 10^{-4}$	$1.13 \times 10^{-4}$	$2.93 \times 10^{-5}$
$^{52}\text{Cr}$	$5.29 \times 10^{-4}$	$2.99 \times 10^{-3}$	$2.94 \times 10^{-3}$	$1.73 \times 10^{-3}$	$2.14 \times 10^{-3}$	$7.38 \times 10^{-3}$
$^{53}\text{Cr}$	$8.54 \times 10^{-5}$	$2.63 \times 10^{-4}$	$2.14 \times 10^{-4}$	$1.38 \times 10^{-4}$	$1.44 \times 10^{-4}$	$2.6 \times 10^{-4}$
$^{54}\text{Cr}$	$1.3 \times 10^{-7}$	$5.22 \times 10^{-8}$	$4.40 \times 10^{-8}$	$4.64 \times 10^{-8}$	$3.17 \times 10^{-8}$	$1.45 \times 10^{-10}$
$^{55}\text{Mn}$	$4.60 \times 10^{-4}$	$1.58 \times 10^{-3}$	$1.32 \times 10^{-3}$	$7.88 \times 10^{-4}$	$8.56 \times 10^{-4}$	$6.32 \times 10^{-4}$
$^{54}\text{Fe}$	$1.17 \times 10^{-2}$	$1.2 \times 10^{-2}$	$8.69 \times 10^{-3}$	$7.1 \times 10^{-3}$	$5.94 \times 10^{-3}$	$6.38 \times 10^{-4}$
$^{56}\text{Fe}$	$1.55 \times 10^{-2}$	$4.52 \times 10^{-1}$	$6.0 \times 10^{-1}$	$7.4 \times 10^{-1}$	$8.17 \times 10^{-1}$	$10.48 \times 10^{-1}$
$^{57}\text{Fe}$	$5.52 \times 10^{-4}$	$1.14 \times 10^{-2}$	$1.60 \times 10^{-2}$	$1.91 \times 10^{-2}$	$2.29 \times 10^{-2}$	$1.95 \times 10^{-2}$
$^{58}\text{Fe}$	$2.94 \times 10^{-8}$	$2.31 \times 10^{-8}$	$1.36 \times 10^{-8}$	$1.30 \times 10^{-8}$	$1.5 \times 10^{-8}$	$7.23 \times 10^{-11}$
$^{60}\text{Fe}$	$2.99 \times 10^{-18}$	$4.95 \times 10^{-18}$	$3.4 \times 10^{-18}$	$5.0 \times 10^{-18}$	$1.5 \times 10^{-16}$	$2.21 \times 10^{-22}$
$^{59}\text{Co}$	$1.42 \times 10^{-5}$	$3.86 \times 10^{-4}$	$5.27 \times 10^{-4}$	$6.13 \times 10^{-4}$	$7.14 \times 10^{-4}$	$1.74 \times 10^{-4}$
$^{58}\text{Ni}$	$7.72 \times 10^{-4}$	$1.79 \times 10^{-2}$	$2.50 \times 10^{-2}$	$3.5 \times 10^{-2}$	$3.60 \times 10^{-2}$	$7.7 \times 10^{-3}$
$^{60}\text{Ni}$	$5.19 \times 10^{-4}$	$4.99 \times 10^{-3}$	$6.13 \times 10^{-3}$	$6.87 \times 10^{-3}$	$8.16 \times 10^{-3}$	$1.0 \times 10^{-2}$
$^{61}\text{Ni}$	$4.72 \times 10^{-5}$	$1.81 \times 10^{-4}$	$2.78 \times 10^{-4}$	$2.77 \times 10^{-4}$	$3.84 \times 10^{-4}$	$3.61 \times 10^{-4}$
$^{62}\text{Ni}$	$3.33 \times 10^{-5}$	$1.41 \times 10^{-3}$	$1.72 \times 10^{-3}$	$1.88 \times 10^{-3}$	$2.5 \times 10^{-3}$	$2.97 \times 10^{-4}$
$^{64}\text{Ni}$	$8.46 \times 10^{-12}$	$5.56 \times 10^{-12}$	$4.59 \times 10^{-14}$	$4.90 \times 10^{-13}$	$1.25 \times 10^{-11}$	$1.80 \times 10^{-13}$
$^{63}\text{Cu}$	$4.69 \times 10^{-7}$	$1.21 \times 10^{-6}$	$2.50 \times 10^{-6}$	$2.29 \times 10^{-6}$	$2.49 \times 10^{-6}$	$5.65 \times 10^{-6}$

**Table 16**  
(Continued)

$M (M_{\odot})$	0.90	0.95	1.00	1.05	1.10	1.20
$^{65}\text{Cu}$	$1.89 \times 10^{-6}$	$1.76 \times 10^{-6}$	$7.61 \times 10^{-6}$	$4.82 \times 10^{-6}$	$9.8 \times 10^{-6}$	$1.28 \times 10^{-5}$
$^{64}\text{Zn}$	$1.57 \times 10^{-5}$	$9.39 \times 10^{-6}$	$2.70 \times 10^{-5}$	$2.48 \times 10^{-5}$	$7.18 \times 10^{-5}$	$2.3 \times 10^{-4}$
$^{66}\text{Zn}$	$2.15 \times 10^{-6}$	$1.81 \times 10^{-5}$	$2.41 \times 10^{-5}$	$2.33 \times 10^{-5}$	$2.52 \times 10^{-5}$	$1.65 \times 10^{-5}$
$^{67}\text{Zn}$	$1.91 \times 10^{-7}$	$1.89 \times 10^{-7}$	$3.41 \times 10^{-7}$	$2.13 \times 10^{-7}$	$6.33 \times 10^{-7}$	$2.31 \times 10^{-6}$
$^{68}\text{Zn}$	$1.0 \times 10^{-6}$	$2.82 \times 10^{-7}$	$3.71 \times 10^{-7}$	$2.25 \times 10^{-7}$	$2.9 \times 10^{-6}$	$3.74 \times 10^{-6}$
$^{70}\text{Zn}$	$2.71 \times 10^{-15}$	$1.77 \times 10^{-16}$	$1.97 \times 10^{-18}$	$2.46 \times 10^{-16}$	$9.85 \times 10^{-15}$	$4.73 \times 10^{-18}$

**Note.** Based on the benchmark model 110-050-2-S50.  $M_{\text{He}} = 0.05 M_{\odot}$  for all models in this table. Masses are in units of solar mass.

**Table 17**  
Similar to Table 16, but for the Radioactive Isotopes

$M (M_{\odot})$	0.90	0.95	1.00	1.05	1.10	1.20
$^{22}\text{Na}$	$1.94 \times 10^{-8}$	$5.10 \times 10^{-9}$	$3.74 \times 10^{-9}$	$1.31 \times 10^{-9}$	$2.46 \times 10^{-9}$	$4.95 \times 10^{-11}$
$^{26}\text{Al}$	$1.39 \times 10^{-5}$	$2.16 \times 10^{-6}$	$1.70 \times 10^{-6}$	$8.41 \times 10^{-7}$	$1.3 \times 10^{-6}$	$4.10 \times 10^{-9}$
$^{39}\text{Ar}$	$2.33 \times 10^{-8}$	$1.1 \times 10^{-8}$	$7.27 \times 10^{-9}$	$5.89 \times 10^{-9}$	$3.48 \times 10^{-9}$	$5.15 \times 10^{-10}$
$^{40}\text{K}$	$1.59 \times 10^{-7}$	$5.28 \times 10^{-8}$	$3.86 \times 10^{-8}$	$3.31 \times 10^{-8}$	$1.73 \times 10^{-8}$	$3.13 \times 10^{-9}$
$^{41}\text{Ca}$	$1.56 \times 10^{-5}$	$6.89 \times 10^{-6}$	$5.66 \times 10^{-6}$	$4.75 \times 10^{-6}$	$3.43 \times 10^{-6}$	$1.22 \times 10^{-6}$
$^{44}\text{Ti}$	$3.27 \times 10^{-5}$	$6.5 \times 10^{-5}$	$2.64 \times 10^{-4}$	$5.75 \times 10^{-5}$	$1.93 \times 10^{-4}$	$5.65 \times 10^{-4}$
$^{48}\text{V}$	$2.8 \times 10^{-7}$	$1.81 \times 10^{-7}$	$1.96 \times 10^{-7}$	$5.81 \times 10^{-8}$	$3.20 \times 10^{-7}$	$6.95 \times 10^{-7}$
$^{49}\text{V}$	$2.76 \times 10^{-7}$	$2.21 \times 10^{-7}$	$1.54 \times 10^{-7}$	$1.24 \times 10^{-7}$	$1.72 \times 10^{-7}$	$4.78 \times 10^{-8}$
$^{53}\text{Mn}$	$2.76 \times 10^{-5}$	$1.14 \times 10^{-5}$	$9.5 \times 10^{-6}$	$9.36 \times 10^{-6}$	$6.47 \times 10^{-6}$	$1.85 \times 10^{-6}$
$^{60}\text{Fe}$	$4.31 \times 10^{-17}$	$7.35 \times 10^{-17}$	$4.59 \times 10^{-17}$	$7.34 \times 10^{-17}$	$1.54 \times 10^{-15}$	$5.72 \times 10^{-18}$
$^{56}\text{Co}$	$3.65 \times 10^{-6}$	$2.15 \times 10^{-5}$	$8.93 \times 10^{-6}$	$3.8 \times 10^{-6}$	$3.80 \times 10^{-6}$	$9.50 \times 10^{-6}$
$^{57}\text{Co}$	$1.43 \times 10^{-5}$	$8.54 \times 10^{-6}$	$5.62 \times 10^{-6}$	$4.83 \times 10^{-6}$	$3.63 \times 10^{-6}$	$1.41 \times 10^{-6}$
$^{60}\text{Co}$	$6.7 \times 10^{-13}$	$2.45 \times 10^{-13}$	$1.17 \times 10^{-13}$	$1.43 \times 10^{-13}$	$2.6 \times 10^{-13}$	$3.60 \times 10^{-14}$
$^{56}\text{Ni}$	$1.51 \times 10^{-2}$	$4.52 \times 10^{-1}$	$6.0 \times 10^{-1}$	$7.4 \times 10^{-1}$	$8.17 \times 10^{-1}$	$9.95 \times 10^{-1}$
$^{57}\text{Ni}$	$5.39 \times 10^{-4}$	$1.14 \times 10^{-2}$	$1.60 \times 10^{-2}$	$1.91 \times 10^{-2}$	$2.29 \times 10^{-2}$	$2.82 \times 10^{-2}$
$^{59}\text{Ni}$	$2.84 \times 10^{-6}$	$3.3 \times 10^{-6}$	$2.89 \times 10^{-6}$	$1.46 \times 10^{-6}$	$1.84 \times 10^{-6}$	$4.30 \times 10^{-6}$
$^{63}\text{Ni}$	$5.43 \times 10^{-13}$	$3.93 \times 10^{-13}$	$2.12 \times 10^{-15}$	$1.34 \times 10^{-14}$	$4.1 \times 10^{-13}$	$2.97 \times 10^{-15}$

**Note.** Masses are in units of solar mass.

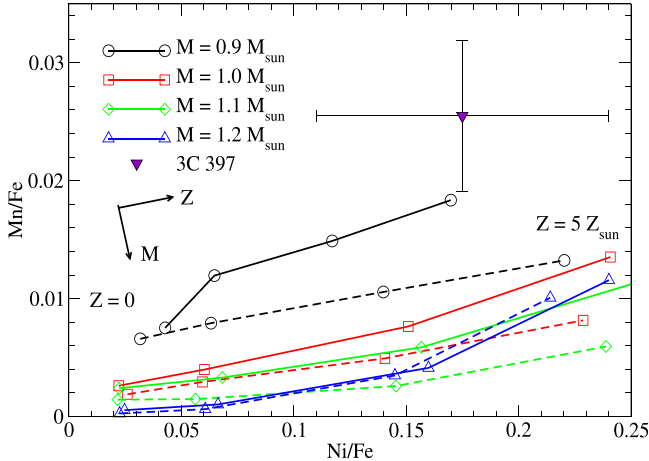


**Figure 27.** Mass ratio Mn/Fe against Ni/Fe for the sub-Chandrasekhar-mass models from  $M = 0.9, 1.0, 1.1,$  and  $1.2 M_{\odot}$ . The He envelope is fixed to be  $0.1$  (solid line) and  $0.2$  (dashed line)  $M_{\odot}$ . The metallicities are  $0, 1, 3,$  and  $5 Z_{\odot}$  for models on the same line from the left to right. The observational data point of the SNR 3C 397 is included. The typical mass and metallicity dependences of the models are shown by the arrows.

significant heating. On the other hand, the emitted  $e^{-}$  is completely absorbed by the surrounding matter. This means that one can trace its amount through its decay as a heat source in the light curve. In particular, the channels  $^{56}\text{Co} \rightarrow ^{56}\text{Ni}$  (half-life  $\approx 113$  days) and  $^{57}\text{Ni} \rightarrow ^{57}\text{Co}$  (half-life  $\approx 272$  days)

can be readily measured. In Graur et al. (2016), the  $B$ -band light curve of SN 2012cg is revisited at 900 days after the  $B$ -band maximum. It is shown that this SN Ia has a high  $^{57}\text{Ni}/^{56}\text{Ni}$  ratio at  $0.043 \pm {}^{+0.012}_{-0.011}$ , which is twice the corresponding solar ratio.

Figure 28 is similar to Figure 27, but for  $^{57}\text{Ni}$  against  $^{56}\text{Ni}$  for the same series of models and with this SN Ia. For models with an increasing metallicity,  $^{57}\text{Ni}$  production increases while  $^{56}\text{Ni}$  mildly decreases. This is because the initial electron fraction, as metallicity increases, deviates from the value of  $0.5$ , which most favors the production of  $^{56}\text{Ni}$  in NSE. On the other hand, the lowered electron fraction enhances production of  $^{57}\text{Ni}$ . Models with a thicker He envelope have higher  $^{56}\text{Ni}$  and  $^{57}\text{Ni}$  compared to models with the same mass but lower  $M_{\text{He}}$ . Similarly, for models with an increasing  $M$ , the  $^{56}\text{Ni}$  and  $^{57}\text{Ni}$  productions are enhanced as a result of higher central density, which allow more matter to be burnt until NSE for producing Fe-peak elements.

Then, we compare our results with this SN Ia. The data point of SN 2012cg is included. It can be seen that this SN has a rather high  $^{56-57}\text{Ni}$  as a healthy explosion. In our models, the high-mass models  $M = 1.2 M_{\odot}$  with high metallicity from  $3$  to  $5 Z_{\odot}$  are more likely to explain this data point. This is consistent with our previous work (Leung & Nomoto 2017, 2018; Nomoto & Leung 2017) that a high-metallicity model from  $1$  to  $5 Z_{\odot}$  with a central density from  $5 \times 10^8$  to  $1 \times 10^9 \text{ g cm}^{-3}$  may fit this observational data the best. However, compared to our Chandrasekhar-mass model, the sub-Chandrasekhar-mass models can fit the

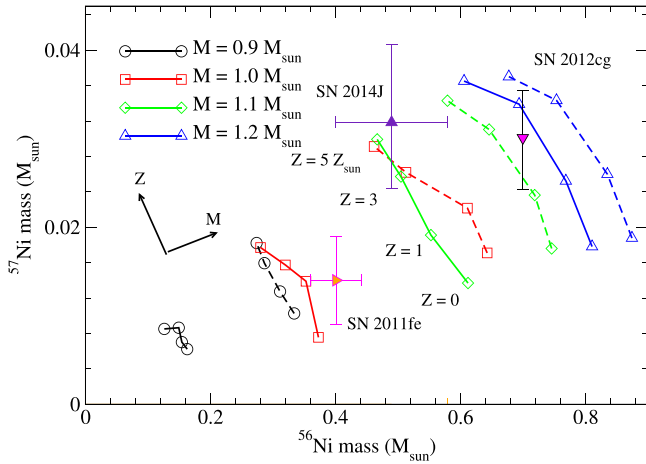


**Figure 28.**  $^{57}\text{Ni}$  against  $^{56}\text{Ni}$  for our sub-Chandrasekhar-mass models from  $M = 0.9, 1.0, 1.1,$  and  $1.2 M_{\odot}$ . The He envelope is fixed to be  $0.1$  (solid line) and  $0.2$  (dashed line)  $M_{\odot}$ . The metallicities are  $0, 1, 3,$  and  $5 Z_{\odot}$  for the model from bottom to top. The observational data points of SN 2011fe, SN 2012cg, and SN 2014J are included. The typical mass and metallicity dependences of the models are shown by the arrows.

upper range of this data point by models with  $M = 1.2 M_{\odot}$  and  $M_{\text{He}} = 0.1 M_{\odot}$  and fit the lower range of that by models with  $M = 1.1 M_{\odot}$  and  $M_{\text{He}} = 0.2 M_{\odot}$ . The trend derived here agrees with the estimation from the analytic formula as done in Graur et al. (2016) that the Chandrasekhar-mass model is preferred for this high  $^{57}\text{Ni}$  abundance. However, we also emphasized that the sub-Chandrasekhar-mass model is not excluded by this SN Ia as a physical picture. To further clarify its origin, future spectral study of the remnant, similar to the SNR 3C 397, will be necessary.

### 7.3. SN 2011fe

The third example comes from the well-observed SN 2011fe. This recent SN exploded on 2011 August 24 in the rather proximate Pinwheel galaxy (Nugent et al. 2011), which is situated 6.4 Mpc away (Shappee & Stanek 2011). The close distance of this SN Ia has attracted intensive study in different bandwidths (see Shappee et al. 2017 for the references therein) and spectral studies. This also allows detection of light curves beyond  $\sim 1000$  days. This provides more abundance constraints compared to the previous SN 2012cg. This SN Ia is first probed with the decay of  $^{55}\text{Fe}$  ( $^{55}\text{Fe} \rightarrow ^{55}\text{Mn}$  with a half-life of 999.67 days) directly. Through taking ratios with other decaying channels, they observe  $\log_{10}(^{57}\text{Co}/^{56}\text{Co}) = -1.62 \pm {}^{+0.08}_{-0.09}$ . In their best-fit model they also showed  $\log_{10}(^{55}\text{Fe}/^{57}\text{Co}) = -1.0 \pm {}^{+0.3}_{-0.5}$ .

Figure 29 is similar to Figure 28, but for the ratio  $^{55}\text{Fe}/^{57}\text{Co}$  against  $^{57}\text{Co}/^{56}\text{Ni}$  for our sub-Chandrasekhar-mass models and the observational data of SN 2011fe. Our models show a less uniform variation with increasing metallicity in the sub-Chandrasekhar-mass range. The variation is nonuniform at low metallicity ( $0-1 Z$ ). On the other hand,  $^{55}\text{Fe}/^{57}\text{Co}$  increases with metallicity, showing that the abundance of  $^{55}\text{Fe}$  is more sensitive to metallicity. It is expected, as shown in Figure 27, that the metallicity still plays an important role in the formation of stable Mn, which comes from the decay of  $^{55}\text{Fe}$ . The models tend to have a lower ratio when the He envelope becomes thicker. Also, when the total mass increases, the ratio is also suppressed. This is because the growth of  $^{57}\text{Ni}$ , which is very sensitive to the size of zone being burnt into NSE, is faster than that of  $^{55}\text{Fe}$ . The much faster growth of  $^{55}\text{Fe}/^{57}\text{Co}$  for the model  $M = 1.2 M_{\odot}$  and  $Z = 5 Z_{\odot}$  is again related to the enhancement of electron capture

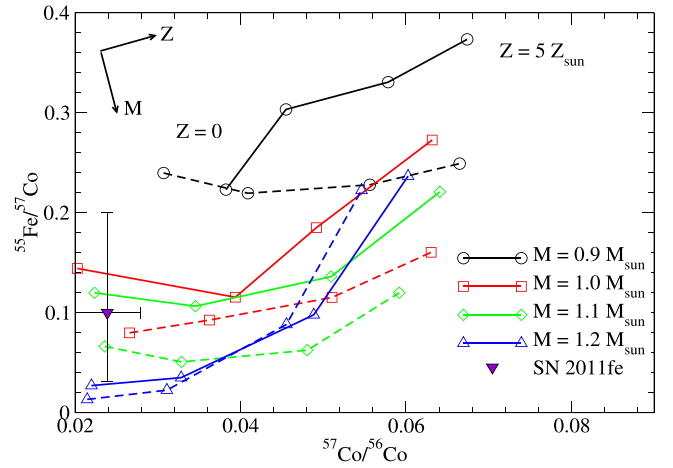


**Figure 29.**  $^{55}\text{Fe}/^{57}\text{Co}$  against  $^{57}\text{Ni}/^{56}\text{Co}$  for our sub-Chandrasekhar-mass models from  $M = 0.9, 1.0, 1.1,$  and  $1.2 M_{\odot}$ . The He envelope is fixed to be  $0.1$  (solid line) or  $0.2$  (dashed line)  $M_{\odot}$ . The metallicity includes  $0, 1, 3,$  and  $5 Z_{\odot}$ . The observational data point of the SN 2011fe is included. The typical mass and metallicity dependences of the models are shown by the arrows.

in the NSE region. The observational data point fits our model much better than the previous two models. It can be seen that a wide range of parameters can be used to explain this SN Ia. SN Ia models from  $M = 1.0-1.2 M_{\odot}$  and a low metallicity  $Z = 0-1 Z_{\odot}$  are adequate to fit in this observational data. This is also consistent with our previous work (Leung & Nomoto 2017, 2018; Nomoto & Leung 2017) that a low central density from  $5 \times 10^8$  to  $7.5 \times 10^8 \text{ g cm}^{-3}$  with a metallicity of  $0-1 Z_{\odot}$  can explain this data point using the turbulent deflagration model with DDT.

Recent late-time study of the light curve in the optical band has also revealed the  $^{57}\text{Ni}/^{56}\text{Ni}$  ratio of this SN Ia. By measuring the shift of late-time light curve after most  $^{56}\text{Ni}$  has decayed, the decay of  $^{57}\text{Ni} \rightarrow ^{57}\text{Co}$  can be another important radioactive source. In Dimitriadis et al. (2017), the pseudo-bolometric light curve is produced by combining data of the optical and near-IR bandwidth in the literature from 200 to 1600 days after explosion. It is shown that for this SN, albeit with significant systematic uncertainties,  $^{57}\text{Co}/^{56}\text{Co} = 0.031 \pm 0.011$ .

In Figure 28 we also plot this data point with our model sequences. The prediction of WD progenitor using the explosion product has been discussed for SN 2012cg in the previous section. Here we further apply this technique for SN 2011fe. The WD sequence with a mass of  $\approx 1.0 M_{\odot}$  and an He envelope of  $\approx 0.1 M_{\odot}$  can explain the observed  $^{57}\text{Ni}/^{56}\text{Ni}$  ratio. The data point can be best explained by the model with  $\sim Z_{\odot}$ .

We remark that, from the first sight, the SN 2011fe is very well explained by the sub-Chandrasekhar-mass model, in fact, in Leung & Nomoto (2017) and Nomoto & Leung (2017) we demonstrate that this SN Ia can also be explained by the Chandrasekhar-mass model in the high central density (high mass) limit with a metallicity close to  $Z_{\odot}$  in the centrally ignited model. This suggests that to further constrain the progenitor, future follow-up observations will be essential to measure the abundances of other isotopes or elements, similar to the analysis done for the SNR 3C 397.

### 7.4. SN 2014J

The fourth application of our models to the SN Ia observation is the candidate SN 2014J. This is an extremely well observed SN Ia owing to its vicinity. This SN Ia was

observed from a very early time since its rising light curve (Goobar et al. 2014). The multifrequency light curve and spectra are observed ranging from the infrared spectra (Telesco et al. 2015), optical photometry and spectrography (Ashall et al. 2014), ultraviolet (Foley et al. 2014; Brown et al. 2015), to gamma-ray light curve and spectra (Churazov et al. 2015; Diehl et al. 2015a, 2015b; Isern et al. 2016). This SN is interesting for its peculiar gamma-ray signals. It has an early gamma-ray signal coming from the decay of  $^{56}\text{Ni}$  at about 20 days after explosion, which is 10 days in advance of typical SNe Ia (Diehl et al. 2015b). The follow-up observation in its time-domain variations shows that it has a nonmonotonic variation in the  $^{56}\text{Co}$ -decay gamma-ray line. The Doppler shift analysis further shows the highly fluctuating Co-decay line frequency (Diehl et al. 2015a). Such features are argued to be originated from the He detonation and asymmetry in the detonation. The current work on the asymmetry double-detonation model appears to well match with this SN.

Here we try to constrain its progenitor from some of its observable by its  $^{57}\text{Ni}/^{56}\text{Ni}$  mass fraction ratio. This ratio has been applied to other SNe Ia, including the previous SN 2011fe and SN 2012cg. The late-time flattening of the late curve in the optical band is analyzed, from 277 to 1181 days after explosion. From the analysis of the late-time light curve (Yang et al. 2018), the mass ratio of  $^{57}\text{Co}/^{56}\text{Co} = 0.066 \pm_{0.008}^{0.009}$ . The ratio is even higher than SN 2012cg. By using the  $^{56}\text{Ni}$  derived from gamma-ray (Isern et al. 2016), where  $^{56}\text{Ni} = 0.49 \pm 0.09$ , we plot in Figure 28 the data point of SN 2014J.

From the figure we observe that the sub-Chandrasekhar-mass model can be capable of reaching the high Ni-isotope ratio at the high-metallicity end. Two of the model sequences can approach this observed data point, namely, when  $M = 1.1 M_{\odot}$  with  $M_{\text{He}} = 0.10 M_{\odot}$  and  $M = 1.0 M_{\odot}$  with  $M_{\text{He}} = 0.20 M_{\odot}$ . Both sequences require  $Z \approx 5 Z_{\odot}$  to reach the high mass fraction ratio. Again, the more massive He envelope is capable of producing the required  $^{56}\text{Ni}$ ; however, such early surface  $^{56}\text{Ni}$  can be very different from that produced through a standard Chandrasekhar-mass WD. In the latter case, the  $^{56}\text{Ni}$  is mostly produced by C detonation after deflagration–detonation transition. But it is always covered by another layer of IME when the detonation reaches the surface. As a result, the  $^{56}\text{Ni}$  decay is not directly visible, but it can be seen as a heat source in the light curve. On the other hand, with the He envelope, there is almost no shielding for the synthesized  $^{56}\text{Ni}$ ; therefore, it is expected that the early gamma-ray signal can be very different. We also note that such a massive He envelope with decaying  $^{56}\text{Ni}$  should show rather strong He lines.

We also compare the  $^{57}\text{Ni}/^{56}\text{Ni}$  ratio of SN 2014J with the Chandrasekhar mass models in Figure 20 of Leung & Nomoto (2018). We note that the Chandrasekhar mass models with  $Z \approx 3\text{--}5 Z_{\odot}$  produces the observed high  $^{57}\text{Ni}/^{56}\text{Ni}$  ratio.

## 8. Summary

In this paper, we study the hydrodynamics and associated nucleosynthesis of sub-Chandrasekhar-mass models for SNe Ia, where the C detonation is triggered by the surface He detonation of a symmetric or an asymmetric structure. Such a double detonation can occur in both the SD and DD scenarios. Our findings are summarized as follows.

- (1) We find that whether C detonation triggered is strongly sensitive to the He detonation pattern. We consider four

possible structures: namely, one-bubble, one-ring, bubble-and-ring, and spherical, in view of the unresolved, inner fluid motion of the He shell before nuclear runaway. The He detonation with higher symmetry (one-ring and spherical structures) can result in geometric convergence, which can very robustly heat up the C fuel to the ignition temperature for the subsequent temperature. He detonation with lower symmetry (one-bubble) requires a more massive He envelope ( $>0.1 M_{\odot}$ ) to trigger the second explosions. The case with multiple bubbles depends on how the shock wave propagates inside the WD.

- (2) We carry out a parameter survey on the nucleosynthesis for the sub-Chandrasekhar-mass WD models with different model parameters. We perform two-dimensional hydrodynamical simulations using our own SN simulation code from the onset of the He detonation until all detonations quench by the expansion. The following parameters are studied: the metallicity, He envelope mass, total mass, the initial He detonation, and the initial C/O mass fraction ratio. We pay attention to some representative elements, including intermediate-mass elements (e.g., Si, S, Ar, and Ca), light iron-peak elements (Ti, V, and Cr), and other iron-peak elements (Mn, Fe, Co, Ni). These elements are strongly sensitive to the total mass, metallicity, and He envelope mass, but less sensitive to the initial He detonation and C/O mass fraction ratio. Metallicity affects mostly the low- $Y_e$  isotopes, e.g.,  $^{55}\text{Mn}$  and  $^{58}\text{Ni}$ . He envelope mass affects light iron-peak elements, especially  $^{48}\text{Ti}$ ,  $^{50,51}\text{V}$ , and  $^{52}\text{Cr}$ . Total mass affects  $^{56}\text{Ni}$  and hence the mass fraction  $[X_i/^{56}\text{Fe}]$  with respect to the Sun.
- (3) We also compare our two-dimensional models with the classical spherical double-detonation model and show that the chemical signature due to asphericity is very significant. The aspherical detonation can create hot spots that produce a distinctive abundance pattern in intermediate-mass elements and light iron-peak elements (Ti, V, and Cr). Explosion of a progenitor with a mass of  $\sim 1.1\text{--}1.2 M_{\odot}$  may help distinguish in the future the degeneracy of the SD and DD scenarios. However, an exact matching with the observed  $^{56}\text{Ni}$  distribution will also require the stellar initial mass function. We further show that the sub-Chandrasekhar-mass WD models cannot substitute the Chandrasekhar-mass one because of the persistent insufficiencies of Mn production. The final  $[\text{Mn}/\text{Fe}]$  can be 0.4 dex lower than the model using the Chandrasekhar-mass WD model. We provide corresponding yield tables for the applications to the galactic chemical evolution.
- (4) We apply our models to provide constraints on some well-observed SNe Ia, including SN 2012cg, SN 2011fe, SN 2014J, and SN Ia remnant 3C 397. The probable progenitor configurations are implied based on the derived chemical abundance of some Fe-peak isotopes. We used the late-time light curve to indicate the  $^{57}\text{Ni}/^{56}\text{Ni}$  ratio. We find that SN 2014J can resemble the sub-Chandrasekhar-mass model at  $1.0\text{--}1.1 M_{\odot}$  with metallicity  $Z = 3\text{--}5 Z_{\odot}$ . (Note that the Chandrasekhar mass models also resemble SN 2014J if  $Z = 3\text{--}5 Z_{\odot}$ .) SN 2011fe can be explained by models with  $M \sim 1.0 M_{\odot}$  with near  $Z_{\odot}$ . SN 2012cg can be approached by models with  $M = 1.1\text{--}1.2 M_{\odot}$  at  $Z = 1\text{--}3 Z_{\odot}$ . For SNR 3C 397, the high Mn/Ni ratio cannot resemble any of our current sub-Chandrasekhar-mass models. The Mn/Fe ratios in our



models are much lower than the observed value. Only models at the lower-mass end ( $0.9 M_{\odot}$ ) with  $Z = 5 Z_{\odot}$  can approach the observed data point.

- (5) The hydrodynamical structures and nucleosynthesis profiles provide useful predictions for future observations of elemental abundances and line  $\gamma$ -rays.

This work has been supported by the World Premier International Research Center Initiative (WPI) and JSPS KAKENHI grant No. JP17K05382. S.C.L. acknowledges support from grant HST-AR-15021.001-A.

We thank the anonymous referee for the very detailed and helpful suggestions to improve the manuscript.

We thank Frank Timmes for his open-source microphysics subroutines, including the Helmholtz equation of state and the *torch* subroutine for the post-process nucleosynthesis. We also thank Ken Shen for the ideas in the numerical modeling of the detonation physics. We thank Amanda Karakas and Chiaki Kobayashi for the information about the galactic stellar abundances. Finally, we thank Roland Diehl and Jordi Isern for the inspiring discussion about SN 2014J.

## Appendix A

### Determination of the He Detonation Timescale

In Section 2 we mentioned that simplified schemes for C and He detonation are used. In this section, we describe in more detail how they are implemented. Unlike C detonation, He detonation in the sub-Chandrasekhar-mass WD scenario occurs at a much lower density ( $\sim 10^4$ – $10^7 \text{ g cm}^{-3}$  in the He envelope). The low density, as well as the nondegenerate property of the electron gas, leads to a lower final temperature, after all He is burnt. As a result, it becomes important to estimate more precisely how much He is burnt in the reaction zone and in the post-reaction zone. In particular, we are interested to know how He is burnt as a function of time, which is used to calibrate the amount of energy released by the detonation.

We calculate the detonation structure following the numerical scheme described in Sharpe (1999). Here we give a brief summary about this method. In general, detonation consists of three sections, the pre-shock region, the reaction zone, and the post-reaction region. We assume at every point inside the detonation wave that thermodynamics equilibrium is maintained, such that the specific internal energy  $\epsilon$  and pressure  $p$  are related by the thermodynamics input including the density  $\rho$ , temperature  $T$ , and the number fraction of each isotope  $Y_i$  ( $i = 1, N$ ) in a network with  $N$  isotopes. Therefore,

$$\Delta\epsilon = \frac{\partial\epsilon}{\partial\rho}|_{T,X_i} + \frac{\partial\epsilon}{\partial T}|_{\rho,Y_i} + \sum_i \frac{\partial\epsilon}{\partial Y_i}|_{\rho,T}. \quad (4)$$

The steady-state Euler equation can be written as

$$\frac{d\rho}{dx} = -\frac{\rho a_f^2}{v} \frac{\sigma \cdot \mathbf{R}}{l}, \quad (5)$$

$$\frac{dT}{dx} = \left(\frac{\partial p}{\partial T}\right)^{-1}_{\rho,X} \left\{ \left[ u^2 - \left(\frac{\partial p}{\partial \rho}\right)_{T,X} \right] \frac{d\rho}{dx} - \sum_{i=1}^N \left(\frac{\partial p}{\partial X_i}\right)_{\rho,T,X_{j \neq i}} \frac{dX_i}{dx} \right\}, \quad (6)$$

$$\frac{dX_i}{dx} = \frac{R_i}{A_i v}, \quad (7)$$

where

$$\eta = a_f^2 - v^2 \quad (8)$$

is the sonic parameter,  $A_i$  is the atomic mass for the  $i$ th isotope,

$$a_f^2 = \left(\frac{\partial p}{\partial \rho}\right)_{T,X} + \left[ \frac{p}{\rho^2} - \left(\frac{\partial \epsilon}{\partial \rho}\right)_{T,X} \right] \times \left(\frac{\partial p}{\partial T}\right)_{\rho,T} \left(\frac{\partial \epsilon}{\partial T}\right)^{-1}_{\rho,X} \quad (9)$$

is the sound speed of constant composition (also known as frozen sound speed in the literature of detonation), and

$$\sigma_i = \frac{1}{\rho a_f^2} \left\{ \left(\frac{\partial p}{\partial X_i}\right)_{\rho,T,X_{j \neq i}} - \left(\frac{\partial p}{\partial T}\right)_{\rho,X} \left(\frac{\partial \epsilon}{\partial T}\right)^{-1}_{\rho,X} \times \left[ \left(\frac{\partial \epsilon}{\partial X_i}\right)_{\rho,T,X_{j \neq i}} - \left(\frac{\partial q}{\partial X_i}\right)_{X_{j \neq i}} \right] \right\} \quad (10)$$

is the thermicity constant, such that  $\sigma \cdot \mathbf{R}$  is the thermicity. In integrating this set of differential equations, we use the boundary conditions at  $x = 0$ ,  $\rho = \rho_i$ ,  $T = T_i$ ; at  $x \rightarrow \infty$ ,  $\rho = \rho_f$ ,  $T = T_f$  and  $X = X_f$  with thermicity = 0. Notice that  $\rho_i$ ,  $T_i$ , and  $Y_i$  are the quantities after shock. They are related to the pre-shock quantities ( $\rho_0$ ,  $T_0$ ,  $X_0$ ) by

$$\rho_0 D = \rho_i c_s, \quad (11)$$

$$\rho_0 D^2 = \rho_i c_s^2, \quad (12)$$

$$\rho_0 D^2 + \rho_0 \epsilon_0 + P_0 = \rho_i \epsilon_s^2 + \rho_i \epsilon_i + P_i. \quad (13)$$

$D$ ,  $c_s$ , and  $P_0$  are the pre-shock matter density, speed of sound, and pressure of the pre-shock matter, respectively.

In Figure 30, we plot the density, temperature, and chemical isotope profiles for a detonation wave at a density of  $10^6 \text{ g cm}^{-3}$ . To trigger the first incineration, the matter is assumed to be shock-heated to a temperature of  $\sim 2 \times 10^9 \text{ K}$ . Before  $10^{-4} \text{ s}$ , the temperature does not rise considerably. Also, there is only a very subtle drop in the density. There is also a slow change in the chemical composition from  $^4\text{He}$  to  $^{12}\text{C}$ . At  $\sim 10^{-4} \text{ s}$ , the temperature rises drastically from  $2 \times 10^9 \text{ K}$  to  $3 \times 10^9 \text{ K}$ . The density also drops by  $\sim 30\%$ . We can see isotopes from  $^{12}\text{C}$ ,  $^{40}\text{Ca}$ ,  $^{48}\text{Ti}$ , and  $^{52}\text{Fe}$  burst out one by one around  $10^{-4} \text{ s}$ . This means that even at low temperature, the  $\alpha$ -chain reaction can proceed efficiently, once the triple- $\alpha$  reactions have provided the first fuel for the subsequent reactions. Beyond  $4 \times 10^{-4} \text{ s}$ , the productions of other isotopes are suppressed again, except  $^{56}\text{Ni}$ . At that time,  $^4\text{He}$  is stably burnt into  $^{56}\text{Ni}$ , causing the temperature (density) to grow (drop) to its equilibrium value. At  $\sim 1 \text{ s}$ , the temperature and density reach their equilibrium at  $3.6 \times 10^9 \text{ K}$  and  $4.6 \times 10^6 \text{ g cm}^{-3}$ .

In Figure 31, we plot the temperature, density, and isotope abundance profiles for pure He fuel at an initial density of  $10^7 \text{ g cm}^{-3}$ . With a high density, nuclear reactions can take place spontaneously. In the first  $10^{-4} \text{ s}$ , temperature increases quickly

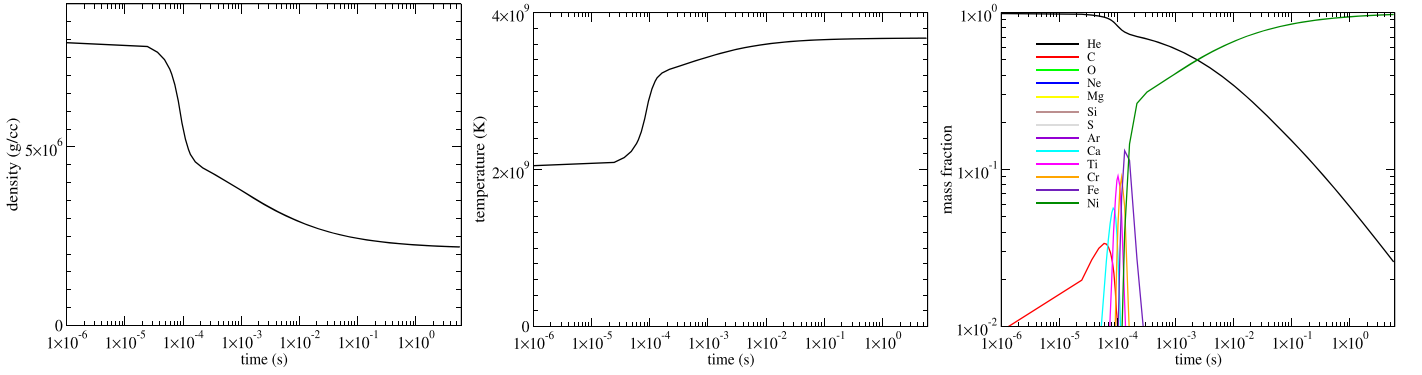


**Figure 30.** Left: density evolution of He during detonation for pure He fuel at a density  $10^6 \text{ g cm}^{-3}$ . The matter is assumed to be shock-heated to above  $2 \times 10^9 \text{ K}$ . Middle: temperature evolution of the detonation wave at an initial density of  $10^6 \text{ g cm}^{-3}$ . Right: isotope evolution of the detonation wave at an initial density of  $10^6 \text{ g cm}^{-3}$ .

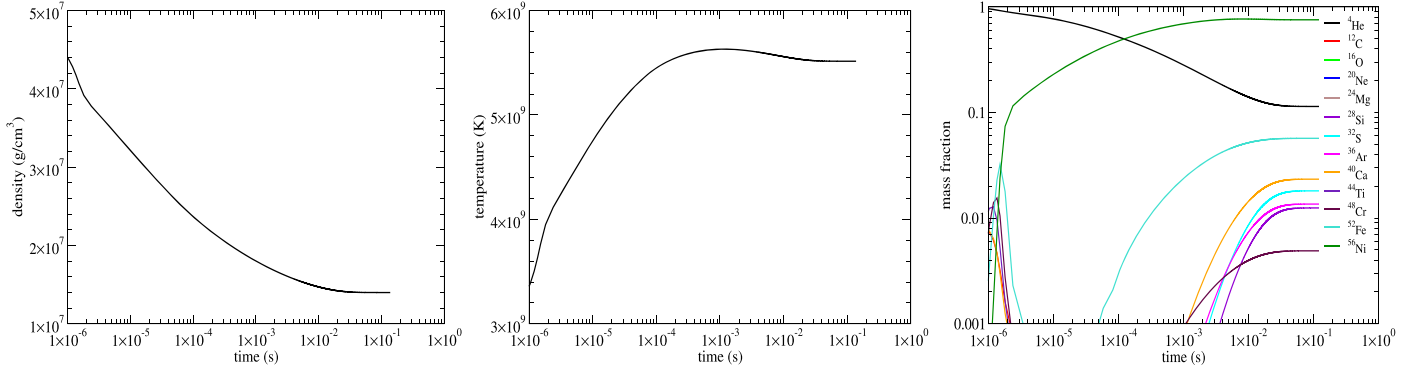


**Figure 31.** Left: density evolution of He during detonation for pure He fuel at a density of  $10^7 \text{ g cm}^{-3}$ . The matter is assumed to be shock-heated to above  $2 \times 10^9 \text{ K}$ . Middle: temperature evolution of the detonation wave at an initial density of  $10^7 \text{ g cm}^{-3}$ . Right: isotope evolution of the detonation wave at an initial density of  $10^7 \text{ g cm}^{-3}$ .

from  $3 \times 10^9 \text{ K}$  to  $6 \times 10^9 \text{ K}$ , while the density drops from  $4 \times 10^7 \text{ g cm}^{-3}$  to  $\sim 2 \times 10^7 \text{ g cm}^{-3}$ . The initial peaks for various isotopes except  $^{56}\text{Ni}$  can be found in the first  $10^{-6} \text{ s}$ , while the conversion of  $^4\text{He}$  to  $^{56}\text{Ni}$  can be found in the first  $10^{-4} \text{ s}$ . After that, the temperature and density start to converge to their asymptotic values at  $\sim 5.5 \times 10^9 \text{ K}$  and  $1.4 \times 10^7 \text{ g cm}^{-3}$ . At the same time, the temperature is sufficiently high that NSE emerges.  $^{52}\text{Fe}$ ,  $^{40}\text{Ca}$ ,  $^{48}\text{Cr}$ ,  $^{36}\text{Ar}$ , and  $^{32}\text{S}$  form one by one and reach their equilibrium value at  $\sim 0.1 \text{ s}$ .

By comparing the two sets of results, we can see that in the density range related to the sub-Chandrasekhar-mass double-detonation models, the time necessary for He to completely release its energy into the system increases by two orders of magnitude when the density drops from  $10^7$  to  $10^6 \text{ g cm}^{-3}$ . (In the simulations we find that the typical time step has a size of  $\sim 10^{-4}$ – $10^{-3} \text{ s}$ , depending on the global velocity distribution.) Therefore, especially for the He near the surface, once they are burnt, they expand drastically, making their local density much lower than those underneath. As a result, their energy release process is incomplete. To mimic this effect, we use a density-dependent timescale  $\tau_{\text{He}}(\rho)$ , which is calibrated by the detonation waves as demonstrated above. The timescale corresponds to the time when 90% of energy is released with respect to its equilibrium value. To establish the relation  $\tau_{\text{He}}$ , we repeat the above process for He detonation waves at different initial densities. Then, we collect the necessary timescale by the above detonation. A simple power-law fitting provides us with the

following formula:

$$\tau_{\text{He}} = 1.72 \times 10^{-6} \left( \frac{\rho}{10^8 \text{ g cm}^{-3}} \right)^{-2} \text{ s}. \quad (14)$$

In the simulations, when the current time step  $\Delta t > \tau_{\text{He}}$ , complete burning is assumed. Otherwise, only the fraction of matter  $\Delta t/\tau_{\text{He}}$  is assumed to release its energy. We have only considered the effect of density because the reaction rate is very sensitive to the input temperature. Below the ignition temperature ( $\sim 10^9 \text{ K}$ ), the reactions are so slow that the burning timescale is much longer than the dynamical timescale, which means that no detonation can be formed. On the other hand, above the ignition temperature, the fuel burns instantaneously. Also, the energy generated by the nuclear reaction is much larger than the different choices of input temperature. Thus, the product of the detonation wave is less insensitive to the input temperature compared to the density.

Certainly a self-consistent way, which is to calculate the network directly, can provide us with the most accurate results regarding the process of partial burning. However, such inclusion is beyond the current capability of our computing resources. Furthermore, in the hydrodynamics, acoustic waves are found everywhere inside the star. These waves cause fluctuations in the local temperature. These fluctuations increase the computation time significantly when a complete network is used, since the nuclear composition always adjusts

itself to the local temperature, where at high temperature the typical time step is small.

### Appendix B Effects of Symmetry Boundary

In this work we have carried out simulations of sub-Chandrasekhar SNe Ia in a quadrant of sphere. This uses a reflective boundary along the symmetry plane  $z = 0$ . As a result, the initial He detonation configuration, namely, a one-bubble structure, corresponds to two synchronous ignitions of He detonation, one at the “north” pole and one at the “south” pole. It is unclear, prior to the runaway of He, how the velocity field, especially the turbulent velocity motion, may perturb the initial ignition of He. Certainly it is more likely for two He detonation bubbles to have asynchronous ignition times, or even that there is only one ignition before C detonation is triggered. Therefore, it is unclear whether the C detonation can still be robustly triggered when there is a time lapse between the two He detonation bubbles.

To do the comparison, we develop a temporary extension of our hydrodynamics code to model the hemisphere of the WD by relaxing the reflection symmetry. We place one He bubble at the “north” pole and another one at the “south” pole, with some time delay. In Table 2 we tabulate the configuration and initial detonation properties of our test models. It can be seen that all the cases give a positive response to the He detonation, regardless of being one or two He bubbles, and their delay time. This suggests that as long as the He envelope has exceeded the marginal thickness, then the shock compression, either by shock–shock collision or by shock–wall collision, can create similar heating to the surface matter of the CO core.

We carry out five hydrodynamics simulations to extract the effects of reflection symmetry. Test-QS corresponds to the model with reflection symmetry, where we choose the same configuration as the benchmark model 110-100-2-50. This means that the Model Test-QS is exactly the benchmark model. Models Test-HS-0–Test-HS-3 do not assume reflection symmetry and have an He ignition delay time from 0 to 1 s. Model Test-HS-0 acts as a control test to see whether the hemisphere extension is consistent with a quadrant sphere modeling, whereas in Model Test-HS-3 we delay the second ignition so long that the C detonation is triggered. From Table 2, when the delay time becomes larger, the position of the C detonation moves away from the “equator,” since the upper He bubble has

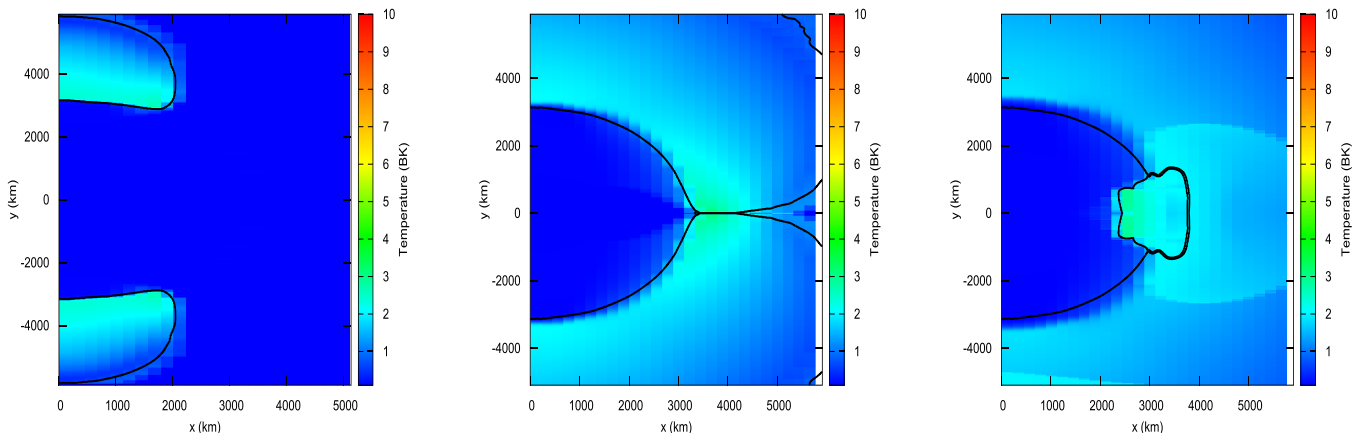
more time to propagate before the shock collision. However, no significant change in the trigger density and temperature is observed, showing that the trigger of C detonation does not depend strongly on the minor details of the He detonation.

In Figure 32 we plot the temperature color plots with the He and C detonation structure at 0.5 s, at the trigger of C detonation and 0.2 s after the trigger of C detonation, respectively, for the Model Test-HS0. The detonation structure of both He and C demonstrates a high degree of symmetry throughout the simulation. The detonation occurs at the equator around the surface of the CO core. The reflected shock leads to a clear distinction between the pre-heated region and post-heated region. From Table 2, it can be seen that when the two He detonations are placed explicitly, the C detonation is triggered along the “equator” of the WD at the same time as Model Test-QS. However, slight differences in density and temperature appear between the grid positions in the quadrant of sphere and hemisphere. They are different that in the Test-QS no grid is placed on the reflection plane while an explicit grid is put on the reflection place in the Model Test-HS-0. As a result, it allows an explicit compression of matter on the equator when the two shocks merge.

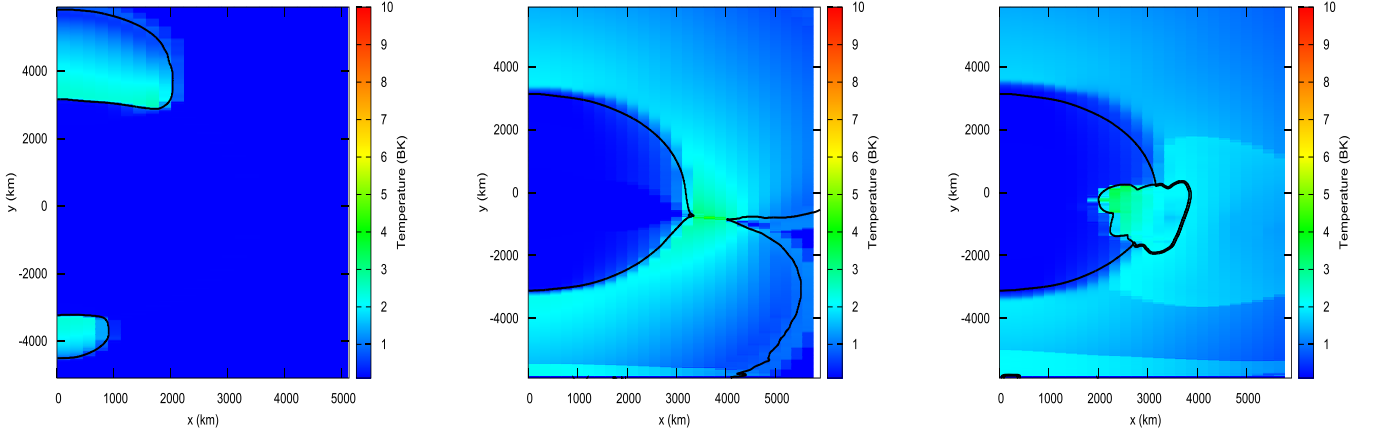
Figure 33 is similar to Figure 32, but for Model Test-HS-1. Due to the delayed He detonation, the area swept up by the upper He detonation wave has a larger volume than the lower one. As a result, the collision point is lower. Despite that, the collision point remains the hottest point that can trigger C detonation. Due to the asymmetric expansion of the star, the detonation in the CO core has more features compared to the previous case.

Figure 34 is similar to Figure 32, but for Model Test-HS-2. The further delayed second He detonation bubble allows the collision to occur at an even lower position. The newly formed C detonation can propagate as in previous cases. The shock reflection in the He envelope can be clearly seen.

Figure 35 is similar to Figure 32, but for Model Test-HS-3. We delayed putting in the second detonation so long that the C detonation has been triggered beforehand. In this case, it is identical to the one-bubble scenario where the shock convergence at the “south” pole of the He envelope creates the desired shock compression and penetration into the CO core, which heats up sufficiently the fuel for spontaneous runaway. The geometrical convergence around the “south” pole allows the shock to be strengthened with an increasing



**Figure 32.** He and C detonation structure and the temperature color plot of Model Test-HS-0 at 0.5 s, at the trigger of C detonation and at 0.2 s after the C detonation trigger.



**Figure 33.** Similar to Figure 32, but for Model Test-HS1 at 0.5 s, at the trigger of C detonation and at 0.2 s after the C detonation trigger.

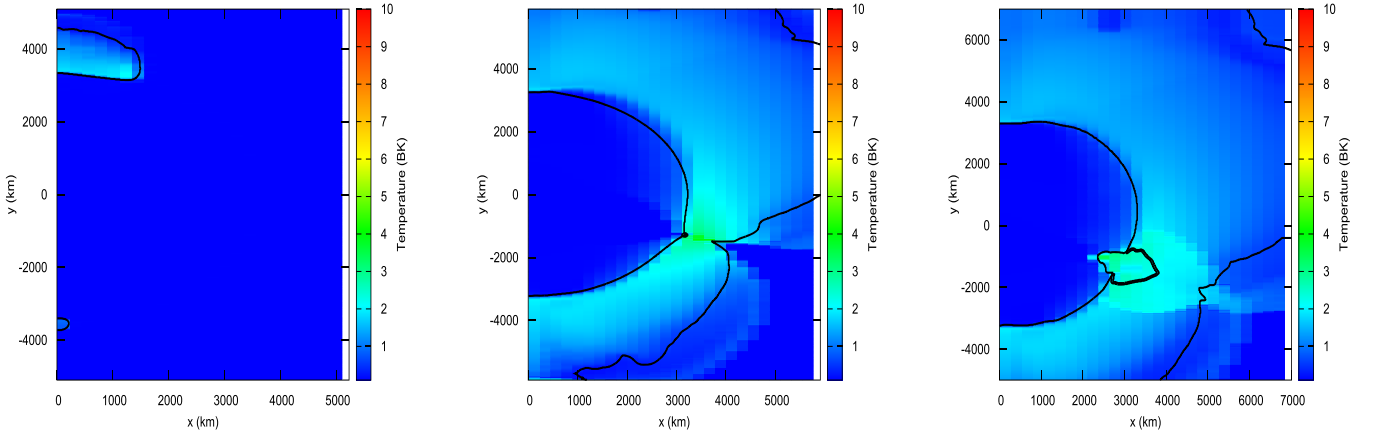


**Figure 34.** Similar to Figure 32, but for Model Test-HS2 at 0.5 s, at the trigger of C detonation and at 0.1 s after the C detonation trigger.

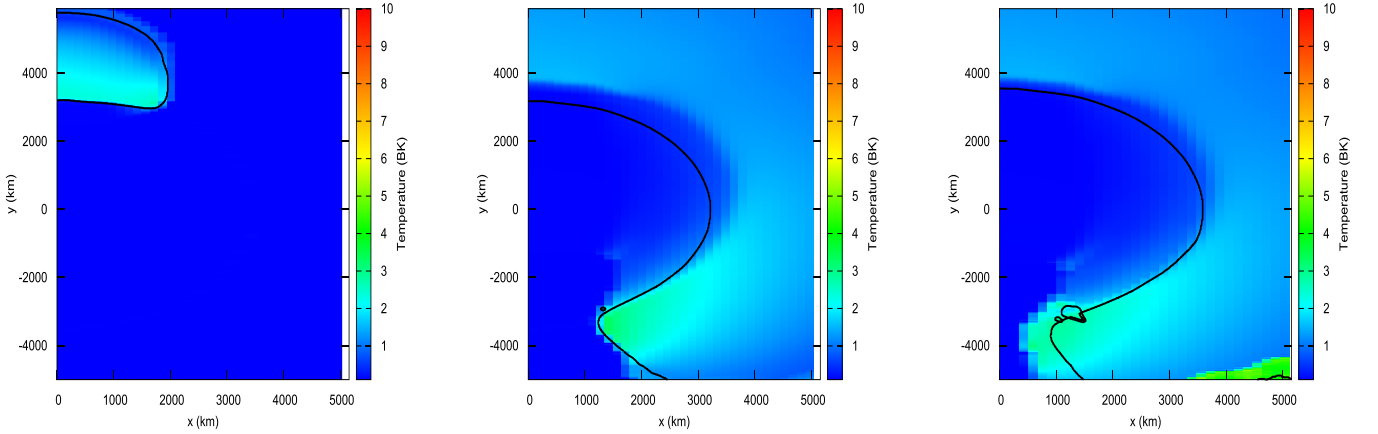


**Figure 35.** Similar to Figure 32, but for Model Test-HS-3 at 0.5 s, at the trigger of C detonation and at 0.075 s after the C detonation trigger.

post-shock temperature when it approaches the rotation axis. The temperature is already adequately high to trigger the C detonation before the He shock collides with the axis. The triggered C detonation can then propagate inside the CO core.

From all four cases it suffices to demonstrate that the C detonation can be ignited by He detonation, and the reflection symmetry of the  $z = 0$  plane can provide the necessary shock collision for shock compressing the fuel in order to raise its temperature for spontaneous nuclear runaway. Even without

the symmetry plane, we demonstrated that the collision of He detonation, regardless of their ignition time, will also provide the necessary shock heating on the CO core surface. We also presented that in the one-bubble limit, i.e., the delay time much greater than the C detonation time, the geometric convergence in the models can also provide the required shock compression. This suggests that as long as the He envelope mass is large enough for triggering C detonation naturally, the configuration of He detonation plays a less important role for the detonation

structure. Since in these tests we only aim at showing the robustness of triggering the C detonation with or without reflection symmetry, the complete nucleosynthesis and the effects of shock collision on the nuclear burning will be left as future work. However, it remains unclear whether the WD can be represented comprehensively by a sphere in hydrostatic equilibrium prior to its runaway. The effects of a nonstatic atmosphere, as a result of He burning before its runaway, will be an interesting future work to further test the robustness of the C detonation mechanism by bubbles.

### Appendix C

#### Test 1: Resolution Study in the Propagation of Detonation

In the main text we have studied extensively how each of the model parameters contributes to the diversity of chemical composition. However, besides the chemical composition, which should be compatible with solar composition, the simulation results should be convergent with respect to different resolution. Here we examine in more detail how our models depend on the choice of resolution.

The first test is done to a static CO core with an He envelope as in our benchmark model. We choose the same configuration same as in Model 110-100-2-50 except for the initial He detonation. We put a spherical C detonation with a radius of 100 km at the beginning and allow it to propagate. The spherical detonation will preserve mostly its symmetry and propagate. Thus, it is literally a one-dimensional problem. But we remark that it is still a two-dimensional problem because in cylindrical coordinates the spherical structure is broken down to  $r$ - and  $z$ -components along the constant radius contour.

We put the model parameters and the explosion energetics including thermodynamics information in Table 3. We choose the standard resolution at 15 km, which is the same as in the main text. A coarser model with a resolution of 30 km and a finer model with that of 7.5 km are prepared in a similar manner. We can see that when the resolution increases, global quantities such as the explosion energy and burning time converge, though it does not follow the exact scaling used in the spatial discretization scheme. The local quantity, i.e., the

global maximum temperature, shows a much slower convergence rate. Despite that, the three models show a decreasing relative change, showing that the results are on the convergence side.

In Figure 36 we plot the time evolution of the central temperature, total energy, and total burnt mass for the three test models. All three models show an initial peak at  $t = 0.1$  s because of the shock imposed by the initial detonation. The peak temperature increases when resolution decreases. A typical change of 5% increase is observed when  $\Delta x$  drops by half. After that, the star gradually expands and the star cools down. The models with a lower resolution have a lower peak temperature. Our code shows linear convergence in the temperature. This is because the smaller the grid size it has, the closer it is to the  $1/r$  divergence when the shock converges. The cooling rate of the central grid also depends on the resolution. The model with a smaller resolution cools faster, and the change of temperature shows a linear dependence. A 5% difference can be seen at the central  $t = 0.4$  when resolution reduces by half.

The total energy and its energy generation are also dependent on the spatial resolution. The total energy includes the kinetic, internal, and gravitational energy. The energy growth and its final energy are also weakly dependent on the spatial resolution. Models with a higher resolution have a faster energy growth and higher final energy. The relative difference is  $\sim 1\%$  when resolution reduces by half. This suggests that when  $\Delta x$  decreases, the level set can capture the front surface with more details, which increases its surface area. As a result, the detonation can effectively propagate faster and release more energy, while the star has less time to expand before it is swept up by the detonation wave.

The total burnt mass shows how much mass is swept up by the detonation wave. It has a similar trend to the total energy, but the result is independent of the energy production algorithm. The models shows a larger and weaker scaling relation for different  $\Delta x$ . A smaller  $\Delta x$  gives a lower time for the detonation wave to complete burning the whole star. A difference of  $\sim 10\%$  is observed.

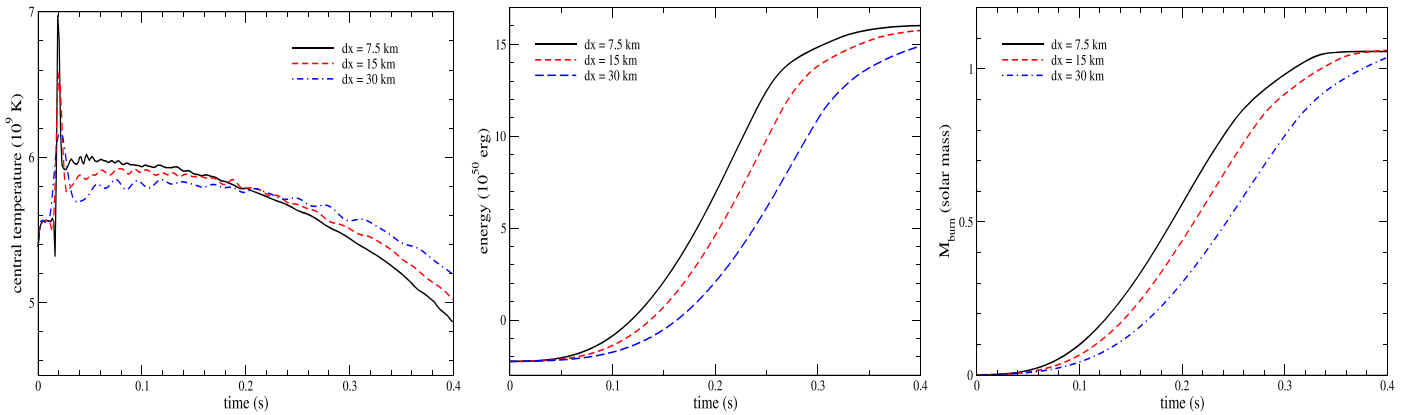


**Figure 36.** Left: time evolution of the central temperature for Models Test1-fine ( $\Delta x = 7.5$  km), Test1 ( $\Delta x = 15$  km) and Test1-coarse ( $\Delta x = 7.5$  km). Middle: similar to the left panel, but for the total energy. Right: similar to the left panel, but for the total burnt mass.



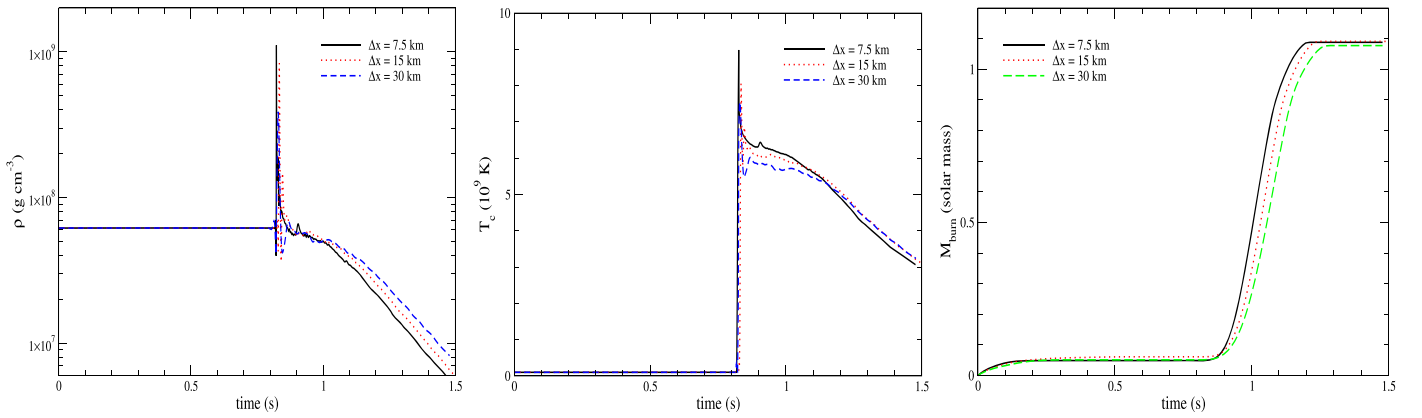


**Figure 37.** Left: time evolution of the central temperature for Models Test2-fine ( $\Delta x = 7.5$  km), Test2 ( $\Delta x = 15$  km) and Test2-coarse ( $\Delta x = 30$  km). Middle: similar to the left panel, but for the central density. Right: similar to the left panel, but for the total burnt mass.

## Appendix D

### Test 2: Resolution Study of Shock Convergence

In this test we study how the choice of spatial resolution affects the convergence of detonation shock. Geometric convergence exists in both C and He detonation in different manners. For C detonation, we have showed that “X”-type detonation (such as Model 110-100-2-50 (X)) can result in the first C detonation along the symmetry axis. This detonation later propagates to the center. But in the three-dimensional projection, it corresponds to a C-detonation ring shrinking into a point. Similarly, the “S”-type detonation (such as Model 100-050-2-S50 (S)) can result in a spherical shock propagating toward the center. For He detonation, a similar phenomenon occurs in the “Y”-type detonation such as Model 110-050-2-B50 (Y). The geometric convergence occurs when the He detonation propagates from the convergence. However, the discontinuity is described numerically in the discretized manner by the Eulerian meshes. As a result, the local thermodynamics behavior at the point of convergence can depend strongly on the spatial resolution.

To study how the geometric convergence of shock depends on the simulation, we repeat the simulations for Model 110-050-2-S50 (S) at a spatial resolution  $\Delta x$  of 7.5, 15, and 30 km. We remind that  $\Delta x = 15$  km is the default resolution. We set up a WD with an  $M = 1.1 M_{\odot}$  and  $M_{\text{He}} = 0.05 M_{\odot}$  at  $Z = Z_{\odot}$ . The initial He detonation is spherical at 30 km away from the CO core. We use the spherical He detonation near the CO core interface. Then, we allow the He detonation to propagate and trigger the inward-propagating shock. The shock converges at the stellar core and triggers the C detonation, which propagates outward. In Table 4 we tabulate the parameters necessary for this resolution study.

In the left panel of Figure 37 we plot the evolution of central density for the three tests. The density is an important quantity not only because it is the essential part in the Euler equation but also because the energy production frequently refers to density as the input parameter. In the figure, the central density has its peak at  $t \sim 0.8$  s. This corresponds to the moment when the spherical shock arrives at the center of the star. The peak value can increase from  $4 \times 10^8$  up to  $10^9 \text{ g cm}^{-3}$  when resolution increases. Again, this suggests that the code obtains a weakly converging result when describing the local properties in the center.

The middle panel of Figure 37 is similar to the left panel, but for the central temperature. The central temperature can be

important especially when it is related to the burnt matter because it controls the NSE process and the electron capture process. The central temperature can increase from  $7 \times 10^9 \text{ K}$  to  $9 \times 10^9 \text{ K}$  for the three models here. Again, smaller  $\Delta x$  allows a faster drop in the central temperature. The sequence does not show a convergent trend. Despite that, we remind that the smaller the resolution we have, the smaller contribution the divergent result to the whole system is.

In the right panel of Figure 37 we plot the burnt mass against time. There is no significant burning at the beginning since only He is burnt. After  $t = 0.9$  s, the detonation wave begins to sweep across the fuel efficiently. Again, it shows a weakly converging sequence that a smaller  $\Delta x$  allows faster burning of material. A reduction by 5% by mass of the whole star to be completely burnt is observed, when resolution drops by half. This shows that, even if the local quantities can rely on  $\Delta x$ , the finer  $\Delta x$  is, the smaller contribution for an individual cell to the global system, especially the one that the center cell gives. As a result, the resolution-dependent feature is averaged out in general.

## Appendix E

### Test 3: Resolution Study of C-detonation Trigger

In this test we study how the choice of spatial resolution affects the convergence of shock in the trigger of second (C) detonation. In the simulation, similar to the previous test, the geometric convergence plays an important role for creating the necessary hot spot, if the initial He detonation possesses certain symmetry in space. For example, we choose to study Model 110-100-2-3R50 (N). This is because, by comparing Models 110-100-2-50 (X), 110-100-2-2R50 (Y), and 110-100-2-3R50 (N), they do not show a regular trend in the detonation pattern. Also, given the fact that Model 110-100-2-50 (X) can trigger the second detonation, with more initial He being burnt at the beginning, Model 110-100-2-3R50 should be more probable to be ignited. Therefore, it becomes interesting to question whether the choice of resolution plays a role.

To test the validity of our result, we also perform a convergence study for Model 110-100-2-3R50 (N) at three resolutions of 7.5, 15, and 30 km. In Table 5 we list the configurations for these three models. Again, 15 km is the default simulation size used in our calculation. We set up the same initial model with a total mass of  $1.1 M_{\odot}$  and He mass of  $0.1 M_{\odot}$  at solar metallicity. The initial detonation is a three-bubble structure located along the rotation axis, symmetry axis,

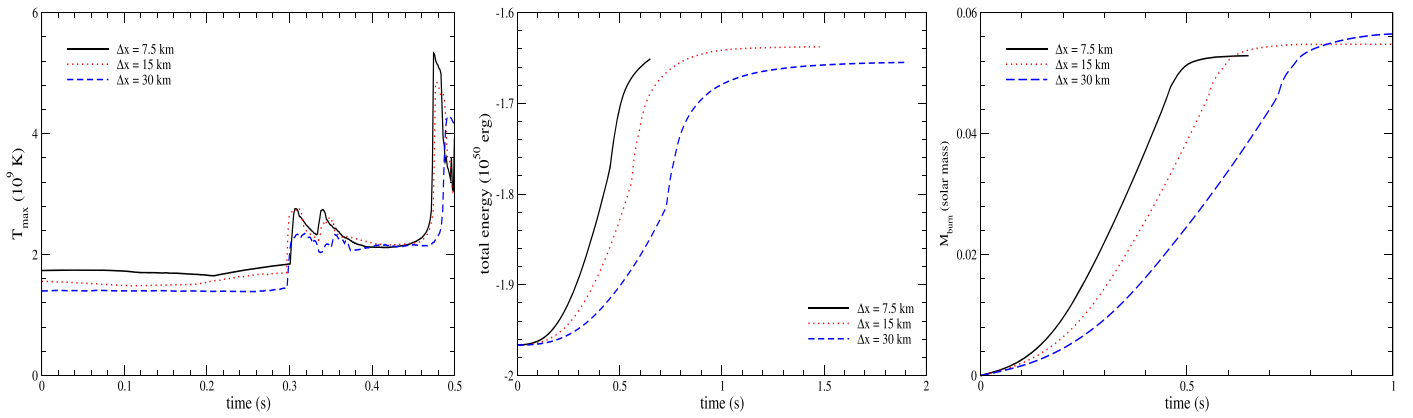


**Figure 38.** Left: time evolution of the central temperature for Models Test3-fine ( $\Delta x = 7.5$  km), Test3 ( $\Delta x = 15$  km) and Test3-coarse ( $\Delta x = 30$  km). Middle: similar to the left panel, but for the total energy. Right: similar to the left panel, but for the total burnt mass.

and diagonal line. Due to the much longer computational time for the high-resolution one, it is only computed until the reflected shock reaches the axis of rotation symmetry (i.e.,  $z$ -axis).

In the left panel of Figure 38 we plot the global maximum temperature against time for the three models. Due to the multiple dimensional effects in this test, the time where the system reaches its maximum temperature and the exact value are not monotonic. However, it shows a clear sign that the difference between the two models decreases when  $\Delta x$  drops. The peak temperature varies from  $4 \times 10^9$  K to  $5 \times 10^9$  K. The relative change drops from  $\sim 20\%$  to  $\sim 5\%$  between the two sets of models. However, we notice that the hot spot is inside the He envelope. So even if it exceeds the maximum threshold temperature of  $3 \times 10^9$  K, suitable for matter at density below  $10^7 \text{ g cm}^{-3}$ , it does not trigger any C detonation.

In the middle panel of Figure 38 we plot the total energy against time. This also tests the convergence of energy production rate in the He envelope due to the absence of second detonation. The maximum energy is limited to  $E = -1.6 \times 10^{50}$  erg. It can be seen that the He detonation has a stronger effect on the energy production rate. We observe a difference in the  $\sim 1\%$  of final energy by reducing half of the grid size but a difference of  $\sim 10\%$  time for the model to reach the same energy.

In the right panel of Figure 38 we plot the total burnt mass against time. The maximum burnt mass is limited to  $M_{\text{He}} = 0.05 M_{\odot}$ . The He detonation has larger but weakly converging differences in its propagation against different resolution. This conforms with the energy production rate in the middle panel. They all show to burn the same amount of matter, but the amount of time differs by 20% and is weakly converging.

The above test demonstrates that the trigger of C detonation by shock convergence is in general robust at the current resolution. However, the necessary  $\Delta x$  to determine the C-detonation trigger can be different, which depends on the chemical composition and also the numerical algorithm, such as how the nuclear reaction scheme is implemented. For further discussion in how resolution affects the discrimination of C-detonation trigger, we refer interested readers to some recent resolution studies for the colliding WD scenario in, e.g., Katz & Zingale (2019) and Kushnir & Katz (2019) and for the near-Chandrasekhar-mass deflagration-detonation transition scenario in, e.g., Fisher et al. (2019).

## Appendix F Comparison of Models in the Literature

We have studied the two-dimensional SN Ia model using the sub-Chandrasekhar-mass WD with the C detonation induced by surface He detonation. In this work, we compared effects of different detonation structures. Here, we consider the realizability of the detonation structure and compare with previous works in the literature.

### F.1. Shigeyama et al. (1992)

The spherical detonation is the same as the classical DD model (Shigeyama et al. 1992). The model is adopted for SN 1990N, which contains clear Si and Ca signatures with high velocities. Model 105-050-2-S50 is comparable to their Model CDT5 but with two qualitative differences. The two models share a similar CO core mass with the same metallicity at  $Z_{\odot}$ . Furthermore, the spherical He detonation setting in Model 105-050-2-S50 ensures that the evolution is spherical, which is compatible with their one-dimensional simulation with spherical symmetry. In their work, the detonation is triggered by hand, assuming that the He detonation on the surface has finished and sent an inward-going shock wave. Thus, there is no direct He burning considered. Second, that model assumes a direct CO detonation at the center, which comes from the assumed symmetry in the detonation wave. In our model, the He detonation is the “X”-type detonation. They find a yield of  $0.56 M_{\odot}$  and  $1.3 \times 10^{51}$  erg for the  $^{56}\text{Ni}$  production and total energy. Our model has a stronger detonation, as we find  $0.60 M_{\odot}$  and  $1.07 \times 10^{51}$  erg, respectively. The spherical detonation model is one of the higher viable shapes of detonation when the convection in the He layer is weak. In that case, the layer closest to the CO boundary has always the highest and uniform temperature. The whole layer will be the first site to trigger explosive He burning.

### F.2. Fink et al. (2007)

We compare our one-bubble model with the models in Fink et al. (2007) in the detonation structure. They consider an isothermal WD model of total mass  $0.9\text{--}1.0 M_{\odot}$ . They also explored different detonation patterns, including spherical, one-, two-, and five-bubble detonation structures. Their model `z4.24A_2dq_256` has a similar model configuration to our Model 105-050-2-2R50.

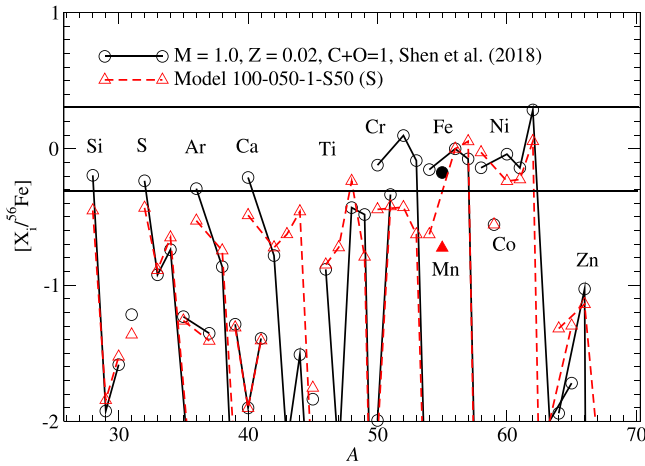


**Figure 39.**  $[X_i/^{56}\text{Fe}]$  for the model from Shen et al. (2018) ( $1 M_\odot$ , solar metallicity, and  $C + O = 1$ ) and our Model 100-005-1-S50.

They observe the second detonation to start at 1.08 s after the He detonation. Our model shows a very close result of 1.07 s. However, they find a yield of  $0.01 M_\odot$  unburned fuel,  $0.40 M_\odot$   $^{56}\text{Ni}$ , and  $0.51 M_\odot$   $^{28}\text{Si}$ . Our model shows more  $^{56}\text{Ni}$  production of mass  $0.49 M_\odot$  but a lower IME at  $0.18 M_\odot$ . There is more  $^{16}\text{O}$  fuel of mass  $0.11 M_\odot$ . The differences between the two models come from the burning scheme. An instantaneous input of energy is provided in the model of detonation wave, while our scheme applies the three-step burning scheme. The burning of  $^{16}\text{O}$  is suppressed when the ash temperature is not sufficiently high, especially around  $10^7 \text{ g cm}^{-3}$ , so that the estimated NQSE and NSE timescales become very long for all the burning to take place. For WD models where convection and turbulence are important, the fluid motion always disturbs the heat-generating He layer. As a result, local hot spot is possible to form. When temperature is close to the explosive burning of  $^4\text{He}$ , the formation of a hot spot is likely to be the first location of He detonation.

### F.3. Shen et al. (2018)

In Shen et al. (2018) the sub-Chandrasekhar-mass WD detonation model is also modeled in the framework of the dynamically driven DD double-detonation model. In this framework, when the two WDs pass by each other, the tidal force of the secondary WD triggers the C detonation of the primary WD, while the secondary WD later leaves the system without disrupting itself. The major difference of this physical picture from the other one is that the companion WD remains intact after the SN Ia, unlike the standard WD violent merger. This provides a smaller total mass in the system, where the ejecta may explode more easily with a higher velocity. In that work, SN Ia models with a mass range of  $0.8\text{--}1.1 M_\odot$  with a metallicity from 0 to  $2 Z_\odot$  and C/O mass fraction ratio from 0.3 to 1 are computed in the one-dimensional limit. Here we compare one of the most similar models, Model 100-005-1-S50, with their  $1 M_\odot$ , solar-metallicity,  $C+O = 1$  model. We choose this model because the initial detonation and the C detonation are spherically symmetric, and also the final  $^{56}\text{Ni}$  mass is similar. We have  $0.6 M_\odot$ , while their model has  $0.53 M_\odot$ .

In Figure 39 we plot the scaled mass fraction of the stable isotopes of the two models. We can see that in general the two models agree well qualitatively. Both models share the similar

relative mass fractions of the same elements. Some minor elements, including P, Cl, Na, and Sc, are surprisingly close to each other, despite their relatively small amounts (subject to larger systematic uncertainty) and the very different treatments in the explosion scenario, initial configuration, explosion treatment, and, in particular, the hydrodynamics. Major elements, such as Si, S, Ar, Ca, Fe, Ni, and Zn, are still close to each other. However, their model shows a systematically higher mass fraction for the high- $Y_e$  end isotopes (i.e., close to 0.5), e.g.,  $^{28}\text{Si}$ ,  $^{32}\text{S}$ ,  $^{36}\text{Ar}$ ,  $^{40}\text{Ca}$ ,  $^{52}\text{Cr}$ , and  $^{54}\text{Fe}$ . This shows that they have more incomplete burning such that more IMEs and light Fe-peak elements are formed. However, there are also some differences in Ti and Fe. Their model obtains higher abundance ratios of  $^{49}\text{Ti}$  and  $^{50,52,53}\text{Cr}$  than our model, but a lower ratio of  $^{46-48}\text{Ti}$ . We note that this feature is prominent in asymmetric detonation but not in symmetric detonation. Also, their  $^{55}\text{Mn}$  production is a few times higher, despite the low-density matter in the star. A more detailed study of how He detonation and C detonation are affected by the numerical treatment will be an interesting future work.

### F.4. Polin et al. (2019)

In Polin et al. (2019) the one-dimensional sub-Chandrasekhar-mass models are also calculated for a wide range of WD masses from  $0.6$  to  $1.2 M_\odot$  and He envelope masses from  $0.01$  to  $0.08 M_\odot$  using the CASTRO code. Their work studies the observational influences from the He envelope mass. It is found that two subclasses of light curves emerge. For a lighter He envelope, the light curve resembles some features in SNe Ia, including the correlation between mass, brightness, and velocity in the spectra. For a more massive He envelope, the light curve contains early UV flux and appears to be red owing to iron-peak elements on the surface, and later it turns blue.

Their methodology and initial models are different from ours. In their work, the nuclear reaction is directly solved by introducing the 13-isotope network containing  $^4\text{He}$ ,  $^{12}\text{C}$ ,  $^{16}\text{O}$ ,  $^{20}\text{Ne}$ ,  $^{24}\text{Mg}$ ,  $^{28}\text{Si}$ ,  $^{32}\text{S}$ ,  $^{36}\text{Ar}$ ,  $^{40}\text{Ca}$ ,  $^{44}\text{Ti}$ ,  $^{48}\text{Cr}$ ,  $^{52}\text{Fe}$ , and  $^{56}\text{Fe}$ . The nuclear reaction zone is specifically refined using the AMR option in CASTRO. A mixed transition between the CO core and He envelope is introduced. Also, at the beginning a width of  $\sim 1 \text{ km}$  spherical He detonation is put in by hand. On the other hand, we use a simplified seven-isotope network patched with the three-step burning scheme. The nuclear reaction is not directly resolved but relied on the level set, which assumes that the front of the most rapid reaction is directly represented by lines, where slower nuclear reactions take place assuming a given timescale. No mixing between CO core and He envelope core is introduced in our initial model. Also, due to the two-dimensional nature, our models include initial He detonations from spherical to different aspherical structure, but the typical size is larger ( $\sim 30 \text{ km}$ ).

Since their work does not aim for nucleosynthesis, here we only compare with their global chemical yields, in particular, their models with  $0.05 M_\odot$  He in the envelope. Their models show a different growth rate in the  $M_{\text{Ni}}$  as a function of  $M$ . They obtain a  $^{56}\text{Ni}$  mass from  $\sim 0.2$ , to  $0.5$ , and then to  $0.8 M_\odot$   $^{56}\text{Ni}$  in the  $0.9$ ,  $1.0$ , and  $1.1 M_\odot$ . On the other hand, we have  $0.02$ ,  $0.6$ , and  $0.8 M_\odot$   $^{56}\text{Ni}$ , respectively, from our Models 090-050-2-S50 (S), 100-050-2-S50 (S), and 110-050-2-S50 (S). Large differences appear in low-mass models. One major reason could be the nuclear reaction at the low density for the CO detonation. In our model, we have used a three-step nuclear



burning reaction, with the timescale dependent on the local density. On the other hand, they solve the nuclear reaction directly using the 13-isotope network in the hydrodynamics. And they also use the adaptive mesh refinement for resolving the nuclear burning at small scales. Both procedures can capture in greater detail how the low-density matter achieves complete burning, which may enhance the IMEs and  $^{56}\text{Ni}$  production. On the other hand, for a more massive WD model, our results agree with theirs well.

### F.5. Jacobs et al. (2016)

An extension of the comparison includes the pre-SN models evolved from a multidimensional hydrodynamics model. However, the exact site of nuclear runaway in our work is a model parameter. In fact, the detailed position and its runaway time can be modeled by following the exact hydrodynamics evolution over a few convective turnover timescales. For example, in Jacobs et al. (2016) the three-dimensional sub-Chandrasekhar-mass WDs of masses from 0.85 to 1.23  $M_{\odot}$  are studied using the low Mach number code MAESTRO. The evolution path prior to its nuclear runaway is studied.

Three nuclear runaway types are observed: localized runaway, quasi-equilibrium, and convective runaway. Localized runaway corresponds to the runaway taking place by a unique hot spot. This occurs when the convection fails to transport heat away generated from the nuclear reaction near the interface efficiently. Quasi-equilibrium stands for the opposite of the localized runaway. The convection can remove the heat efficiently so that no particular hot spot can grow. However, it is unclear finally whether the runaway is localized or collective. Convective runaway means the collective runaway in the form of helium nova.

In their study, there is not a clear trend in how they observed that localized runaway takes place in models with a mass of 0.8, 1.1, and 1.2  $M_{\odot}$ . Models with a mass of 1.0  $M_{\odot}$  tend to have quasi-equilibrium. Convective runaway takes place in the low-mass model with a low  $M_{\text{He}}$ . From this it shows that for a massive-star model the single spot runaway, e.g., 120-050-2-50 (X), is a more realistic model than collective runaway. Models with a mass  $M = 1.1 M_{\odot}$  tend to occur in a single spot runaway, and hence benchmark models such as 110-100-2-50 (X) are the most likely initial configuration. There is no clear conclusion for our benchmark models owing to the quasi-equilibrium outcome for  $M = 1.0 M_{\odot}$ . There are no models of mass 0.9  $M_{\odot}$  presented in their work to compare with ours.

### ORCID iDs

Shing-Chi Leung  <https://orcid.org/0000-0002-4972-3803>

Ken'ichi Nomoto  <https://orcid.org/0000-0001-9553-0685>

### References

- Abe, R. 1959, *PThPh*, **22**, 213
- Arnett, D. 1996, *Supernovae and Nucleosynthesis: An Investigation of the History of Matter from the Big Bang to the Present* (Princeton, NJ: Princeton University Press)
- Ashall, C., Mazzali, P., Bersier, D., et al. 2014, *MNRAS*, **445**, 4427
- Benvenuto, O. G., Panei, J. A., Nomoto, K., Kitamura, H., & Hachisu, I. 2015, *ApJL*, **809**, L6
- Bergström, L., & Goobar, A. 2004, *Cosmology and Particle Astrophysics* (Berlin: Springer)
- Branch, D., & Wheeler, J. C. 2017, *Supernova Explosions* (Berlin: Springer)
- Brown, P. J., Smitka, M. T., Wang, L., et al. 2015, *ApJ*, **805**, 74
- Calder, A. C., Townsley, D. M., Seitenzahl, I. R., et al. 2007, *ApJ*, **656**, 313
- Cenko, S. B., Filippenko, A. V., & Silverman, J. M. 2012, *CBET*, **3111**, 2
- Churazov, E., Sunyaev, R., Isern, J., et al. 2015, *ApJ*, **812**, 62
- Dan, M., Guillochon, J., Brügger, M., Ramirez-Ruiz, E., & Rosswog, S. 2015, *MNRAS*, **454**, 4411
- Dan, M., Rosswog, S., Guillochon, J., & Ramirez-Ruiz, E. 2011, *ApJ*, **737**, 89
- Dave, P., Kashyap, R., Fisher, R., et al. 2017, *ApJ*, **841**, 58
- Diehl, R., Siebert, T., Hillebrandt, W., et al. 2015a, *A&A*, **574**, A72
- Diehl, R., Siebert, T., Hillebrandt, W., et al. 2015b, *Sci*, **345**, 1162
- Dimitriadis, G., Sullivan, M., Kerzendorf, W., et al. 2017, *MNRAS*, **468**, 3798
- Feltzing, A., Fohlman, M., & Bensby, T. 2007, *A&A*, **467**, 665
- Fink, M., Hillebrandt, W., & Röpke, F. K. 2007, *A&A*, **476**, 1133
- Fink, M., Röpke, F. K., Hillebrandt, W., et al. 2010, *A&A*, **514**, A53
- Fisher, R., Mozumdar, P., & Casabona, G. 2019, *ApJ*, **876**, 64
- Foley, R. J., Fox, O. D., McCully, C., et al. 2014, *MNRAS*, **443**, 2887
- Fryer, C. L., Ruiter, A. J., Belczynski, K., et al. 2010, *ApJ*, **725**, 296
- Goobar, A., Johansson, J., Amanullah, R., et al. 2014, *ApJ*, **784**, 12
- Graur, O., Zurek, D., Shara, M. M., et al. 2016, *ApJ*, **819**, 31
- Guerrero, J., García-Berro, E., & Isern, J. 2004, *A&A*, **413**, 257
- Hillebrandt, W., & Niemeyer, J. C. 2000, *ARA&A*, **38**, 191
- Isern, J., Jean, P., Bravo, E., et al. 2016, *A&A*, **588**, 67
- Iwamoto, K., Brachwitz, F., Nomoto, K., et al. 1999, *ApJS*, **125**, 439
- Jacobs, A. M., Zingale, M., Nonaka, A., Almgren, A. S., & Bell, J. B. 2016, *ApJ*, **827**, 84
- Jha, S. W. 2017, in *Handbook of Supernovae*, ed. A. W. Alsabti & P. Murdin (Cham: Springer), 375
- Jiang, J.-A., Doi, M., Maeda, K., et al. 2017, *Natur*, **550**, 80
- Kandrasehoff, M., Cenko, S. B., & Li, W. 2012, *CBET*, **3111**, 1
- Kasen, D. 2010, *ApJ*, **708**, 1025
- Katz, M. P., & Zingale, M. 2019, *ApJ*, **874**, 169
- Kitamura, H. 2000, *ApJ*, **539**, 888
- Kushnir, D., & Katz, B. 2019, arXiv:1904.10001
- Leung, S.-C., Chu, M.-C., & Lin, L.-M. 2015a, *ApJ*, **812**, 110
- Leung, S.-C., Chu, M.-C., & Lin, L.-M. 2015b, *MNRAS*, **454**, 1238
- Leung, S.-C., & Nomoto, K. 2017, in *JPS Conf. Proc.*, 14th Int. Symp. on Nuclei in the Cosmos (NIC2016), ed. S. Kubono et al., 020506
- Leung, S.-C., & Nomoto, K. 2018, *ApJ*, **861**, 143
- Li, W., Filippenko, A. V., & Treffers, R. R. 2001, *ApJ*, **546**, 734
- Livne, E. 1990, *ApJL*, **354**, L53
- Livne, E., & Arnett, D. 1995, *ApJ*, **452**, 62
- Livne, E., & Glasner, A. S. 1990, *ApJ*, **361**, 244
- Livne, E., & Glasner, A. S. 1991, *ApJ*, **370**, 272
- Maoz, D., Mannucci, F., Li, W., et al. 2011, *MNRAS*, **412**, 1508
- Maoz, D., Mannucci, F., & Nelemans, G. 2014, *ARA&A*, **52**, 107
- Marion, G. H., Kirschner, R. P., Foley, R. J., Challis, P., & Irwin, J. 2012, *CBET*, **3111**, 3
- Moll, R., Raskin, C., Kasen, D., & Woosley, S. E. 2014, *ApJ*, **785**, 105
- Moll, R., & Woosley, S. E. 2013, *ApJ*, **774**, 137
- Moore, K., Townsley, D. M., & Bildsten, L. 2013, *ApJ*, **776**, 97
- Nabi, J.-U., & Klapdor-Kleingrothaus, H. V. 1999, *ADNDT*, **71**, 149
- Nabi, J.-U., & Klapdor-Kleingrothaus, H. V. 2004, *ADNDT*, **88**, 237
- Niemeyer, J. C., & Hillebrandt, W. 1995, *ApJ*, **452**, 779
- Nomoto, K. 1982a, *ApJ*, **253**, 798
- Nomoto, K. 1982b, *ApJ*, **257**, 780
- Nomoto, K. 1984, *ApJ*, **277**, 791
- Nomoto, K., Iwamoto, K., & Kishimoto, N. 1997, *Sci*, **276**, 1378
- Nomoto, K., & Leung, S.-C. 2017, in *Handbook of Supernovae*, ed. A. W. Alsabti & P. Murdin (Cham: Springer), 1275
- Nomoto, K., & Leung, S.-C. 2018, *SSRv*, **214**, 67
- Nomoto, K., Sugimoto, D., & Neo, S. 1976, *Ap&SS*, **39**, L37
- Nomoto, K., Thielemann, F.-K., & Yokoi, K. 1984, *ApJ*, **286**, 644
- Nugent, H., Sullivan, M., Cenko, S. B., et al. 2011, *Natur*, **480**, 344
- Osher, S., & Sethian, J. A. 1988, *JCP*, **79**, 12
- Pakmor, R. 2017, in *Handbook of Supernovae*, ed. A. W. Alsabti & P. Murdin (Cham: Springer), 1257
- Pakmor, R., Kromer, M., Taubenberger, S., & Springel, V. 2013, *ApJL*, **770**, L8
- Polin, A., Nugent, P., & Kasen, D. 2019, *ApJ*, **873**, 84
- Rasio, F. A., & Shapiro, S. L. 1995, *ApJ*, **438**, 887
- Raskin, C., Kasen, D., Moll, R., Schwab, J., & Woosley, S. 2014, *ApJ*, **788**, 75
- Raskin, C., Scannapieco, E., Fryer, C., Rockefeller, G., & Timmes, F. X. 2012, *ApJ*, **746**, 62
- Rauscher, T., & Thielemann, F. K. 2000, *ADNDT*, **75**, 1
- Reddy, B. E., Tomkin, J., Lambert, D. L., & Prieto, C. A. 2003, *MNRAS*, **340**, 304
- Reinecke, M., Hillebrandt, W., Niemeyer, J. C., & Klein, R. 1999, *A&A*, **347**, 731

- Roepke, F. K., & Hillebrandt, W. 2005, [A&A](#), **431**, 635
- Sato, Y., Nakasato, N., Tanikawa, A., et al. 2015, [ApJ](#), **807**, 105
- Segretain, L., Chabrier, G., & Mochkovitch, R. 1997, [ApJ](#), **481**, 355
- Seitenzahl, I. R., Roepke, F. K., Fink, M., & Pakmor, R. 2010, [MNRAS](#), **407**, 2297
- Shappee, B. J., & Stanek, K. Z. 2011, [ApJ](#), **733**, 124
- Shappee, B. J., Stanek, K. Z., Kochanek, C. S., & Garnavich, P. M. 2017, [ApJ](#), **841**, 48
- Sharpe, G. J. 1999, [MNRAS](#), **310**, 1039
- Shen, K. J., Kasen, D., Miles, B. J., & Townsley, D. M. 2018, [ApJ](#), **854**, 52
- Shigeyama, T., Nomoto, K., Yamaoka, H., & Thielemann, F.-K. 1992, [ApJL](#), **386**, L13
- Sim, S. A., Fink, M., Kromer, M., et al. 2012, [MNRAS](#), **420**, 3003
- Sim, S. A., Roepke, F. K., Hillebrandt, W., et al. 2010, [ApJL](#), **714**, L52
- Sobeck, J. S., Ivans, I. I., Simmerer, J. A., et al. 2006, [AJ](#), **131**, 2949
- Taubenberger, S. 2017, in *Handbook of Supernovae*, ed. A. W. Alsabti & P. Murdin (Cham: Springer), 317
- Telesco, C. M., Hoefflich, P., Li, D., et al. 2015, [ApJ](#), **798**, 93
- Timmes, F., Fryer, C., Timmes, F., et al. 2019, *BAAS*, **51**, 2
- Timmes, F. X. 1999, [ApJ](#), **124**, 241
- Timmes, F. X., & Arnett, D. 1999, [ApJ](#), **125**, 277
- Timmes, F. X., & Swesty, D. 1999, [ApJS](#), **126**, 501
- Townsley, D. M., Calder, A. C., Asida, S. M., et al. 2007, [ApJ](#), **668**, 1118
- Travaglio, C., Hillebrandt, W., Reinecke, M., & Thielemann, F.-K. 2004, [A&A](#), **425**, 1029
- Umeda, H., Nomoto, K., Yamaoka, H., & Wanajo, S. 1999, [ApJ](#), **513**, 861
- Woosley, S. E., & Kasen, D. 2011, [ApJ](#), **734**, 38
- Woosley, S. E., Taam, R. E., & Weaver, T. A. 1986, [ApJ](#), **301**, 601
- Yamaguchi, H., Eriksen, K. A., Badenes, C., et al. 2014, [ApJL](#), **780**, L136
- Yamaguchi, H., et al. 2015, [ApJL](#), **801**, L31
- Yang, Y., Wang, L., Baade, D., et al. 2018, [ApJ](#), **852**, 89
- Yoon, S.-C., Podsiadlowski, P., & Rosswog, S. 2007, [MNRAS](#), **380**, 933
- Yungelson, L. R. 2005, in *White Dwarfs: Cosmological and Galactic Probes*, ed. E. M. Sion, S. Vennes, & H. L. Shipman (Dordrecht: Springer), 163